MOLECULAR SIMULATION STUDY OF ENHANCED OIL RECOVERY METHODS IN
TIGHT FORMATION

by

Chuncheng Li
Bachelor of Science, Northeast Petroleum University, China, 2014
Master of Science, Northeast Petroleum University, China, 2017

A Dissertation

Submitted to the Graduate Faculty

of the

University of North Dakota

In partial fulfillment of the requirements

for the degree of

Doctor of Philosophy

Grand Forks, North Dakota

December
2020

ii

Name: Chuncheng Li

Degree: Doctor of Philosophy

       This document, submitted in partial fulfillment of the requirements for the degree from the University of North Dakota, has been read by the Faculty Advisory Committee under whom the work has been done and is hereby approved.

Hui Pu

Vamegh Rasouli

Kegang Ling

Jerome Delhommelle

       This document is being submitted by the appointed advisory committee as having met all the requirements of the School of Graduate Studies at the University of North Dakota and is hereby approved.

Chris Nelson
Dean of the School of Graduate Studies

12/3/2020

Date

<div align="center">PERMISSION</div>

Title   Molecular Simulation Study of Enhanced Oil Recovery Methods in Tight Formation

Department   Petroleum Engineering

Degree   Doctor of Philosophy

In presenting this dissertation in partial fulfillment of the requirements for a graduate degree from the University of North Dakota, I agree that the library of this University shall make it freely available for inspection. I further agree that permission for extensive copying for scholarly purposes may be granted by the professor who supervised my dissertation work or, in his absence, by the Chairperson of the department or the dean of the Graduate School. It is understood that any copying or publication or other use of this dissertation or part thereof for financial gain shall not be allowed without my written permission. It is also understood that due recognition shall be given to me and to the University of North Dakota in any scholarly use which may be made of any material in my dissertation.

<div align="right">Chuncheng Li
11/30/2020</div>

TABLE OF CONTENTS

LISTS OF FIGURES

LISTS OF TABLES

ACKNOWLEDGMENTS

ABSTRACT

The Middle Bakken Formation of the Williston Basin is a typical tight formation with the predicted primary oil recovery of less than 10%, which results in large amounts of oil remaining in the reservoir. Therefore, an effective enhanced oil recovery (EOR) method for recovering the residual oil is crucially important. To obtain the microscopic EOR mechanisms, molecular simulation methods including Monte Carlo (MC) simulations and molecular dynamics (MD) simulations were applied to study the various EOR methods, such as CO_2 injection, hydrocarbon gas injection, and nanofluid flooding. A series of molecular models, including bulk systems, interfacial systems, and nanoconfined systems, were built to evaluate the potentials of the injected fluids to improve oil recovery.

CO_2 injection is a successful EOR technology that is being widely applied in North American oil fields. Studies have suggested CO_2-based EOR is technically possible in the Middle Bakken Formation. The swelling of the crude oil/CO_2 system plays a crucial role in the CO_2 flooding process. Therefore, a better understanding of the effect of CO_2 on crude oil swelling and viscosity reduction is critical for a successful CO_2 EOR project. In this dissertation, a series of n-alkane/CO_2 systems were studied by performing configurational-bias Monte Carlo (CBMC) simulations and MD simulations. The effects of alkyl chain length, pressure, and temperature on the CO_2 solubility and the swelling factor were investigated. The solubility of CO_2 and the swelling factor of CO_2 saturated n-alkane are positively correlated to the pressure, while negatively correlated to the alkyl chain length and temperature. With more CO_2 dissolved, the interaction energy between n-alkane molecules becomes less negative, which indicates the swelling of the n-alkane/CO_2 system. N-alkanes with longer alkyl chain have more negative intermolecular interaction energy, and thus have a smaller swelling factor after saturating with CO_2. With the increase of the CO_2 mole

fraction, the viscosity of the n-alkane/CO_2 system is reduced. N-alkanes with longer alkyl chains have a larger viscosity reduction with increasing amounts of dissolved CO_2.

Besides CO_2, hydrocarbon gases, like methane and ethane, can also mobilize the residual oil and enhance oil recovery. The gas solubility, volume swelling factor, oil diffusion coefficient, minimum miscibility pressure (MMP), and the oil extraction from nanoslits were then studied to compare the efficiency of different gases in the EOR process. Based on the Bakken oil composition, a molecular model of the crude oil containing different types of alkanes was built. MD simulations were carried out to study the interfacial interactions between the Bakken crude oil and the injected gases and the oil extraction from the calcite nanoslits. At various pressures and reservoir temperature, density profiles were plotted to show the distributions of different components, and the solubility of gases in crude oil was calculated. The simulation results show that all three gases hold great potential in further improving oil recovery. At constant temperature and pressure, ethane holds the highest solubility in crude oil and can induce the most pronounced oil swelling. Meanwhile, ethane can achieve the lowest MMP and the most significant oil diffusion coefficient. Without the effect of nano-confinement, ethane is most effective in mobilizing crude oil. However, CO_2 is more effective in extracting oil from the nanoslits.

Recent studies have also reported various types of nanoparticles (NPs) for improving oil recovery either alone or in combination with surfactants. The mechanisms of surface-modified silica (SiO_2) NPs in improving oil recovery were investigated. Interfacial tensions (IFTs) of octane (C_8H_{18})/water systems in the presence of different NPs were calculated. Quartz nanochannels were constructed to study the effect of NPs on oil flow through nanopores in rocks. Both water-wet and oil-wet surfaces were considered. Simulation results indicate that IFT reduction depends strongly on the distribution and the interfacial concentration of NPs. Surface-modified NPs with both

xvii

hydrophilic and hydrophobic functional groups can reduce the IFT between oil and water. However, the IFT reduction is not significant in terms of EOR application. The alkanes/water/NPs transportation in confined nanochannels shows that the initial rock wettability affects the water flooding performance and the final oil recovery. The surface-modified NPs hold a higher capacity in detaching oil droplets from the oil-wet mineral surface regardless of their abilities to change interfacial tension. Surface modification is crucial to improve the surface properties of SiO_2 NPs. The strong interactions between NPs and oil/rock lead to oil detachment and incremental oil recovery. The chemical composition of the functional groups and the surface coverage of the hydrophilic/hydrophobic functional groups should be carefully tuned to achieve the highest oil recovery rate.

Molecular simulation study provides better insight into the interactions between oil components and injected fluids or mineral surfaces at the molecular level. The effect of injected fluids on the properties of the oil can be clearly explained. The application of molecular simulation methods could play an important role in interpreting experimental results and providing guidance for practical oil recovery processes in the Bakken Formation.

CHAPTER 1

INTRODUCTION

1.1 Background

The Middle Bakken Formation of the Williston Basin is one of the major unconventional tight oil reservoirs in the United States. The ultra-low matrix permeability prevents oil from flowing naturally into the wellbore. The successful application of horizontal drilling and multistage hydraulic fracturing has made it possible to produce crude oil from the reservoir (Iwere et al., 2012; Phillips et al., 2007; Yang and Zoback, 2014). However, the predicted recovery factor of primary oil recovery is less than 10% due to the tight nature of the formation (Clark, 2009; LeFever and Helms, 2006). Therefore, a large amount of crude oil remains in the reservoir. For the oil industries, it's crucial to develop an effective enhanced oil recovery (EOR) technique to recover the maximum amount of the residual oil.

Carbon dioxide (CO_2) EOR has been proven to be a successful technology in conventional reservoirs (Perera et al., 2016; Qin et al., 2015). CO_2 can mobilize the oil through swelling the oil, extracting hydrocarbons, and reducing oil viscosity (Abedini and Torabi, 2014; Orr et al., 1982). The injection of CO_2 into oil reservoirs results in incremental oil recovery as well as CO_2 capture and storage, which can significantly reduce greenhouse gas emissions to the atmosphere (Abedini and Torabi, 2014; Aycaguer et al., 2001; Gaspar Ravagnani et al., 2009). As a typical tight formation, the Bakken Formation holds a huge CO_2 storage capacity and the potential of significantly increasing oil production by injecting CO_2 (Sorensen et al., 2014). Both experimental studies and numerical simulations have shown that CO_2 injection could be an effective EOR method to improve the oil recovery in tight formations (Kurtoglu, 2014; Kurtoglu et al., 2013; Sorensen et al., 2015; Yu et al., 2015).

1

Although CO_2 EOR is a very successful and mature technology in the U.S., it has not been applied in many unconventional reservoirs like the Bakken Formation because of the limited low-cost CO_2 supply. In addition, wells in the Bakken Formation produce large amounts of natural gas, which is often flared off. This flaring not only wastes energy but also emits large amounts of greenhouse gas, carbon dioxide. Some experimental studies have focused on using hydrocarbon gas as a working fluid for EOR in the Bakken Formation (Steven B Hawthorne et al., 2019; Jin et al., 2016). Hydrocarbon gas injection can improve oil recovery as well as reduce CO_2 emissions from gas flaring. It has been successfully employed in the North Sea oil fields for several decades (Awan et al., 2008). Different gases should be compared for screening the best injected gas. In terms of the tight formation, the EOR potential of the gases in the nanopores should be particularly analyzed.

Besides gas injection, the chemical injection has been adjudged as an efficient EOR method to recover the residual oil trapped in the reservoir. Among the chemical EOR techniques, surfactant flooding is most widely investigated and employed in the oil industries. Surfactants can mobilize residual oil by lowering the oil/water interfacial tension and/or by altering the rock wettability from oil-wet to water-wet (Kamal et al., 2017b). Under mild reservoir conditions (low temperature, low salinity), most surfactants perform well in improving oil recovery. However, under harsh reservoir conditions (high temperature, high salinity), the stability and effectiveness of surfactants can be a challenging task (Kamal et al., 2017b; Negin et al., 2017). Moreover, the high cost of chemicals and the surfactant loss due to the high adsorption on rock surfaces also limit the application of surfactant flooding (Gogoi, 2011). Recently, nanotechnology has been employed to solve various challenges arising in surfactant flooding. By adding different nanoparticles (NPs) in the base fluids (such as water, brine, ethanol, etc.), investigators have developed various types of

2

nanofluids to improve oil recovery (Kamal et al., 2017a; Nazari Moghaddam et al., 2015). Studies have shown that NPs can improve oil recovery either alone or in combination with surfactants (Hendraningrat et al., 2013; Zargartalebi et al., 2015). Although substantial studies have focused on using NPs to improve oil recovery, whether the NPs adsorbed at an interface can reduce the interfacial tension is still controversial. The main EOR mechanism of different NPs has not been clearly demonstrated.

Moreover, tight rocks are usually dominated by nanoscale and microscale pore throats (Nelson, 2009; Zhang et al., 2020), and fluids are significantly affected by the strong surface-fluid interactions (Alharthy et al., 2013). The rock wettability and the nano-confinement should be considered in the investigation of EOR methods in tight formation. Understanding the behavior of fluids at the nanoscale is important to the development of injected fluids for EOR applications. However, nanoscale phenomena are usually difficult to observe from laboratory experiments. In recent years, molecular simulations have been employed in the oil industries to study different EOR methods (Le et al., 2015; Li et al., 2019b; Tang et al., 2019; Yan et al., 2017). Molecular simulations can provide a molecular-level insight into the interactions between components, which is generally difficult to obtain from experimental studies.

1.2 Research Objective

A molecular simulation study on the evaluation of injected fluids for EOR in tight formation was conducted. The fluid properties under high temperature and high pressure conditions were calculated. The oil extraction processes in nanochannels were presented. For the gas injection EOR methods, the feasible working conditions of different gases were evaluated. For the nanofluid systems, the mechanisms of different types of NPs in improving oil recovery were demonstrated.

1.3 Dissertation Organization

This dissertation has seven chapters including two main topics, gas injection EOR and nanofluids for EOR.

Chapter 1 is the introduction, which explains the research background, objective, and organization of the dissertation.

Chapter 2 provides a literature review and laboratory tests of the rock and reservoir fluid properties in the Middle Bakken Formation.

Chapter 3 describes the molecular simulation methods and the application in the area of petroleum engineering.

Chapter 4 presents the molecular simulation study on the n-alkane/CO_2 systems. The effects of alkyl chain length, pressure, and temperature on the CO_2 solubility and the alkane swelling factor were investigated.

Chapter 5 presents the interfacial interactions between Bakken crude oil and injected gases at reservoir temperature. The gas solubility, volume swelling factor, oil diffusion coefficient, and minimum miscibility pressure (MMP) were studied to compare the efficiency of different gases in the EOR process.

Chapter 6 presents the effect of different gases on the oil detachment from mineral surfaces as well as the effect of nano-confinement on the oil extraction.

Chapter 7 presents the effect of different NPs on the interfacial tensions (IFTs) of octane (C_8H_{18})/water systems and oil transport through nanochannels.

Chapter 8 provides the conclusions and recommendations of the dissertation.

4

CHAPTER 2

RESERVOIR DESCRIPTION OF THE MIDDLE BAKKEN FORMATION

The Bakken Formation of the Williston Basin is located in western North Dakota, eastern Montana, and southern Saskatchewan. As shown in Figure 2-1, the formation consists of three members ranging in age from late Devonian to early Mississippian. The Middle Bakken is the principal oil reservoir which is bounded by the Upper Bakken Shale and the Lower Bakken Shale. This chapter mainly describes the rock and fluid properties of the Middle Bakken Formation.
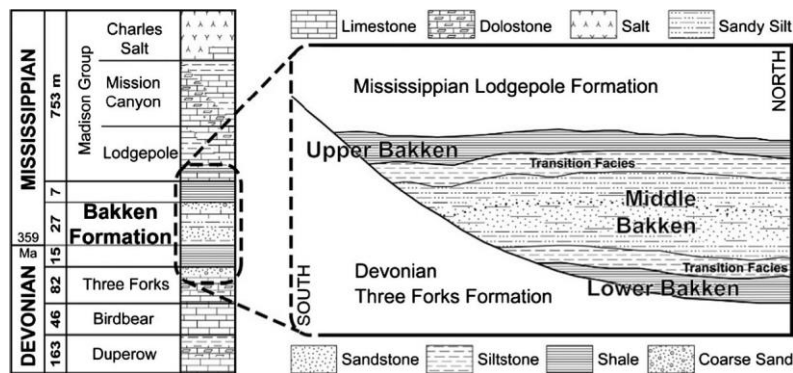
Figure 2-1 A cross section of the Bakken Formation (West et al., 2013)

The Middle Bakken core plugs from three wells were provided by the North Dakota Geological Survey Wilson M. Laird Core Sample Library. Figure 2-2 shows the location and North Dakota Industrial Commission (NDIC) well numbers from which the rock core samples were obtained. Different samples were prepared based on the type of tests. Results from literature and laboratory tests are presented.
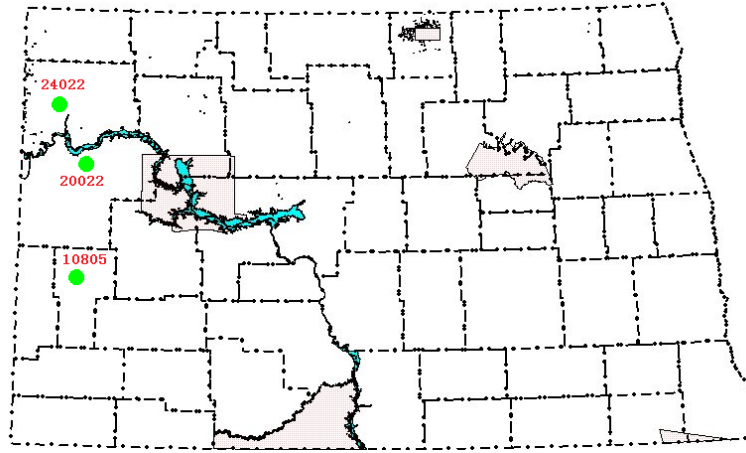
Figure 2-2 Location (designated by green circles) and NDIC well numbers from which the rock

core samples were obtained.

2.1 Rock Properties of the Middle Bakken Formation

2.1.1 Porosity and permeability

The relationship of air permeability (K) and porosity (Φ) for the Middle Bakken rock is shown

in Figure 2-3 The porosity of the Middle Bakken rock samples ranges from 1.5-10.8%, and the

matrix permeability ranges from < 0.0001 to 0.805 mD. There is no simple relationship between

permeability and porosity for the Middle Bakken Formation samples. For a given porosity, the

permeability varies over a range of 2–4 orders of magnitude, because the permeability–porosity

relationship is highly affected by the clay content and the natural fractures.
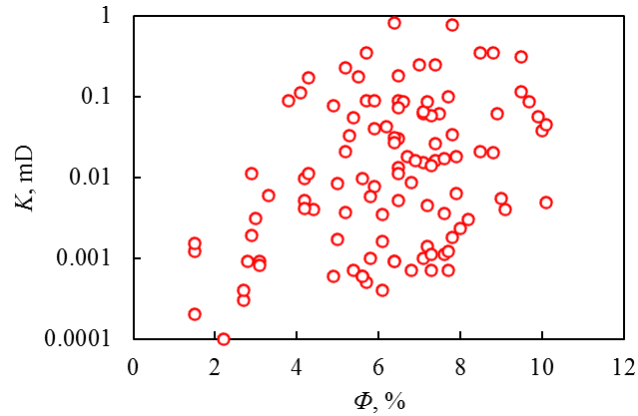
Figure 2-3 Permeability-porosity relationship of rock samples from the Middle Bakken.

2.1.2 Mineral composition

The mineral composition of the Middle Bakken rocks was analyzed by X-ray diffraction (XRD). XRD records the diffraction or reflection of a beam of X-rays by rock samples. The unique arrangement of atoms in each mineral's crystal structure interacts with the X-ray beam, producing regions of diffraction intensity, or peaks, diagnostic for that mineral. XRD data can be processed for identifying mineral types and determining the mineral fractions (K. Liu et al., 2017). Powder samples were prepared using the micronizing mill. The XRD analysis was performed by the X-ray diffractometer. As shown in Figure 2-4, quartz, calcite, and dolomite are the dominant minerals of the Middle Bakken samples, and illite is the major clay type.
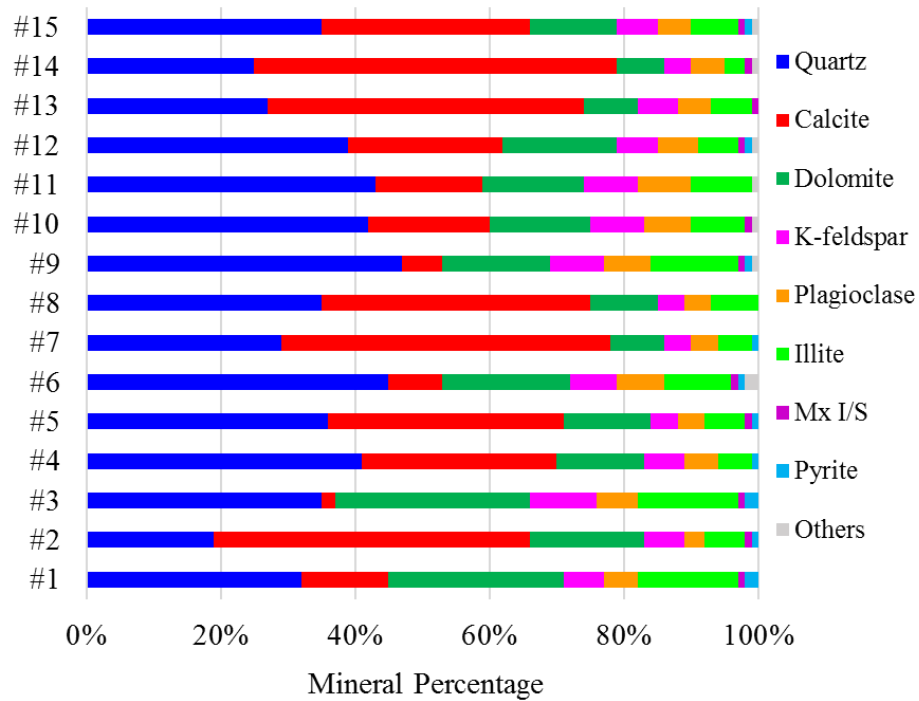
Figure 2-4 XRD results for the Middle Bakken core samples

2.1.3 Pore structure

The morphology of the rock samples was observed using scanning electron microscopy (SEM). The SEM images were visually examined and different pore types were identified (Figure 2-5). Pore structures in Middle Bakken samples are mainly comprised of pores associated with organic matter (OM), pores between grains and crystals (interparticle), and pores within grains, crystals, and clay aggregates (intraparticle) (Loucks et al., 2012; Saraji and Piri, 2015). Very few organic matters are found in the Middle Bakken core samples.

8
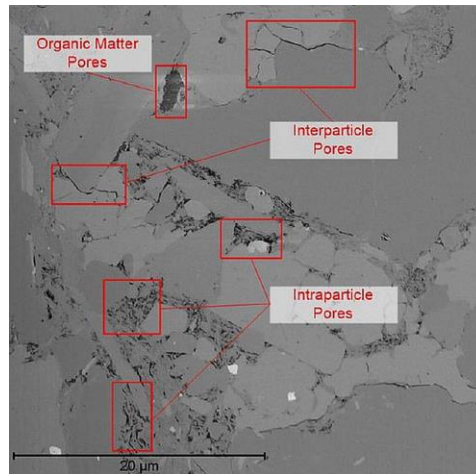
Figure 2-5 Middle Bakken pore types observed from SEM images (Saraji and Piri, 2015)

Most pores of the matrix are slit-like nanopores or nanochannels. As shown in Figure 2-6, the outmost nanochannel is connected with other pores through several pore throats, and the shapes of the throats vary greatly. The sizes of the pore throats are all in nanoscale. The sophisticated pore network has a significant impact on the fluids flowing through the rock matrix.
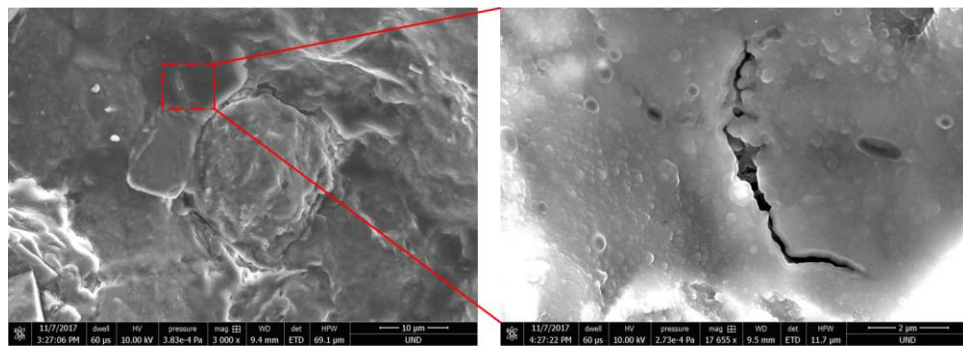
Figure 2-6 Slit-like nanopores or nanochannels in a Middle Bakken rock sample

2.1.4 Pore size distribution

The core samples were crushed to <250 μm and oven dried for 8 h at 383 K (110 ℃) to be used for nitrogen (N_2) gas adsorption. The N_2 adsorption and desorption isotherms were collected at 77 K (−196 ℃) using the automated gas sorption analyzer. Figure 2-7 shows the N_2

adsorption/desorption isotherms of the samples. The shape of the hysteresis loop indicates the pores of the Middle Bakken rock are slit-shaped pores (Labani et al., 2013).
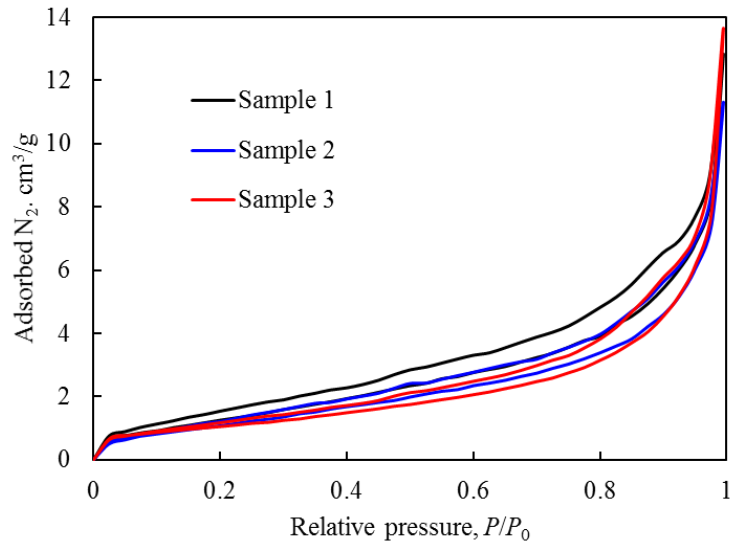
Figure 2-7 N_2 adsorption/desorption isotherms of the Middle Bakken rock samples.

The pore size distributions of the rock samples are shown in Figure 2-8. According to the International Union of Pure and Applied Chemistry (IUPAC) classification (Rouquerol et al., 1994), the Middle Bakken has micropores (< 2 nm), mesopores (2–50 nm), and macropores (> 50 nm), while the pore volume is dominated by mesopores.
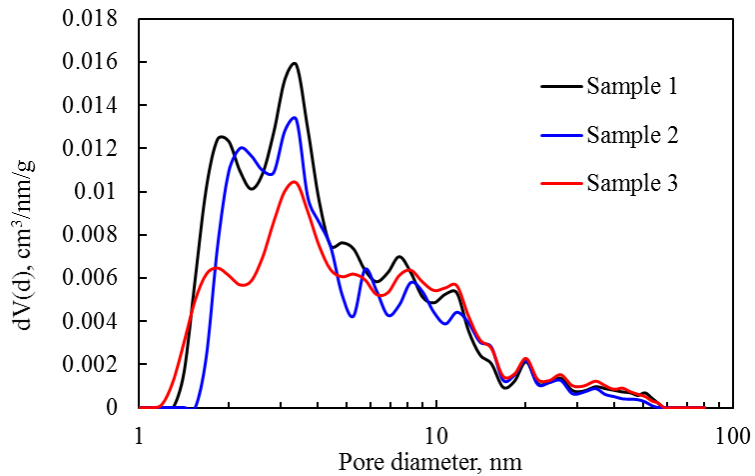
Figure 2-8 Pore size distributions of Middle Bakken Formation.

2.2 Crude Oil Properties of the Middle Bakken Formation

Bakken crude oil is a light crude oil with an API gravity generally between 38 ° and 43 °. Low molecular weight hydrocarbons are the dominant components for all oil samples. Very few asphaltenes and resins were found in the oil samples (Hawthorne et al., 2016; Kurtoglu, 2014). A typical Bakken crude oil composition is shown in Table 2-1.

Table 2-1 Bakken oil components (Hawthorne et al., 2016).

Oil component	"Live" oil	"Dead" oil
	Mole fraction	Mole fraction
CO_2	0.0032	0
N_2	0.0322	0
CH_4	0.2687	0
C_2H_6	0.1080	0
C_3-C_4	0.1309	0.0001
C_5-C_7	0.1369	0.0884
C_8-C_{13}	0.1840	0.4770
C_{14}-C_{24}	0.0947	0.3016
C_{25}-C_{36+}	0.0415	0.1329

The light crude oil with very low viscosity can flow better for production and transport. However, within the nanopores or nanochannels, the fluid flow is affected by the strong rock-oil

interactions. The flow investigation at the nanoscale is more complex compared to the flow without nanoconfinement.

2.3 Triple-Porosity System in the Middle Bakken Formation

The Middle Bakken Formation can be seen as a triple-porosity system made up of the matrix, less permeable micro-fractures, and more permeable macro-fractures after hydraulic fracturing (Figure 2-9). The oil flow process is divided into 3 parts: a). from the matrix to micro-fractures, b). from micro-fracture to macro-fractures, c). from macro-fractures to horizontal well (Alahmadi, 2010).
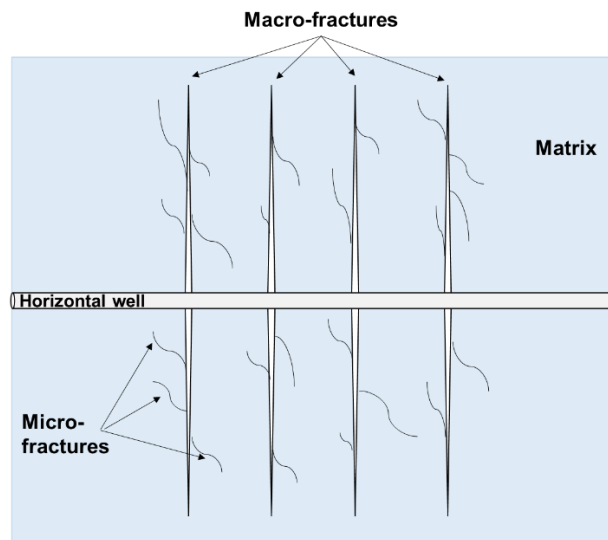
Figure 2-9 triple-porosity system of fractured reservoirs

After analyzing the oil production of the Bakken production well, the production history is divided into 3 main stages:

Stage 1 represents the transient linear flow in the macro-fractures. The initial production rate is relatively high but decreases rapidly. The permeability of macro-fractures is usually high and hence this flow stage will be very short.

The decline of oil production in Stage 2 was relatively slow, cause the flow in the macro-fractures, micro-fractures, and matrix can almost make up the pressure reduction in the macro-fractures.

Stage 3 is the main and longest flow region. The pressure of the matrix declined gradually. This flow stage is governed by exponential decline.

Understanding the fluid properties at nanoscale and improving the efficiency of oil flow into the fractures is extremely important for EOR in the Middle Bakken Formation.

CHAPTER 3

SIMULATION METHODOLOGY

Although hydraulic fractures are commonly created to enhance the permeability of tight

formations, the flow of hydrocarbons to the fractures occurs through the intrinsic matrix nanopores

(Josh et al., 2012). Therefore, it is important to study the fluid properties under nano-confinement.

However, nanoscale phenomena can hardly be observed from experimental studies. Nowadays,

molecular simulation has become a powerful tool to reveal details of molecular processes on

lengths of space and time unreachable to experimental observations. In this chapter, an

introduction of molecular simulation and its applications in petroleum engineering is presented.

3.1 Molecular Simulation

Molecular simulation is a method for simulating molecular structures and behavior to

understand various physical and chemical properties of molecular systems. Based on statistical

mechanics, quantum mechanics, or experiments, a set of reasonable models and algorithms have

been constructed. The macroscopical phenomena can be understood at a microscopical level by

performing molecular simulations.

There are two main simulation methods in molecular modeling: Monte Carlo (MC)

(Metropolis et al., 1953) and molecular dynamics (MD) (Alder and Wainwright, 1957, 1959). In

an MC simulation, each new configuration of the system is generated by a random move of an

atom or molecule. MC simulation is used to evaluate the configurational properties as ensemble

averages for a system in equilibrium. While in an MD simulation, the atoms in the system move

by a driving force based on a force field. MD simulation calculates the properties as time averages.

The obvious advantage of MD over MC is that MD gives out dynamical properties as well as

atoms' trajectories throughout the simulations. In this dissertation, we mainly adopted the MD simulation method,

3.2 Molecular Dynamics Simulation

MD simulation is a computer simulation method for analyzing the physical movements of atoms and molecules. In an MD simulation, atoms are modeled as point charges with an associated mass. The interactions between the atoms are described by force fields. The movements of the atoms are predicted by solving Newton's laws of motion. With MD simulation, the equilibrium and transport properties of a classical many-body system can be computed.

3.2.1 Molecular dynamics algorithm

The basic MD algorithm (Allen and Tildesley, 1989) is shown in Figure 3-1. An MD simulation is initiated by assigning atoms with initial coordinates and velocities. For each timestep (1~2 fs for atomistic MD simulations) of the simulation, the total force acting on an atom is defined as the negative gradient of the potential energy function. Once the forces acting on individual atoms are obtained, the atom coordinates and velocities are updated by integrating Newton's law of motion. The system properties of interest (energy, temperature, pressure, etc.) are computed, and the atoms' trajectories, which represents the time-dependent evolution of the system are saved during the simulation. The integration is repeated over a sufficient number of timesteps, so the thermodynamic properties fluctuate around constant average values and the system reaches equilibrium. The production run can only be started after equilibration. The system properties are sampled at regular intervals and averaged over the production run. at the end of the simulation.
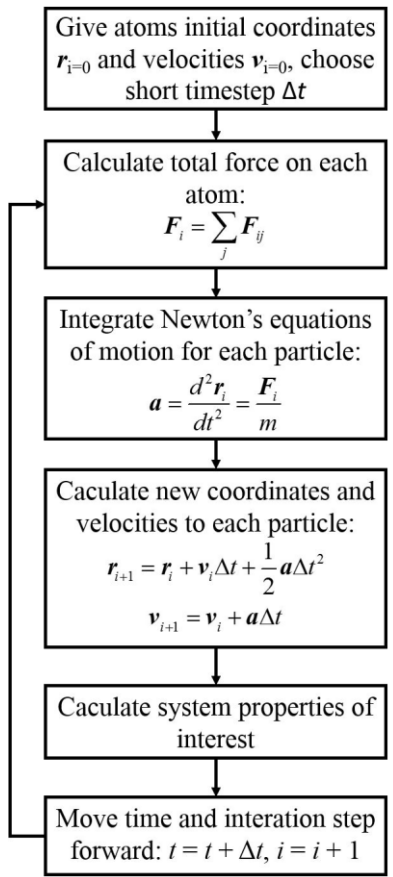
Figure 3-1 Simplified schematic of the molecular dynamics algorithm.

3.2.2 Force field

In the MD simulations, the interaction forces and energies between atoms in the system are usually evaluated using a classical potential energy function, the so-called force field. The basic functional form of a force field includes bonded terms and non-bonded terms. The general form for the total energy is written as:

$$U_{total} = U_{bonded} + U_{non\text{-}bonded} \tag{3.1}$$

The bonded terms describe the interactions of atoms that are linked by covalent bonds. The bonded potential energy is typically expressed as a sum of four components:

$$U_{bonded} = U_{bond} + U_{angle} + U_{dihedral} + U_{improper} \cdots\cdots\cdots\cdots\cdots\cdots\cdots \tag{3.2}$$

16

The bond (or stretching) term describes the interaction between two atoms connected by a chemical bond (Figure 3-2(a)) The most common potential to be used is the harmonic bond potential:

$$U_{\text{bond}} = k_{ij}(r_{ij} - r_0) \tag{3.3}$$

where the force constant, k_{ij}, and the equilibrium bond distance, r_{ij}, are defined for a bond connecting atoms of i and j.

The angle (or bending) term describes the interaction between three atoms connected in sequence by two chemical bonds (Figure 3-2(b)). The harmonic angle potential and the cosine harmonic angle potential are two common potentials to be used.

$$U_{\text{angle}} = k_{ijk}^{\text{H}}(\theta_{ijk} - \theta_0) \tag{3.4}$$

$$U_{\text{angle}} = k_{ijk}^{\text{CH}}(\cos\theta_{ijk} - \cos\theta_0) \tag{3.5}$$

where the force constant, k_{ijk}^{H} or k_{ijk}^{CH}, and the equilibrium angle, are defined for an angle of a series of atoms of i, j, and k.

As shown in Figure 3-2(c) and Figure 3-2(d), the dihedral (or torsion) term describes the interaction between four atoms connected in sequence by three chemical bonds. While the improper (or improper torsion) term describes the interaction between four atoms, in which three of the four atoms are connected to the fourth by three chemical bonds.
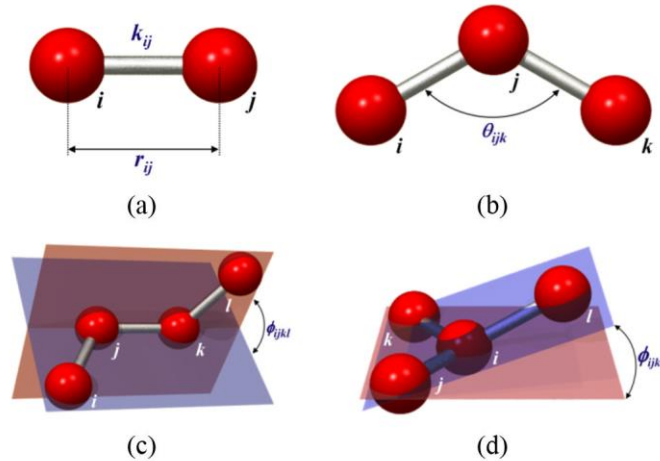
Figure 3-2 Illustration of different functional terms describing bonded interactions: (a) bond stretching (b) angle bending (c) torsion and (d) improper torsion (Images borrowed from http://cbio.bmt.tue.nl/pumma/index.php/Theory/Potentials)

The non-bonded term is used to describe the Van der Waals and the electrostatic interactions. The Lennard-Jones 12-6 potential is the most common potential to model the Van der Waals interactions and the electrostatic two-body interaction is expressed using Coulomb's law (Allen and Tildesley, 1989).

The non-bonded potential energy is described as:

$$U_{\text{non-bonded}} = U_{\text{VdW}} + U_{\text{Coul}} = 4\varepsilon_{ij} \left[\left(\frac{\sigma_{ij}}{r_{ij}} \right)^{12} - \left(\frac{\sigma_{ij}}{r_{ij}} \right)^{6} \right] + \frac{q_i q_j}{4\pi r_{ij}} \tag{3.6}$$

where ε_{ij} donates the depth of the potential well, σ_{ij} represents the distance at which the interaction energy of two atoms is minimal, r_{ij} is the distance between atoms i and j, q_i and q_j are the partial charges for atoms i and j, respectively.

The LJ potential consists of two parts: a steep repulsive term and a smoother attractive term (Figure 3-3). The part which contains the power 12 describes the repulsive forces between atoms

18

while the part which contains the power 6 denotes attraction. The LJ potential of two atoms is minimized at an equilibrium interatomic distance of $\sqrt[6]{2}\sigma$, where the potential energy U is -ε. Two interacting atoms repel each other when the distance between the atoms is smaller than their equilibrium distance. The atoms attract each other at a moderate distance, which is larger than the equilibrium distance, and do not interact at infinite distance.
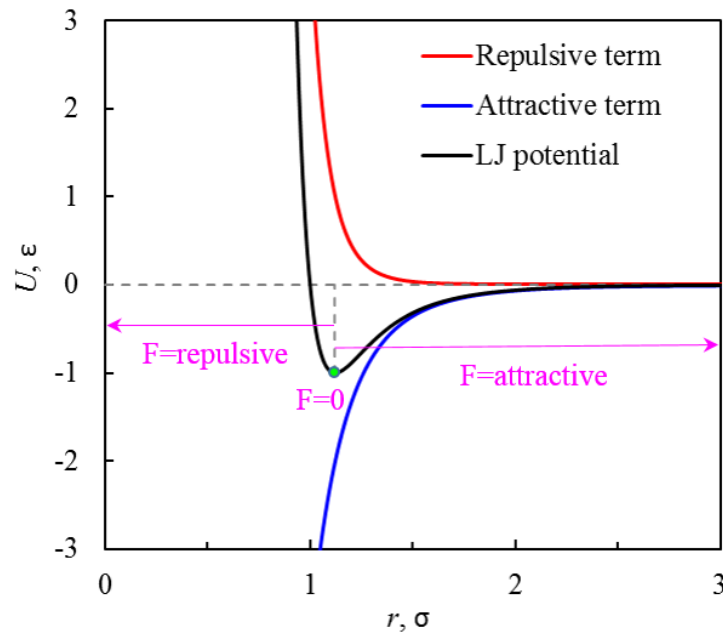
Figure 3-3 The LJ potential, attraction term only, and repulsion term only between atoms

The Lorentz−Berthelot mixing rules, $\varepsilon_{ij} = \sqrt{\varepsilon_{ii}\varepsilon_{jj}}$ and $\sigma_{ij} = (\sigma_{ii} + \sigma_{jj})/2$, or the geometric mean combining rule, $\varepsilon_{ij} = \sqrt{\varepsilon_{ii}\varepsilon_{jj}}$ and $\sigma_{ij} = \sqrt{\sigma_{ii}\sigma_{jj}}$, are usually applied to calculate the Van der Waals interactions between unlike atoms (Plimpton, 1995).

The Coulomb interaction potential determines the electrostatic force between charged atoms. The force is inversely proportional to the distance between two atoms squared ($F \propto 1/r^2$), and it is repulsive for atoms with like charges and attractive for atoms with opposite charges.

To speed up the simulation, the interactions between two atoms separated by a distance greater than the cutoff distance are ignored. As shown in Figure 3-3, the LJ potential is extremely small when the separation of two atoms is larger than 2.5σ. However, electrostatic interactions still have an impact beyond the system size. Different methods have been developed to add a constant term to the force field to compensate for the long-range electrostatic interactions. The main methods to deal with long-range electrostatic interactions are the Ewald summation method (Toukmaji A.Y. and Board J.A., 1996), the Particle-Particle Particle Mesh (PPPM) (Hockney and Eastwood, 1989) and the Multi-level Summation Method (MSM) (Hardy et al., 2009).

The choice of force field has a great impact on the validity of results from a molecular dynamics simulation. The parameters ε and σ, partial atomic charges, as well as the mixing rules should be carefully adjusted to accurately model different substances.

3.2.3 Ensembles

The three common types of ensembles in the MD simulations are the microcanonical ensemble (NVE), the canonical ensemble (NVT), and the isothermal-isobaric ensemble (NPT).

The microcanonical ensemble represents an isolated system. It is a system of a fixed number of particles (N), a constant volume (V), and constant total energy.

In the canonical ensemble, the number of particles (N), the volume (V), and the temperature (T) are fixed. The system is coupled to a heat bath, and exchanges energy with the heat bath to keep the temperature around the fixed value.

In the isothermal-isobaric ensemble, both the temperature (T) and pressure (P) are kept constant. The system is allowed to exchange energy with a heat bath of temperature and the volume can also change according to the pressure applied to the system.

20

3.2.4 Periodic boundary conditions

Although MD simulation is a powerful tool to obtain information that is not easily obtained from experiments, the atom numbers are still far below the real size of most systems. In order to conserve the macroscopic behavior of the system under investigation, periodic boundary conditions are most commonly applied in the MD simulations (Allen and Tildesley, 1989).

Figure 3-4 shows a two-dimensional schematic of periodic boundary conditions. The central box corresponds to the original system, and the other boxes are all exact replicas of the central box. If a particle moves in the central box, its periodic image in each of the replicated boxes moves in exactly the same way. If a particle leaves the central box, one of its images will enter through the opposite face. When calculating the interaction between a certain particle and any other particles, a cutoff distance is introduced. The dashed circle in Figure 3-4 represents the cutoff distance. Only the interactions with neighboring particles inside the cutoff distance are calculated. The interactions beyond the cutoff distance are small enough to be neglected.
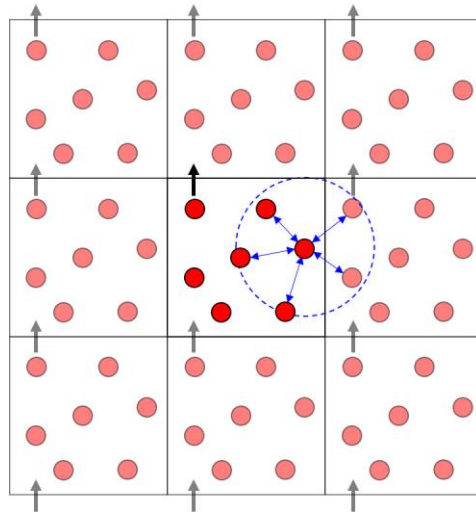
Figure 3-4 Schematic of periodic boundary conditions

3.3 Application of Molecular Simulation in Petroleum Engineering

Molecular simulation can be used to make comparisons with experimental measurements, predict experimental results, test new theories, and provide insights for designing and manufacturing of new materials. Moreover, for experiments that are difficult or dangerous to produce in laboratory conditions, the molecular simulation could be a better alternative to experimental studies. Molecular simulation methods have been widely used in the fields of biology, drug design, chemistry, and materials science. In petroleum engineering, molecular simulations have been used to investigate the properties of fluids and rock and their interactions at various conditions.

The properties of hydrocarbons have been extensively studied using molecular simulation methods. Different force fields, like OPLS-AA (Jorgensen et al., 1996; Siu et al., 2012), TraPPE (Martin and Siepmann, 1999, 1998), and NERD (Nath et al., 1998), have been developed to model the hydrocarbons. The density, vapor-liquid equilibrium, and viscosity are the main focused properties in many published studies (Herdes et al., 2018; López-Lemus et al., 2006; Papavasileiou et al., 2019; Ungerer et al., 2007). Molecular simulation can be used to investigate the hydrocarbon properties under extreme temperature and pressure conditions, which are difficult to achieve using current laboratory equipment. Moreover, the MD simulations have proven to be more reliable in predicting thermophysical properties than many classical thermodynamic models, which make predictions from the extrapolation of property trends (Ungerer1 et al., 2006). In fully atomistic MD simulation studies, pure alkane or alkane mixtures are commonly used to represent the crude oil. However, the composition of crude oil is complex, which contains normal and branched alkanes, cycloalkanes, aromatics, resins, and asphaltenes. Considering the current computational power, it is challenging to conduct a fully atomics MD simulation to simulate the real crude oil.

To deal with this problem, coarse-grained (CG) models have been built to simulate the complexity of crude oil (Herdes et al., 2015; Müller et al., 2015). In a coarse-grained molecular simulation, a group of atoms is represented by one bead, so the number of degrees of freedom is reduced and the fine interaction details are eliminated. The simulation of a CG system requires less computational resources and runs faster than that for the same system in all-atom representation. As a result, an increase of orders of magnitude in the simulated time and length scales can be achieved.

Molecular simulations have also been employed to study the interactions between injected fluids (gases and chemicals) and crude oil. The effect of CO_2 on the oil swelling (Liu et al., 2015; Zhang et al., 2013), viscosity reduction (Li et al., 2019b), and oil/water interfacial tension (IFT) (Liu et al., 2016; Makimura et al., 2013; Zhao et al., 2015) have been reported in the published studies. Other gases, like nitrogen (N_2), methane (CH_4), and ethane (C_2H_6), have also been studied using MD simulations in EOR-related researches, including IFT studies (De Lara et al., 2012) and the evaluation of minimum miscibility pressure (MMP) (Li et al., 2020; Peng et al., 2018). Among all the chemicals used in the oil fields, the surfactant is studied most. The self-assembly structure (Chun et al., 2015; Jalili and Akhavan, 2009; Ruiz-Morales and Romero-Martínez, 2018; Tang et al., 2014), surface adsorption (Cai et al., 2018; Hu et al., 2012; Wang and Larson, 2015), temperature sensitivity (Qu et al., 2016; Sammalkorpi et al., 2007), and salt resistance (Chen and Xu, 2013; Qu et al., 2016; Yan et al., 2010) of surfactants, as well as the effect of surfactant or surfactant/nanoparticles on the oil/water IFT (Li et al., 2019a; Shi et al., 2018; Vu and Papavassiliou, 2019), have been evaluated using molecular simulations.

Recently, the molecular simulation technique has been used increasingly to study fluid-rock systems. Molecular simulation can calculate water or oil contact angles on mineral slabs that are

not convenient to measure in laboratories (Chen et al., 2015; Šolc et al., 2011; Tenney and Cygan, 2014). For nanopore-dominated tight rocks, nanoscale phenomena are usually difficult to observe. MD simulation studies have focused on the investigation of oil and gas behavior and its transport properties in inorganic (De Almeida and Miranda, 2016; Wang et al., 2016a, 2016b; Zhang et al., 2016) and organic nanopores (Ho et al., 2018; Wang et al., 2015). Adopting MD simulation, the effect of injected gases (Fang et al., 2017; Yan et al., 2017b) and surfactant solutions (Tang et al., 2019) on the oil detachment in nanochannels have also been studied. The visualization of MD simulation results can be used to better understand the oil displacement in nanochannels.

CHAPTER 4

MOLECULAR SIMULATION STUDY ON THE VOLUME SWELLING AND THE VISCOSITY REDUCTION OF N-ALKANE/CO₂ SYSTEMS

4.1 Introduction

As one of the largest reserves of crude oil in the United States, the Bakken Formation plays a vital role in meeting the nation's energy needs. It has been reported that the Bakken Petroleum System in the Williston Basin has an estimated original oil in place (OOIP) of 300-900 billion barrels (Steven B. Hawthorne et al., 2019; Jia et al., 2019). However, the primary recovery factors are only estimated to be less than 10% due to the ultra-low matrix permeability (Clark, 2009; LeFever and Helms, 2006). Hence, a considerable amount of oil will remain in the reservoir, resulting in an urgent need for effective enhanced oil recovery (EOR) techniques. Since the Bakken Formation has huge original oil in place, small improvements in the oil recovery factor would result in significant volumes of produced oil.

Resulting in incremental oil recovery as well as reducing Carbon dioxide (CO_2) emission (Suebsiri et al., 2006), CO_2 injection has become one of the most common enhanced oil recovery (EOR) techniques in North America. Many CO_2 injection projects have been successfully carried out in Texas, New Mexico, and Colorado (Alvarado and Manrique, 2010; Kuuskraa et al., 2013; Manrique et al., 2007). In recent years, the Middle Bakken Formation of the Williston Basin in North Dakota has become the interest of CO_2 EOR. The Middle Bakken Formation is a typical tight formation, which holds a huge CO_2 storage capacity and the potential of significantly increasing oil production by injecting CO_2 (Sorensen et al., 2014). The predicted recovery factor of primary oil recovery is less than 10% (Clark, 2009; LeFever and Helms, 2006) while using CO_2 injection technique 2.5%−9.4% incremental oil recovery factor can be obtained (Yu et al., 2015).

The swelling of crude oil by dissolved CO_2 and reduction of crude oil viscosity are two main physical mechanisms of the CO_2 EOR method (Orr et al., 1982; Seyyedsar et al., 2017). When CO_2 is injected into a reservoir and contacts the crude oil, the dissolution of CO_2 occurs thereby causing swelling and density reduction. The swollen oil droplets will increase oil saturation and the reservoir pressure. Some trapped oil will be forced out of the pore spaces and move toward the fractures or the production well. Thus additional oil can be recovered from reservoirs. The system expansion process can reduce crude oil viscosity significantly, and therefore increase the mobility of crude oil.

Some experiments (Dong et al., 2018; Han et al., 2015; Mosavat et al., 2014; Yang et al., 2012; Zheng et al., 2016) focusing on the CO_2 dissolution and swelling effect have been carried out, and various models and correlations (Chung et al., 1988; Mac ías-Salinas et al., 2013; Mulliken and Sandler, 1980; Simon and Graue, 1964) have been built to predict CO_2 solubility, crude oil/CO_2 mixture viscosity, oil swelling factor, etc. However, experimental studies are often time-consuming, costly, and cannot cover all the conditions, especially for CO_2-crude oil interactions in micro- and/or nano-pore spaces in tight formations. Although models and correlations can predict many parameters easily, they cannot explain different phenomena scientifically and thoroughly.

Over the last few years, molecular simulation methods including the Monte Carlo (MC) method and the Molecular Dynamics (MD) method have been widely used to study the gas solubility and diffusion coefficient in liquids, and the viscosity of gas/liquid mixtures (Liu, B. et al., 2015, Liu, H. et al., 2014; Moultos et al., 2016; Urukova et al., 2009; Vorholz et al., 2004; Zhang et al., 2013). Zhang et al. (2013) provided a reasonable method to study the CO_2 solubility in octane and the swelling of the octane/CO_2 system with MC simulation. Liu, B. et al. (2015) used

MD simulation to investigate the effects of temperature, pressure, and alkane structures on the swelling of alkane/CO_2 systems. They inferred that the dispersion interaction is the main reason for the swelling of the alkane/CO_2 system. Moultos et al. (2016) studied the CO_2 diffusivity in various hydrocarbons and reproduced the liquid viscosities with three different force fields.

While the minimum miscibility pressure (MMP) between Bakken crude oil and CO_2 as well as CO_2 flow in tight Bakken rocks were studied (Hawthorne et al., 2017; Sorensen et al., 2014, 2017), more work needs to be done on the solubility of CO_2 in Bakken crude oil, the swelling factors of crude oil/CO_2 system, and the crude oil viscosity reduction. In this study, five main n-alkanes (octane, decane, dodecane, tetradecane, and hexadecane) in Middle Bakken crude oil (Kurtoglu, 2014) were selected and a series of configurational-bias Monte Carlo (CBMC) (Frenkel et al., 1992; Siepmann and Frenke, 1992) simulations were performed to study the impacts of pressure, temperature and alkyl chain length on the solubility of CO_2 in different n-alkanes and the swelling of n-alkane/CO_2 systems. MD simulations were carried out to study the viscosity reduction of n-alkanes due to the dissolution of CO_2. The main temperature employed in our simulations is 383 K, which is consistent with the reported experimental study (Hawthorne et al., 2017; Sorensen et al., 2014, 2017).

4.2 Force Fields and Simulation Details

4.2.1 Force fields

The non-bonded interactions for the force fields employed in this work were described by the pairwise additive Lennard-Jones (LJ) 12-6 potentials and the Coulombic interactions.

In the CBMC simulations, the nonpolar, flexible chain n-alkane molecules were described by the transferable potentials for phase equilibria united atom (TraPPE-UA) model (Martin and

Siepmann, 1998, 1999), in which methyl (CH_3) and methylene (CH_2) groups were treated as pseudo atoms. The Lorentz-Berthelot combining rules were used to determine the cross-parameters for unlike-pair interactions. While in the MD simulations, the L-OPLS-AA force field (Siu et al., 2012) was selected to describe the n-alkanes, as this force field is more accurate in reproducing the viscosity of long-chain alkanes (Ewen et al., 2016). The unlike interactions were evaluated using the geometric mean combining rule. The CO_2 molecules were described by the TraPPE model (Potoff and Siepmann, 2001) with two rigid bonds and a rigid bond angle.

The non-bonded and bonded parameters for each of the force fields used in this work are listed from Table 4-1 to Table 4-4.

Table 4-1 Parameters for non-bonded interactions used in CBMC simulations

atom/group	q_i (e)	σ_{ii} (Å)	ε_{ii} (kcal·mol^{-1})
CH_3	0	3.75	0.195
CH_2	0	3.95	0.0914
C	0.70	2.80	0.0537
O	-0.35	3.05	0.157

Table 4-2 Parameters for bonded interactions used in CBMC simulations

Stretch	r_0 (Å)	k_b(kcal·mol^{-1}·Å^{-2})
CH_x-CH_y	1.54	191.77
C−O	1.16	-
Bend	θ_0 (°)	k_θ (kcal·mol^{-1}·rad^{-2})
$CH_x-CH_2-CH_y$	114.0	124.20

C−O−C	180.0		-

Torsion	C_1(kcal·mol^{-1})	C_2(kcal·mol^{-1})	C_3(kcal·mol^{-1})	C_4(kcal·mol^{-1})
CH_x−CH_2−CH_2−CH_y	0	0.666	-0.136	1.573

Note: x = 2 or 3, y = 2 or 3.

Table 4-3 Parameters for non-bonded interactions used in MD simulations

atom	q_i (e)	σ_{ii} (Å)	ε_{ii} (kcal·mol^{-1})
CT_CH_3	-0.222	3.50	0.066
CT_CH_2	-0.148	3.50	0.066
HC_CH_3	0.074	2.50	0.03
HC_CH_2	0.074	2.50	0.0263
C	0.70	2.80	0.0537
O	-0.35	3.05	0.157

Table 4-4 Parameters for bonded interactions used in MD simulations

Stretch	r_0 (Å)	k_b(kcal·mol^{-1}·Å^{-2})
CT-CT	1.529	268.0
CT-HC	1.090	340.0
C−O	1.16	-
Bend	θ_0 (°)	k_θ (kcal·mol^{-1}·rad^{-2})
CT-CT-CT	112.7	58.35
CT-CT-HC	110.7	37.5
HC-CT-HC	107.8	33.0

| | 180.0 | | - |

Torsion	C_1(kcal·mol^{-1})	C_2(kcal·mol^{-1})	C_3(kcal·mol^{-1})	C_4(kcal·mol^{-1})
CT-CT-CT-CT	0.645	-0.214	0.178	0.000
CT-CT-CT-HC	0.000	0.000	0.300	0.000
HC-CT-CT-HC	0.000	0.000	0.300	0.000

(Note: first row is C−O−C 180.0 -)

4.2.2 Simulation details

The CBMC simulations were performed with a fixed number of 100 n-alkane molecules in a cubic unit cell for both pure and CO_2 saturated n-alkane systems. The Monte Carlo moves of n-alkane molecules were translation, rotation, and reinsertion. The relative frequency of the three moves was 1:1:1. For CO_2 saturated n-alkane systems, with the insertion and deletion of CO_2 molecules, the systems reached equilibrium at specified temperatures and pressures. The Monte Carlo moves of CO_2 molecules were translation, rotation, reinsertion, and swap. The relative frequency of the four moves was 1:1:1:1. The grand canonical (μVT) ensemble (Dubbeldam et al., 2004; Zhang et al., 2013) was employed for the simulations of CO_2 saturated n-alkane systems. In this ensemble, the temperature, T, the volume, V, and the chemical potential, μ, were fixed. The system volume was allowed to change when the n-alkane was absorbing/desorbing CO_2. The volume change probability was set as 0.05. A truncated and shifted potential with a cutoff radius of 12Å was used. The number of initialization cycles and production cycles was 10000 and 50000, respectively. The simulations were performed for a pressure range of 2−10 MPa and a temperature range of 323−383 K. Finally, the average values of the properties of interest were calculated and analyzed.

Equilibrium molecular dynamics (EMD) simulations were used in conjunction with the Green-Kubo relation (Green, 1954; Kubo, 1957) (Equation 4.1) to compute the shear viscosity of the n-alkane/CO_2 systems.

$$\eta(t) = \frac{V}{k_B T} \int_0^\infty \left\langle P_{\alpha\beta}(t_0) P_{\alpha\beta}(t_0 + t) \right\rangle dt \tag{4.1}$$

where V is the volume of the simulation box, k_B is the Boltzmann constant, T is the temperature, $P_{\alpha\beta}$ denotes the off-diagonal components of the pressure tensor, and the angle brackets indicate the ensemble average.

One hundred twenty-five n-alkane molecules and CO_2 molecules with different mole fractions were randomly placed in a cubic box. Then the box was equilibrated in the isothermal-isobaric (NPT) ensemble for 3 nanoseconds (ns). The average volume of the simulation box during the final 1.0 ns was calculated and employed in the following 5 ns canonical ensemble (NVT) simulation. The viscosity was finally obtained from the last 2 ns NVT production run based on three independent trajectories. The long-range electrostatic interactions were calculated using the particle-particle particle-mesh (PPPM) method (Hockney and Eastwood, 1989) with an accuracy of 10^{-5} and a cutoff radius of 14 Å. The Nosé−Hoover thermostat and barostat (Hoover et al., 1982; Nosé, 1984) were applied to control the temperature and pressure, respectively. Fast-moving bonds involving hydrogen atoms were constrained with the SHAKE algorithm (Ryckaert et al., 1977), and the time step was set to 2 femtoseconds (fs).

All CBMC simulations were carried out with the open source package RASPA 2.0 (Dubbeldam et al., 2016). The MD simulations were performed using the LAMMPS package (Plimpton, 1995). The configuration snapshots were rendered by VMD software (Humphrey et al., 1996). The snapshots of the systems simulated in this work are shown in Figure 4-1.
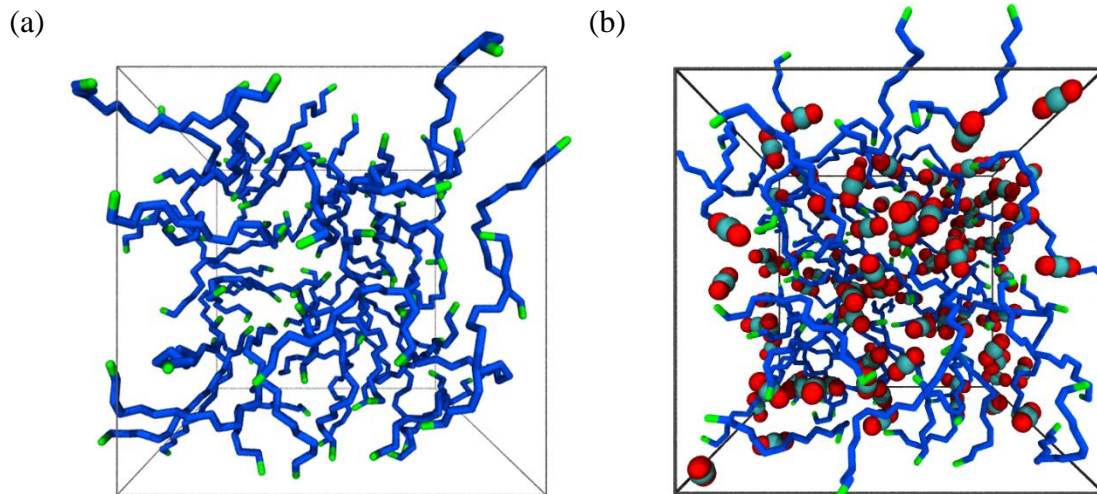
Figure 4-1 Simulation unit cells of (a) pure and (b) CO_2 saturated hexadecane: green and blue tubes represent the CH_3 group and CH_2 group, respectively; red and cyan spheres represent O atoms and C atoms, respectively.

4.3 Results and Discussion

4.3.1 CO_2 solubility in n-alkanes.

The solubility of CO_2 in each n-alkane as a function of pressure and temperature is presented in Figure 4-2 and Figure 4-3, respectively. For each n-alkane, the solubility of CO_2 increases with the increasing pressure and decreases with the increasing temperature. As shown in Figure 2, at 383 K, the solubility of CO_2 in n-alkanes with different alkyl chain lengths varies slightly at a low pressure (2 MPa), while CO_2 is more soluble in n-alkanes with shorter alkyl chain length at a high pressure (10 MPa). The standard deviations of CO_2 solubility in the five n-alkanes are 0.93, 2.59, 4.46, 7.93, and 13.14, respectively, at the pressure range of 2−10 MPa, and the temperature of 383 K. At 383 K and 10 MPa, the solubility of CO_2 in n-octane is 2.09 times the solubility of CO_2 in n-hexadecane. Similarly, under the same pressure condition (6 MPa), the difference in solubility

of CO_2 in n-alkanes between short-chain n-alkanes and long-chain n-alkanes at a low temperature (323 K) is much larger than that at a high temperature (383 K), as shown in Figure 3. The standard deviations of CO_2 solubility in the five n-alkanes are 15.66, 7.21, and 4.46, respectively, at the temperature range of 323−383 K, and the pressure of 6 MPa. At 323 K and 6 MPa, the solubility of CO_2 in n-octane is 1.92 times the solubility of CO_2 in n-hexadecane.
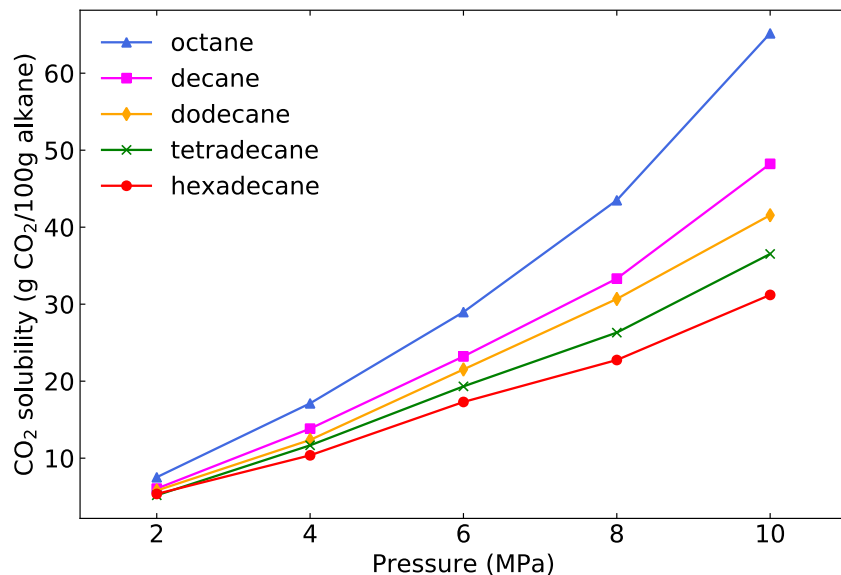
Figure 4-2 CO_2 solubility in n-alkanes as a function of pressure at 383 K.
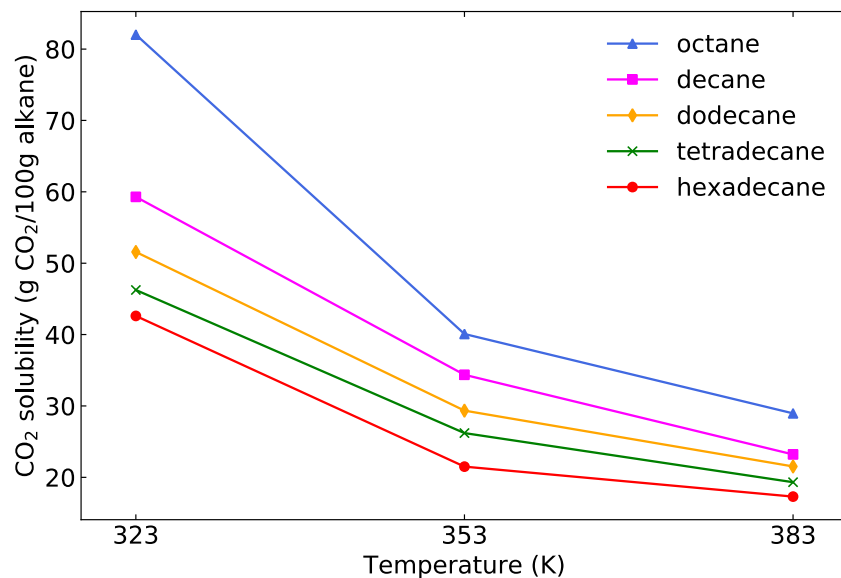
Figure 4-3 CO$_2$ solubility in n-alkanes as a function of temperature at 6 MPa.

4.3.2 Density of pure n-alkanes and CO$_2$-saturated n-alkanes.

The simulated density values of the pure n-alkanes are consistent with the experimental data provided in the National Institute of Standards and Technology (NIST) database (Lemmon et al., 2011). As shown in Figure 4-4 and Figure 4-5, the density of pure n-alkanes increases slightly with the increasing pressure and the decreasing temperature, while the density of CO$_2$-saturated n-alkanes decreases dramatically with the increasing pressure and the decreasing temperature. The reason for this phenomenon can be explained by the impacts of pressure and temperature on the solubility of CO$_2$ in n-alkane. With the increasing pressure and the decreasing temperature, more CO$_2$ can dissolve in n-alkane resulting in the expansion of the n-alkane, and thus the density of the n-alkane decreases.
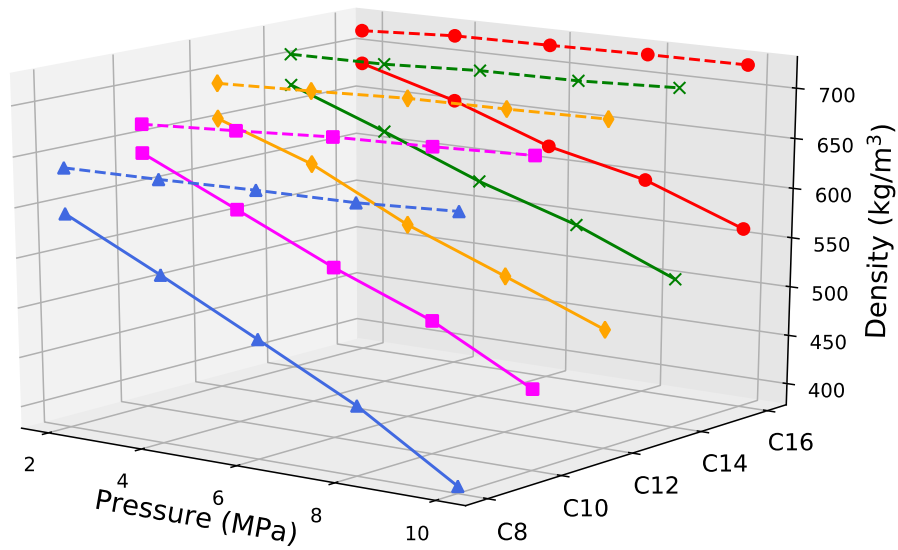
Figure 4-4 Density of pure (dashed lines) and CO$_2$ saturated (solid lines) n-alkanes as a function of pressure at 383K.
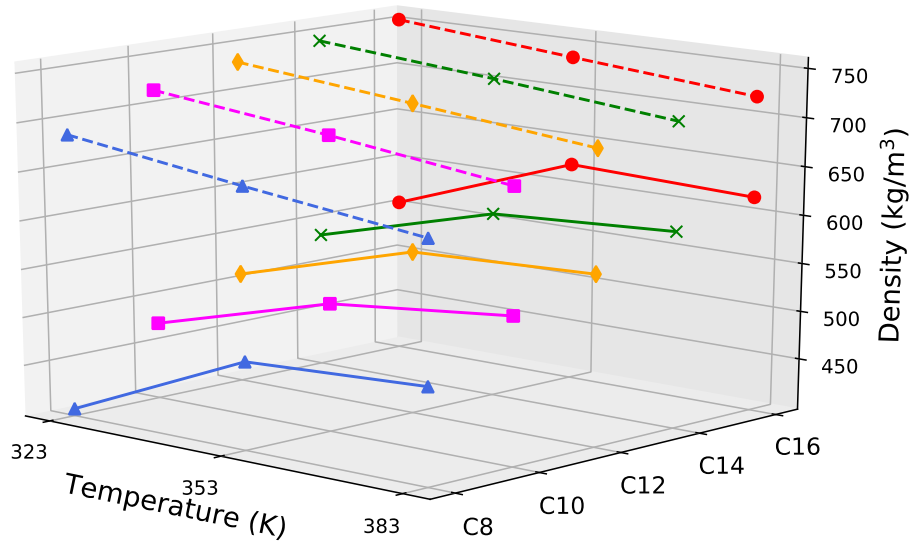
Figure 4-5 Density of pure (dashed lines) and CO_2 saturated (solid lines) n-alkanes as a function of temperature at 6 MPa.

4.3.3 Swelling factor of n-alkanes−CO_2 systems.

The swelling factor, an important indicator for quantifying the oil swelling when CO_2 dissolves into oil, is defined as the volume of the saturated CO_2-oil mixture divided by the volume of the oil alone (Orr et al., 1982). The swelling factor of n-alkanes/CO_2 system as a function of pressure and temperature is presented in Figure 4-6 and Figure 4-7. The swelling factor of n-alkanes/CO_2 system increases with the increasing pressure and the decreasing temperature, which is consistent with the CO_2 solubility in n-alkanes. N-alkanes with a shorter chain length have a higher swelling factor when saturated with CO_2, which indicates that light oil has a higher swelling factor than heavy oil.

35
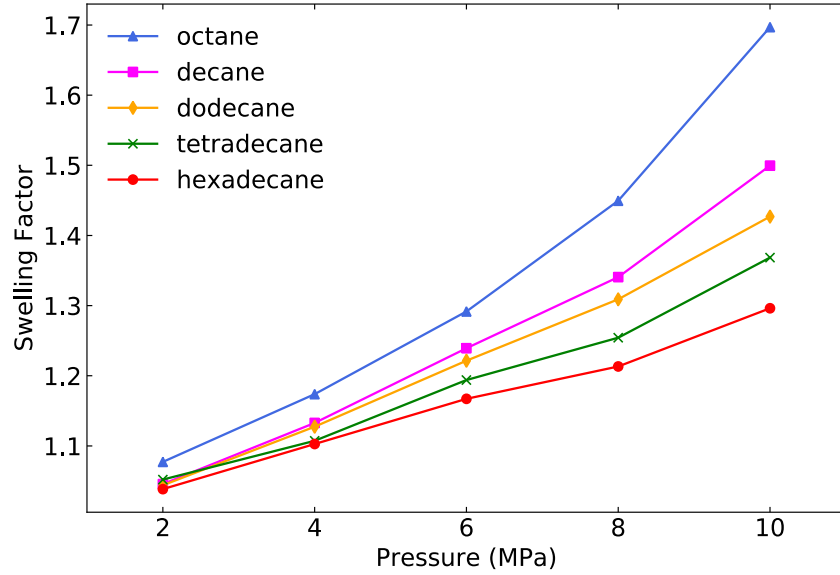
Figure 4-6 Swelling factor of n-alkane/CO_2 system as a function of pressure at 383 K.
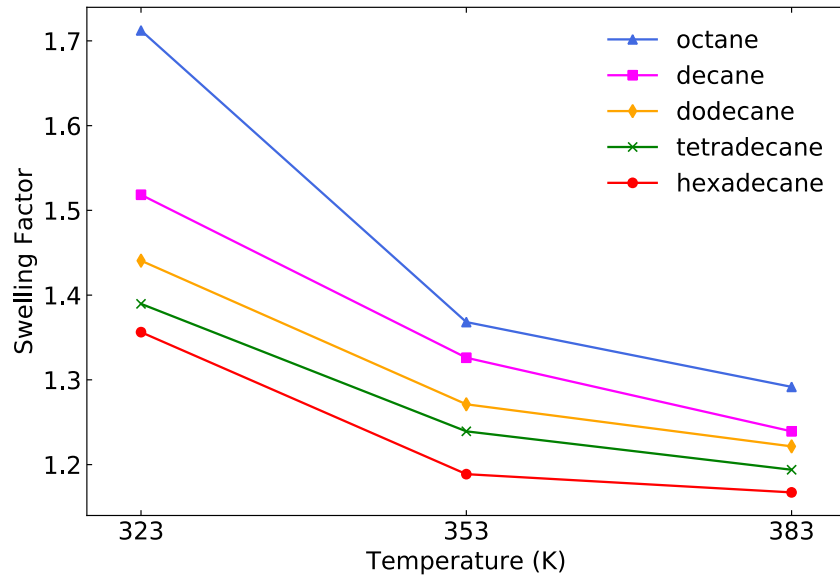
Figure 4-7 Swelling factor of n-alkane/CO_2 system as a function of temperature at 6 MPa.

4.3.4 Interaction energy.

As the n-alkane molecule and CO_2 molecule are both nonpolar, the intermolecular forces both belong to the London dispersion force, we would expect they are soluble in each other. The

interactions of these molecules arises solely from the dispersion energy, which will be referred to as "interaction energy" in this dissertation. The interaction energy of pure n-alkanes at specified pressures and temperatures are calculated, as shown in Figure 4-8. The n-alkanes with shorter chains have less negative intermolecular interaction energy, which means it is easier for molecules to separate from each other, so a higher swelling factor can be observed when octane is saturated with CO_2.

The interaction energy of n-alkane−n-alkane, CO_2−CO_2, and n-alkane−CO_2 in the n-alkane/CO_2 system are also analyzed. Taking hexadecane (Figure 4-9) for example, the interaction energy between hexadecane and CO_2 molecules becomes more negative with the increasing pressure, while the interaction energy between hexadecane molecules becomes less negative. This is because more CO_2 molecules dissolve in the hexadecane and occupy the intermolecular space of hexadecane molecules.
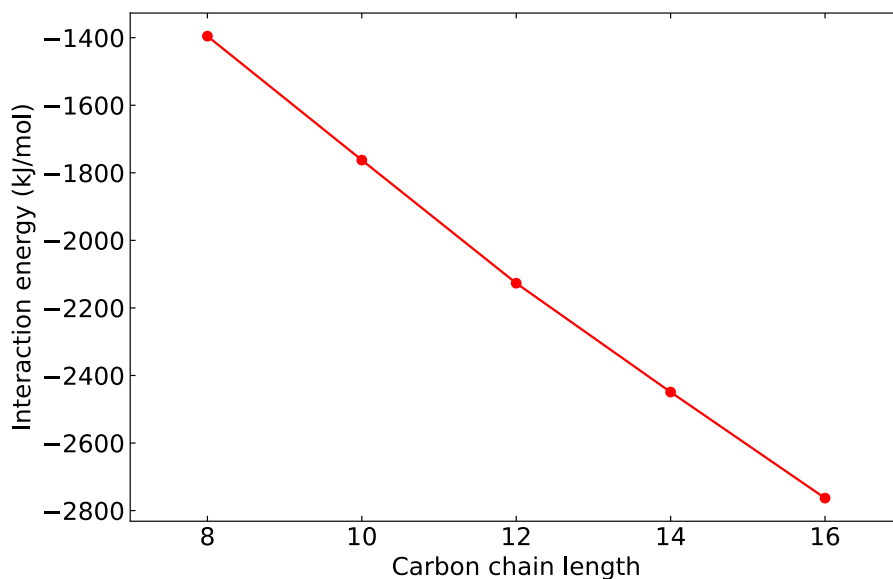
Figure 4-8 Interaction energy of pure n-alkane molecules at 383 K and 10 MPa.
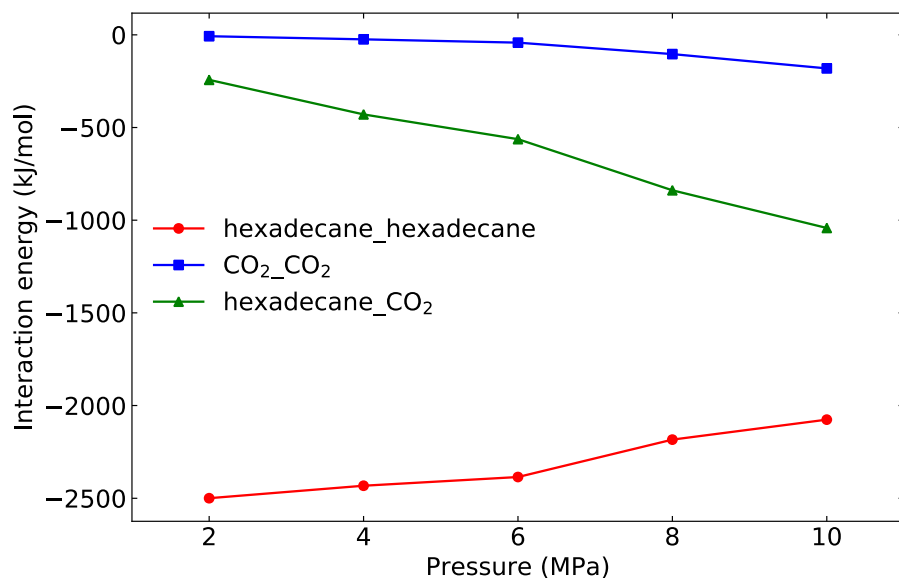
Figure 4-9 Interaction energy as a function of pressure in hexadecane/CO_2 system at 383 K.

4.3.5 Viscosity reduction of n-alkane/CO_2 system.

The viscosities of pure n-alkanes and CO_2 at 383 K and 35MPa are computed and compared with the experimental data in the NIST database (Lemmon et al., 2011). All the simulation results are in good agreement with the NIST data, yielding a viscosity value within 4% of the experimental one (except 9.5% for dodecane), as shown in Figure 4-10.
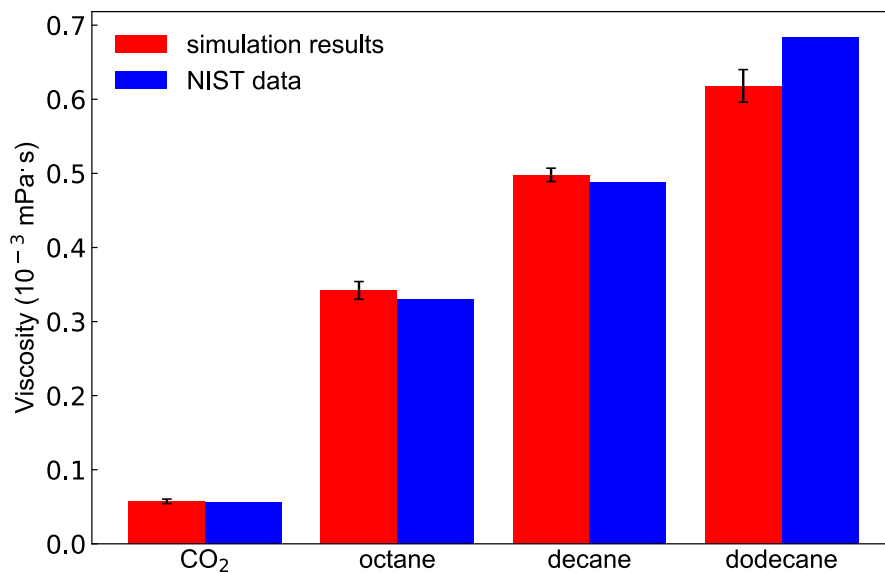
Figure 4-10 Interaction energy as a function of pressure in hexadecane/CO_2 system at 383 K.

With the increase of the CO_2 mole fraction, the viscosity of the n-alkane/CO_2 system is reduced (Figure 4-11). The viscosity and the CO_2 mole fraction are approximately in a linear relationship. The slopes of these viscosity trend lines (dotted lines in Figure 4-11) show that the n-alkanes with longer alkyl chains have a larger viscosity reduction with increasing CO_2 mole fraction. The average viscosity reduction rate is about 45% when the CO_2 mole fraction is 60%.
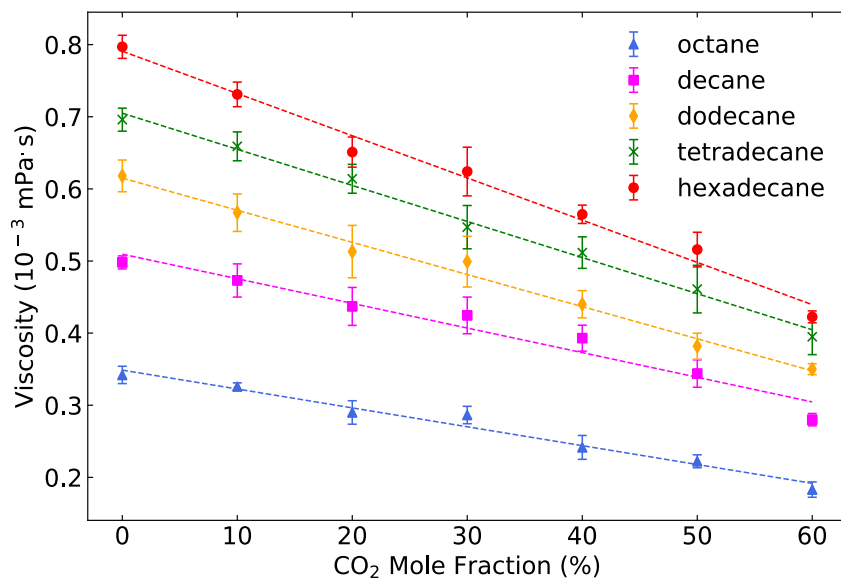
Figure 4-11 Viscosity of n-alkane/CO_2 system as a function of CO_2 mole fraction at 383 K and 35 MPa.

4.4 Conclusions

In this study, the CBMC simulations and the MD simulations were carried out to investigate the volume swelling and the viscosity reduction of the n-alkane/CO_2 systems. Results from the CBMC simulation indicate that pressure, temperature, and oil composition are the main factors impacting the CO_2 solubility, and the density and swelling factor of the n-alkane/CO_2 system. Both

the CO_2 solubility and the swelling factor of the n-alkane/CO_2 system increase with the increasing pressure and the decreasing temperature. The CO_2 solubility and swelling effect are more pronounced in light oil. The pressure and the temperature have a negligible effect on the density of pure n-alkanes, while the density of CO_2-saturated n-alkanes decreases dramatically with the increasing pressure and the decreasing temperature. The interaction energy between n-alkanes and CO_2 can reasonably explain the swelling process.

The MD simulation results show that the viscosity of the n-alkane/CO_2 system is approximately in an inversely proportional relationship with the mole fraction of dissolved CO_2. The average viscosity reduction rate is about 45% when the CO_2 mole fraction is 60% under the reservoir condition.

Molecular simulation study provides better insights into the interactions between oil components and CO_2 at the molecular level. The application of molecular simulation methods can play an important role in interpreting experimental results and providing guidance for practical oil recovery processes in the Bakken Formation.

CHAPTER 5

INTERFACIAL INTERACTIONS BETWEEN BAKKEN CRUDE OIL AND INJECTED GASES AT RESERVOIR TEMPERATURE: A MOLECULAR DYNAMICS SIMULATION STUDY

5.1 Introduction

Carbon dioxide (CO_2) EOR has been proven to be a successful technology in conventional reservoirs (Perera et al., 2016; Qin et al., 2015). CO_2 can mobilize the oil through swelling the oil, extracting hydrocarbons, and reducing oil viscosity (Abedini and Torabi, 2014; Orr et al., 1982). The injection of CO_2 into oil reservoirs results in incremental oil recovery as well as CO_2 capture and storage, which can significantly reduce greenhouse gas emissions to the atmosphere (Abedini and Torabi, 2014; Aycaguer et al., 2001; Gaspar Ravagnani et al., 2009). Studies have reported that total organic carbon (TOC) can significantly affect the storage and transportation of crude oil (Zhang et al., 2020) as well as CO_2 storage capacity (Pan et al., 2018). Low-TOC shale is more suitable as a caprock, while high-TOC shale provides a large CO_2 sink via adsorption trapping (Arif et al., 2017). The rock samples in the Middle Bakken are typical inorganic rocks with the main minerals of quartz, dolomite, feldspar, and calcite (Steven B. Hawthorne et al., 2019; Zhang et al., 2019). TOC content of the Middle Bakken Formation ranges from 0.1 to 0.4 percent by weight (Steven B. Hawthorne et al., 2019). As a typical tight formation, the Bakken Formation holds a huge CO_2 storage capacity and the potential of significantly increasing oil production by injecting CO_2 (Sorensen et al., 2014). Both experimental studies and numerical simulations have shown that CO_2 injection could be an effective EOR method to improve the oil recovery in tight formations (Kurtoglu, 2014; Kurtoglu et al., 2013; Sorensen et al., 2015; Yu et al., 2015).

Although CO_2 EOR is a very successful and mature technology in the U.S., many reservoir targets like the Bakken Formation have not been flooded because of limited low-cost CO_2 supply.

41

In addition, wells in the Bakken Formation produce large amounts of natural gas, which is often flared off. This flaring not only wastes energy, but it also emits large amounts of greenhouse gas, carbon dioxide. Some experimental studies have focused on using hydrocarbon gas as a working fluid for EOR in the Bakken Formation (Steven B Hawthorne et al., 2019; Jin et al., 2016). Hydrocarbon gas injection can improve oil recovery as well as reduce CO_2 emissions from gas flaring. It has been successfully employed in the North Sea oil fields for several decades (Awan et al., 2008).

Many experimental studies have been carried out to investigate the EOR potentials of different gases such as nitrogen (N_2) (Assef and Almao, 2019), CO_2 (Hawthorne and Miller, 2019; Li et al., 2017), and hydrocarbon gases (Steven B Hawthorne et al., 2019; Hawthorne and Miller, 2019; Li and Sheng, 2016). Interactions between crude oil and injecting gas play an important role in gas solubility, viscosity reduction, swelling factor, and oil extraction. However, from the laboratory studies, it is still a challenge to observe microscopic interactions. Over the past few decades, molecular simulation methods including Monte Carlo (MC) simulations and molecular dynamics (MD) simulations have been applied to study the gas EOR processes. Compared with experiments, molecular simulations are more efficient and economical to obtain microscopic properties. Zhang et al. (Zhang et al., 2013) studied the CO_2 solubility in octane and its effect on octane swelling from MC simulations. The simulation results indicate that the interaction between octane and CO_2 is the main cause of octane swelling. Using both MC and MD simulations, Li et al. (Li et al., 2019b) investigated the volume swelling and the viscosity reduction of n-alkane/CO_2 systems. N-Alkanes with different alkyl chains were studied under various pressure and temperature conditions. De Lara, L. S. et al. (De Lara et al., 2012) analyzed the interfacial tension (IFT) of fluid/oil interfaces and the self-diffusion coefficients of components in the systems. The

simulations suggest an increase in the fluid diffusion in the oil phase as the IFT reduces. The adsorption and translocation of supercritical CO_2/hydrocarbons in mineral nanopores also have been studied from MD simulations by many researchers(Le et al., 2016, 2015; B. Liu et al., 2017; Simoes Santos et al., 2018). The strong interactions between CO_2 molecules and mineral surfaces result in the detachment of hydrocarbon molecules from the surfaces. An enhancement of hydrocarbon diffusivity can be obtained with increasing dissolved CO_2 molecules.

The CO_2 related molecular simulations have been extensively studied, while few MD simulation studies focus on the interactions between methane (CH_4) or ethane (C_2H_6) and hydrocarbons. As each of these gases has the potential to improve the oil recovery in the Bakken Formation, studies should be done to optimize the injected fluid. In this work, to evaluate the abilities of CO_2, CH_4 and C_2H_6 for mobilizing and recovering crude oil, a series of MD simulation systems were built to study the interfacial interactions between Bakken crude oil and gases at Bakken reservoir temperature (383 K). The gas solubility, swelling factor, diffusion coefficient, and minimum miscibility pressure (MMP) were investigated.

5.2 Models and Methodology

5.2.1 Molecular models

Based on the dead Bakken oil components proposed by Hawthorne et al. (Hawthorne et al., 2016), a quaternary system (C_6 + C_{10} + C_{19} + C_{30}) was chosen to represent the crude oil (Figure 5-1). The crude oil model has been successfully used for estimating the MMPs of the CO_2−Bakken oil system (Peng et al., 2018).
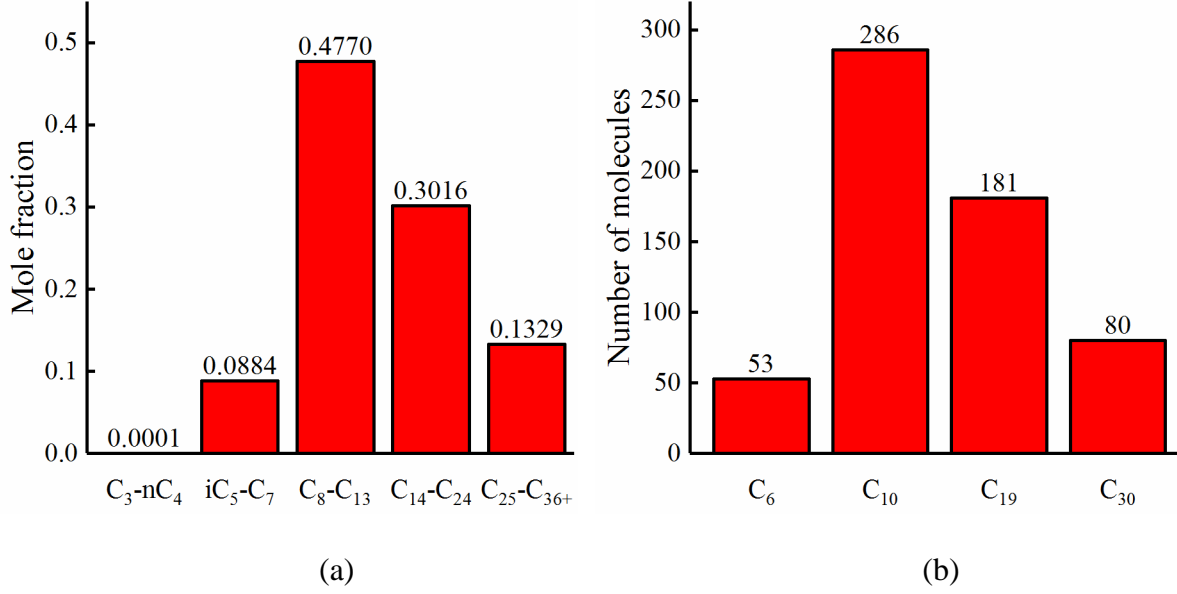
Figure 5-1 (a) Dead Bakken oil composition, (b) crude oil model in MD simulations

Figure 5-2 shows the molecules and the crude oil model used in the simulations. The force field for CO_2 was taken from the work of Zhu et al. (Zhu et al., 2009), and CH_4 was modeled using the TraPPE-UA force field (Martin and Siepmann, 1998), while the NERD force field (Nath et al., 1998) was used for all other alkanes. The non-bonded interactions between atoms were described by the pairwise additive Lennard-Jones (LJ) 12-6 potentials and the Coulombic interactions,

$$U\left(r_{ij}\right)=4\varepsilon_{ij}\left[\left(\frac{\sigma_{ij}}{r_{ij}}\right)^{12}-\left(\frac{\sigma_{ij}}{r_{ij}}\right)^{6}\right]+\frac{q_i q_j}{4\pi r_{ij}} \tag{5.1}$$

where ε_{ij} represents the depth of the potential well, σ_{ij} represents the distance at which interaction energy of two particles is minimal, r_{ij} is the distance between particles i and j, q_i and q_j are the partial charges for particles i and j, respectively.

Unlike-atom interactions were calculated using the modified Lorentz-Berthelot combining rules (Wang et al., 2018)

44

$$\sigma_{ij} = \frac{\sigma_{ii} + \sigma_{jj}}{2} \tag{5.2}$$

$$\varepsilon_{ij} = a\sqrt{\varepsilon_{ii}\varepsilon_{jj}} \tag{5.3}$$

Here, a = 0.9 was adopted for CO_2-alkanes interactions, while a = 1 for all other interactions.
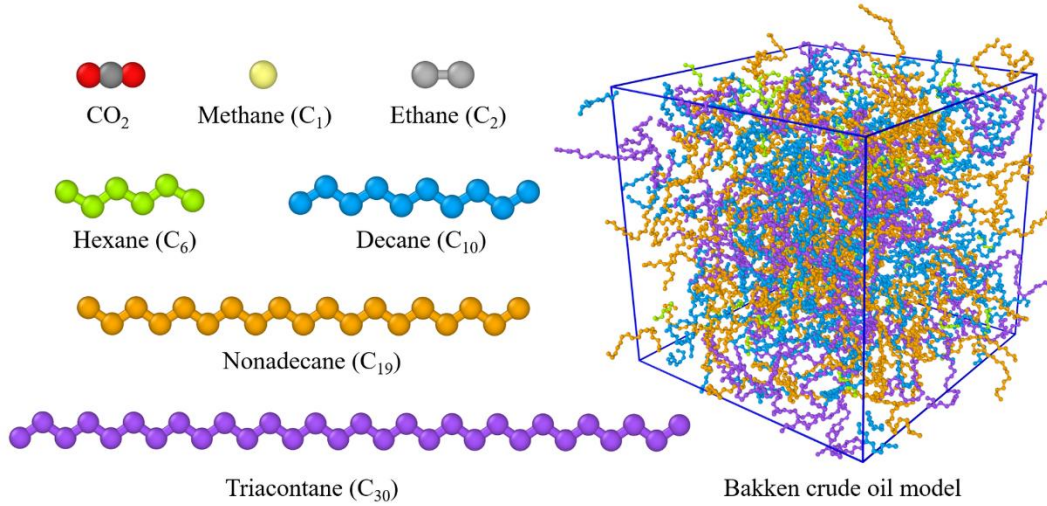
Figure 5-2 Various molecules used in the simulations and a snapshot showing the Bakken crude oil model. In the CO_2 molecule, gray and red particles represent C and O atoms, respectively. In the alkane molecules, particles represent methyl (−CH₃) groups or methylene (−CH₂) groups. For clarity, different color codes were employed.

5.2.2 Simulation details

Figure 5-3 shows the simulation cells for the injected gases and crude oil system. The simulation cell was set as a rectangular box with dimensions $L_x \times L_y \times L_z$, where $L_x = L_y = 6$ nm and $L_z = 35$ nm. Periodic boundary conditions were used in all directions. Initially, each simulation cell consists of a slab of crude oil in the middle and different numbers of gas molecules on both sides. The pressure of the system was changed by adjusting the number of gas molecules.
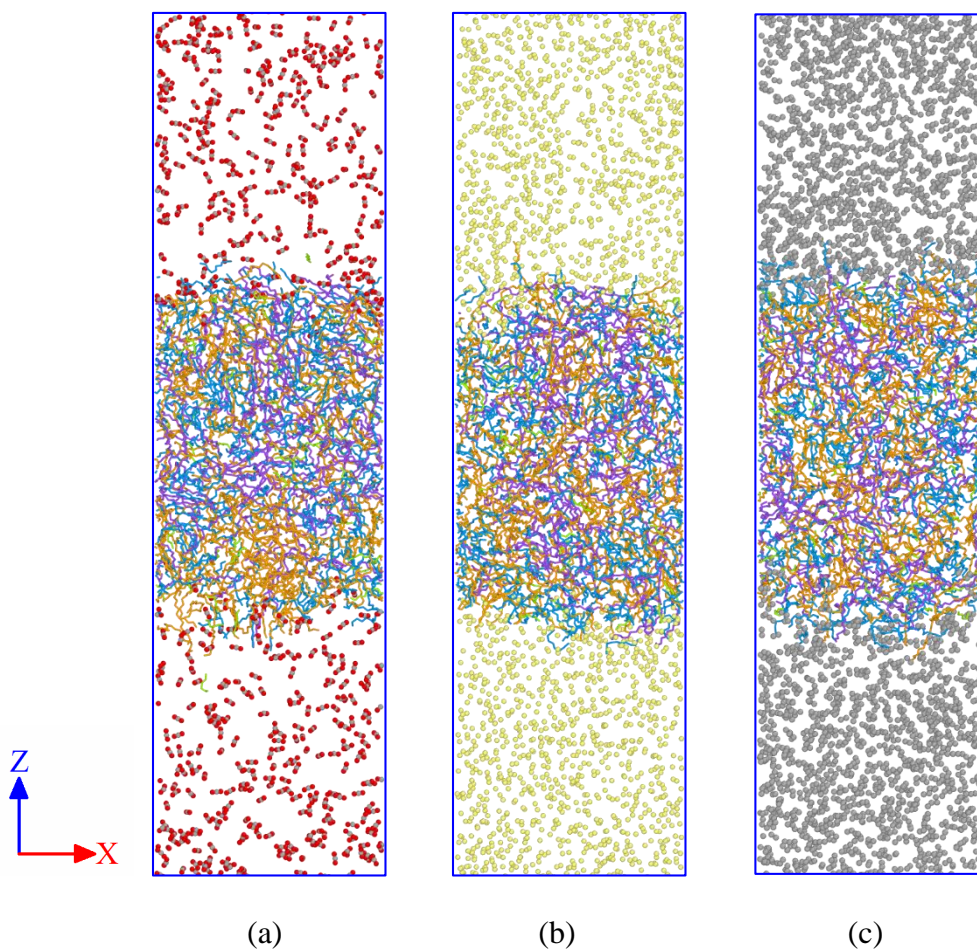
Figure 5-3 Simulation snapshots of injected gas-crude oil systems. (a) CO_2−crude oil, (b)

CH_4−crude oil, (c) C_2H_6−crude oil.

In order to mimic the oil reservoir condition, a temperature of 383 K was set in the simulations. The systems were first equilibrated in a 10 ns NVT simulation, and a production run of 30 ns was used to average the system properties. The Nosé−Hoover thermostat (Hoover et al., 1982; Nosé, 1984) with a relaxation time of 200 fs was applied to control the temperature. For the systems containing CO_2, the long-range electrostatic interactions were calculated using the particle−particle particle−mesh (PPPM) method (Hockney and Eastwood, 1989) with an accuracy of 10^{-5}. The cutoff radius was set to 20 Å, and the time step was set to 2 fs.

All MD simulations were performed using the LAMMPS package (Plimpton, 1995). The snapshots were rendered by the OVITO software (Stukowski, 2010).

5.3 Results and Discussion

5.3.1 Constituent density profiles

FiguresFigure 5-4,Figure 5-5, andFigure 5-6 show the density (ρ) profiles along the direction perpendicular to the interface (z-axis) for the interfacial systems containing CO_2, CH_4, and C_2H_6, respectively. Solid lines and dashed lines represent crude oil and injected gases, separately. The lines with different colors represent results at different pressures.

In all simulation conditions, the pressure of the system was lower than the MMP. When the two phases contact with each other, a small amount of crude oil and injected gases will leave their own phase and become solvated by the molecules of the other phase. The clear interfaces are formed as the system reaches equilibrium. In each simulation system, two interfaces can be found from the density profile. The interfacial width becomes wider as more gas dissolve in the crude oil. When the pressure reaches the MMP, the interfaces disappear, and the two phases become miscible, which can further improve the oil recovery efficiency.

From the simulation results, for the injected gas−crude oil system, the oil density decreases with the increase of pressure. When the injected gases contact the crude oil, the dissolution of the injected gases occurs, thereby causing swelling and density reduction. As the injection pressure increases, more gas molecules dissolve into the crude oil, causing larger oil swelling and density reduction.

As shown in the density profiles, CO_2 and C_2H_6 accumulate at the oil-gas interfaces, while CH_4 does not. Moreover, C_2H_6 is more soluble in the crude oil than CO_2 and CH_4, because C_2H_6

47

has the strongest attractive interaction with the crude oil, and it is more oleophilic than the other two gases.
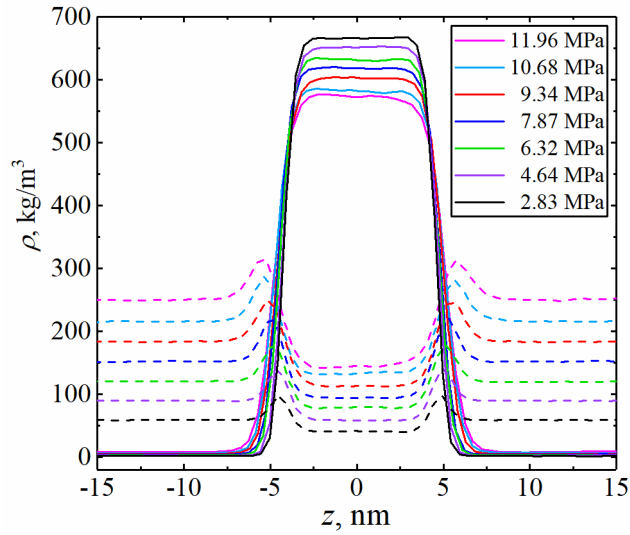
Figure 5-4 Density profile of the CO_2−crude oil system at 383 K and various pressures.
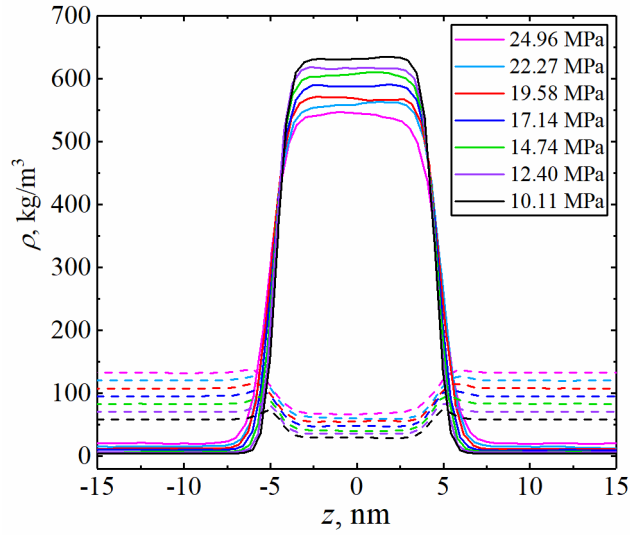
Figure 5-5 Density profile of the CH_4−crude oil system at 383 K and various pressures.
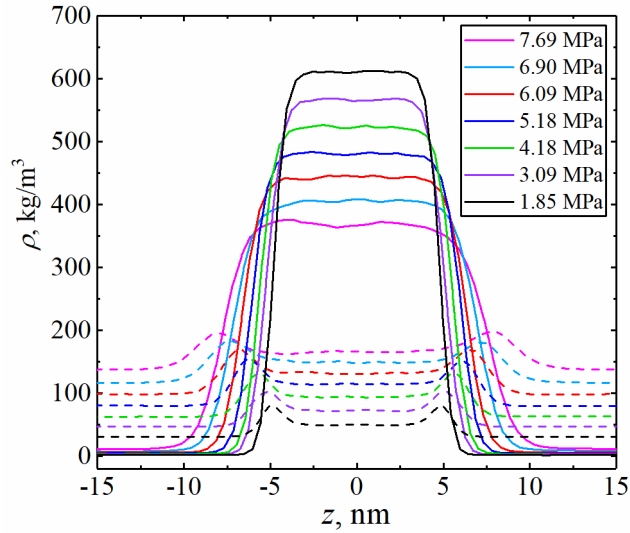
Figure 5-6 Density profile of the C_2H_6−crude oil system at 383 K and various pressures.

5.3.2 Gas solubility and oil swelling

The solubility process plays an important role in the oil swelling as well as the oil recovery. From the density profile, the gas solubility was calculated by the amount of gas dissolved in the crude oil with the unit of g/100g. The swelling factor is defined as the volume of the saturated gas−oil mixture divided by the volume of the oil alone (Orr et al., 1982). While, in this study, the swelling factors were calculated by the density ratio of the pure oil to the gas saturated oil.

Figures Figure 5-7, Figure 5-8,Figure 5-9 show the solubility of the gases in the crude oil and the swelling factors as a function of pressure at 383 K for CO_2, methane, and ethane, respectively. Both the gas solubility and the swelling factor increase with increasing pressure. C_2H_6 has a higher solubility in the crude oil and can induce a more pronounced oil swelling than CO_2 and CH_4. The oil swelling can increase oil saturation as well as the reservoir pressure, and the trapped oil will be forced out of the pore spaces. Therefore, for C_2H_6 injection, more incremental oil production can be obtained.
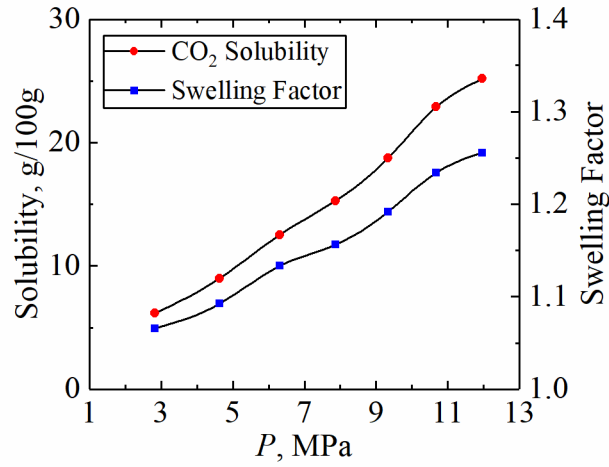
Figure 5-7 CO_2 solubility & swelling factor as a function of pressure at 383 K.
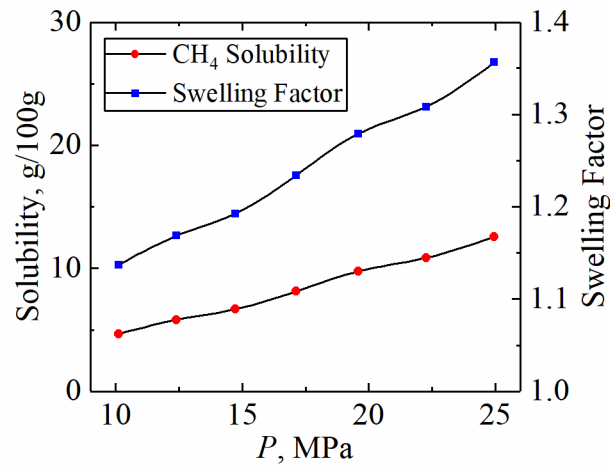
Figure 5-8 CH_4 solubility & swelling factor as a function of pressure at 383 K.
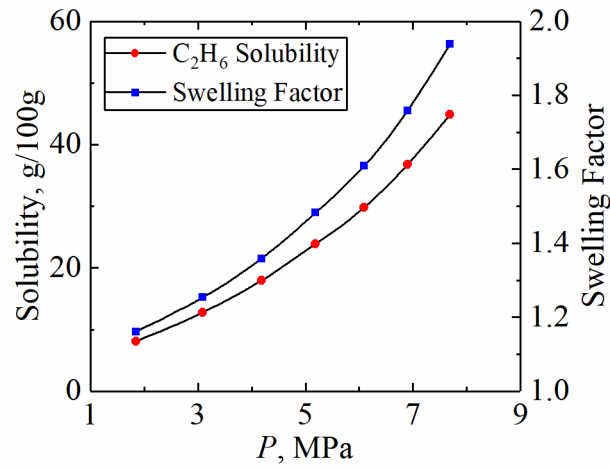
Figure 5-9 C_2H_6 solubility & swelling factor as a function of pressure at 383 K.

From the simulation results, the swelling factor presents a good linear relationship with the gas solubility (Figure 5-10), which is in good agreement with the research results in the literature (Chung et al., 1988; Welker and Dunlop, 1963). The greater solubility of gas results in a higher swelling factor. The swelling of crude oil due to the dissolution of the injected gas can be predicted from the gas solubility.

At a given gas solubility, CH_4 can lead to a more significant oil swelling than C_2H_6 and CO_2. However, the injection pressure is much higher for CH_4 to attain the same solubility as CO_2 and C_2H_6. Therefore, compared with CO_2 and C_2H_6, the operation of CH_4 injection is more difficult in terms of the injection pressure.
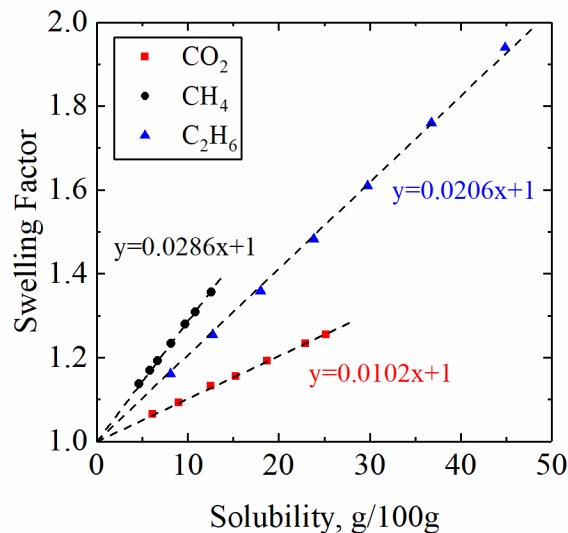
Figure 5-10 Swelling factors as a function of gas solubility at 383 K.

5.3.3 Diffusion coefficient of crude oil

The dissolution of the injected gas can also improve the flowability of crude oil. In order to evaluate the flowability, the diffusion coefficient of the crude oil was calculated based on the mean square displacement (MSD) using Einstein relation (Allen and Tildesley, 1989).

$$D = \lim_{t \to \infty} \frac{\langle [r(t) - r(0)]^2 \rangle}{6t} \tag{5.4}$$

where D is the diffusion coefficient, $r(t) - r(0)$ is the center of mass displacement of the molecules, the angle brackets indicate the ensemble average, and t is the simulation time.

Under different pressures, the diffusion coefficients of gas saturated crude oil were calculated, as shown in Figure 5-11. With gas molecules dissolve in the crude oil, the interaction between hydrocarbon molecules weakens. Therefore, for the injected gas–crude oil system, the diffusion coefficient of the oil phase increases with the increase of pressure. Compared with CO_2 and CH_4, C_2H_6 can induce a higher diffusion coefficient of crude oil, and thus it is more effective in mobilizing the crude oil.
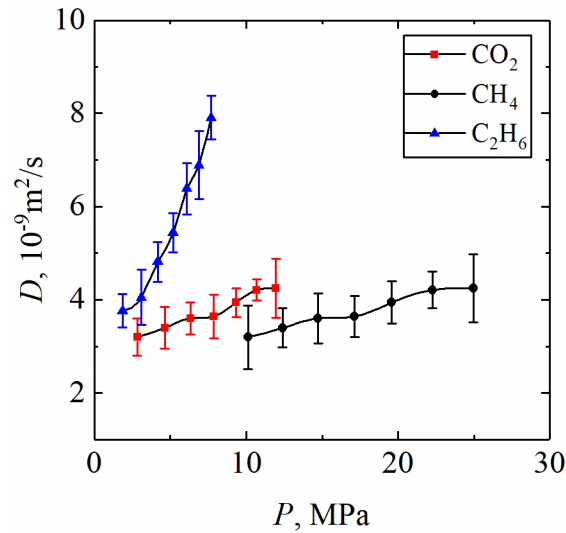
Figure 5-11 Diffusion coefficient of the gas saturated crude oil as a function of pressure.

5.3.4 Interfacial tension (IFT) and minimum miscibility pressure (MMP)

The MMP is another crucial parameter for a successful gas injection project. When the operation pressure is higher than the MMP, the injected gas and crude oil can reach a miscible condition that the two phases can mix at any ratio. Compared with immiscible gas injection, the

52

miscible gas injection can further improve oil recovery (Martin, 1983; Martin and Taber, 1992; Yu et al., 2015).

The vanishing interfacial tension (VIT) method (Rao, 1997) was used to determine the MMP values. The IFT (γ) was calculated from the expression of pressure tensor (Zhang et al., 1995) as follows,

$$\gamma = \frac{1}{2}\left\langle L_z(p_{zz} - \frac{p_{xx} + p_{yy}}{2})\right\rangle \tag{5.5}$$

where L_z is the box length in the z-direction, P_{xx}, P_{yy}, and P_{zz} are the diagonal elements of the pressure tensor, and the angled brackets indicate the ensemble average.

The IFT values of injected gas−Bakken oil systems were calculated at 383 K and various pressures. Figures Figure 5-12Figure 5-13,Figure 5-14show the results for CO_2, CH_4, and C_2H_6, respectively. The IFT decreases with increasing pressure and presents a linear relationship. The trend was extrapolated to zero IFT, at which the pressure was determined as the MMP.
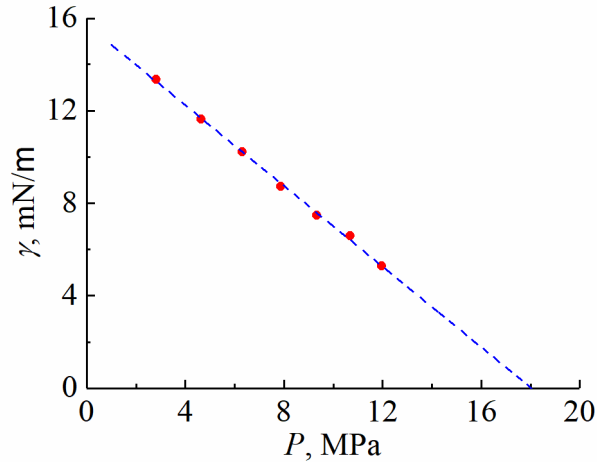
Figure 5-12 IFT of CO_2−Bakken oil system as a function of pressure at 383 K
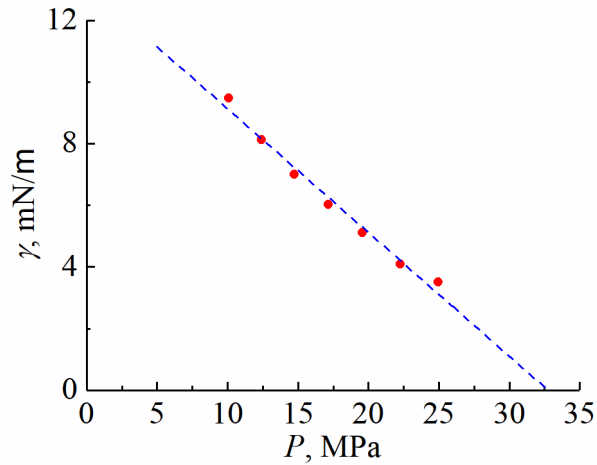
Figure 5-13 IFT of CH_4−Bakken oil system as a function of pressure at 383 K
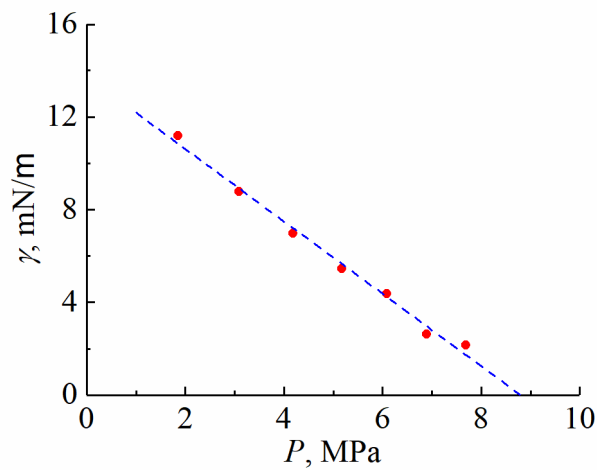
Figure 5-14 IFT of C_2H_6−Bakken oil system as a function of pressure at 383 K

The MMPs of injected gas−crude oil systems at 383 K predicted by the MD simulation are listed in table 1. The results agree well with the experimental data and simulation results in the literature. The relative errors between the simulation results and the experimental data are around 5%.

Table 5-1 MMPs of injected gas-Bakken oil systems at 383 K from the MD simulation

Injected gas	MMPs (MPa)		
	This study	Experiment[a]	Reference simulation[b]
CO_2	18.04	17.43	16.71
CH_4	32.74	31.14	−
C_2H_6	8.80	9.27	−

[a] experimental data of MMP from Hawthorne et al. (Hawthorne et al., 2016).

[b] simulation result of MMP from Peng et al. (Peng et al., 2018).

For the Bakken crude oil at its reservoir temperature of 383 K, CH_4 approximately doubles the MMP compared to CO_2, while C_2H_6 reduces the MMP by about one-half. MMP is the pressure necessary to ensure the miscibility of the injected gases and in-situ oil. The MMP results show that lower injection pressure is needed for C_2H_6 EOR to achieve a miscible oil recovery process. Under miscible conditions, the interfacial tension becomes zero and capillary pressure disappears, which resulting in the injection gas and crude oil form a single-phase and flow together more easily through the porous media (Orr et al., 1982; Yu et al., 2015). Compared with immiscible gas injection, the injected gas can extract more hydrocarbons from the oil phase during the miscible gas injection. Therefore, a much lower MMP allows C_2H_6 EOR to recover more crude oil than CH_4 or CO_2 EOR at the operation conditions.

Considering the oil swelling, MMP, and oil diffusion coefficient, C_2H_6 is more effective in mobilizing crude oil than CO_2 and CH_4. Meanwhile, the re-injection of C_2H_6 in the Bakken Formation can be a potential EOR technology because of the excess C_2H_6 in the Bakken oil play.

5.4 Conclusion

In this study, the molecular dynamics simulation was performed to investigate the interfacial interactions between the Bakken crude oil and the injected gases. The gas solubility, the volume swelling factor, the oil diffusion coefficient, and the minimum miscibility pressure (MMP) have been studied to evaluate the EOR potentials of different gases (CO_2, CH_4, and C_2H_6). The simulation results show that each of the three gases holds great potential in improving oil recovery.

When the injected gases come in contact with crude oil, the dissolution of the injected gases occurs, thereby causing oil swelling. Both the gas solubility and the swelling factor increase with increasing pressure. The linear relationship between the swelling factor and the gas solubility can be used to predict the oil swelling. Compared with CO_2 and CH_4, C_2H_6 has stronger attractive interaction with crude oil, and thus it is more soluble in crude oil and induces a more pronounced oil swelling. Meanwhile, C_2H_6 leads to a stronger oil diffusivity, and thus it is more effective in mobilizing crude oil. Furthermore, C_2H_6 is more favorable for the Bakken Formation since C_2H_6 is sufficient in the Bakken oil play, and there is no need for high injection pressure.

The molecular-level insight into the interaction between the hydrocarbons and injected fluid can be obtained from the molecular dynamics (MD) simulation. The MD simulation is useful in predicting the experimental results and guiding the gas injection EOR in the Bakken Formation.

CHAPTER 6

EFFECT OF THE INJECTED GASES AND NANO-CONFINEMENT ON THE OIL DETACHMENT FROM MINERAL SURFACES

6.1 Introduction

In Chapter 5, only the interactions between the injected gases and crude oil are considered to compare the EOR potentials of different gases. However, tight rocks are dominated by nanoscale and microscale pore throats (Nelson, 2009; Zhang et al., 2020), and fluids are significantly affected by the strong rock-fluid interactions (Alharthy et al., 2013). Besides fluid-fluid interactions, the EOR processes also involve the adsorption and transport of injected gases and hydrocarbons in nanopores. To further evaluate the efficiency of different gases in improving oil recovery, we should take the mineral surfaces and the nanoconfinement into consideration.

The XRD mineralogy analysis of the core samples shows that the Middle Bakken rock mainly consists of different inorganic minerals of various proportions (Figure 2-4). The N_2 adsorption results indicate the pores of the Middle Bakken rock are slit-shaped pores. Three main minerals (quartz, calcite, and illite) in the Bakken Formation were modeled.

Equilibrium MD simulations were conducted to study the adsorption behavior of oil molecules confined in slit-shaped mineral nanopores. Then, the oil detachment from a calcite surface in the process of gas injection was also investigated using MD simulations. The effects of CO_2 and C_2H_6 on the oil detachment were compared. To further investigate the ability of the two gases in terms of oil extraction as well as the effect of nanoconfinement, oil extraction from dead-end nanochannels was simulated. Considering the conditions with or without nanoconfinement, different oil displacement mechanisms were demonstrated.

6.2 Models and Methodology

6.2.1 Octane confined in slit-shaped nanopores

The quartz (100) surface, calcite (104) surface, and illite (100) surface were cleaved from the bulk crystal structures. In the illite unit cell, one octahedral Al^{3+} was substituted by Mg^{2+} and one tetrahedral substitution of Si^{4+} by Al^{3+}. The CLAYFF force field (Cygan et al., 2004) was implemented to simulate quartz and illite, while the potential model developed by Xiao et al. (2011) was adopted to describe the calcite substrate. The slit-shaped mineral pores with a width of ~6 nm were built. Octane (C_8H_{18}) molecules were modeled according to the NERD force field (Nath et al., 1998) and added in the slits. The simulated systems of C_8H_{18} confined in slit-shaped pores are shown in Figure 6-1. The systems were simulated under the conditions of 383K and 35 MPa. The pressure of the fluid was controlled using the method proposed by Falk et al. (2012). The temperature was controlled using the Nosé-Hoover thermostat.
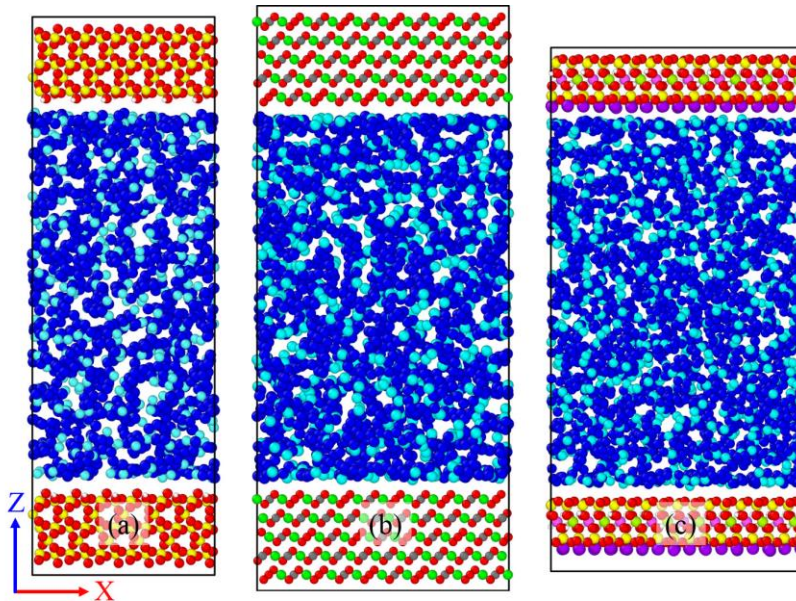
Figure 6-1 Simulated systems of octane confined in slit-shaped pores: (a) quartz, (b) calcite, (c) illite. Red, yellow, white, gray, green, pink, light green, purple, blue, cyan spheres represent O, Si, H, C, Ca, Al, Mg, K, CH_2 group, and CH_3 group, respectively.

6.2.2 Oil detachment from surface and oil extraction under nanoconfinement

To further compare the EOR potential of CO_2 and C_2H_6, the oil detachment from calcite surfaces and oil extraction from dead-end calcite nanochannels were investigated. With the same oil and CO_2 models as Chapter 5, the initial configurations of oil/CO_2/calcite systems were built as shown in Figure 6-2. An external force was applied on the topmost slab to keep the pressure of the fluid phase being maintained at a specified pressure. The temperature of the systems was maintained at 383 K. The simulations of oil extraction by C_2H_6 were also conducted following the same procedure. All systems were simulated for 10 ns in the NVT ensemble.
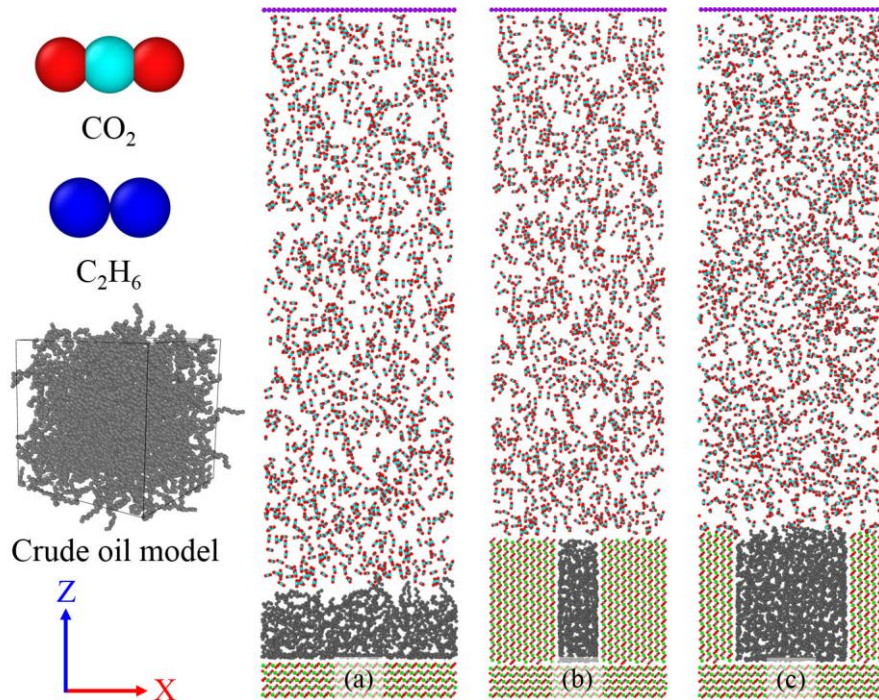
Figure 6-2 Snapshots of models for simulating oil extraction by CO_2: (a) calcite surface, (b) 2.19

nm calcite nanochannel, (c) 5.22 nm calcite nanochannel.

6.3 Results and Discussion

6.3.1 Adsorption characteristics of C_8H_{18} in slit pores

The mass density profiles of C_8H_{18} in different slit-pores are shown in Figure 6-3. The mass density profiles are symmetric with respect to the central plane ($z = 0$) of the two mineral surfaces. Dense C_8H_{18} layers exist in the near-wall region. From the spacing between two successive troughs, we determined the thickness of each monolayer (~0.45 nm). The density tends toward a constant (the bulk density at the same pressure and temperature) when it is farther away from the solid surface. The peak values in the density profiles indicate a higher oil adsorption on calcite surfaces than the other two minerals.
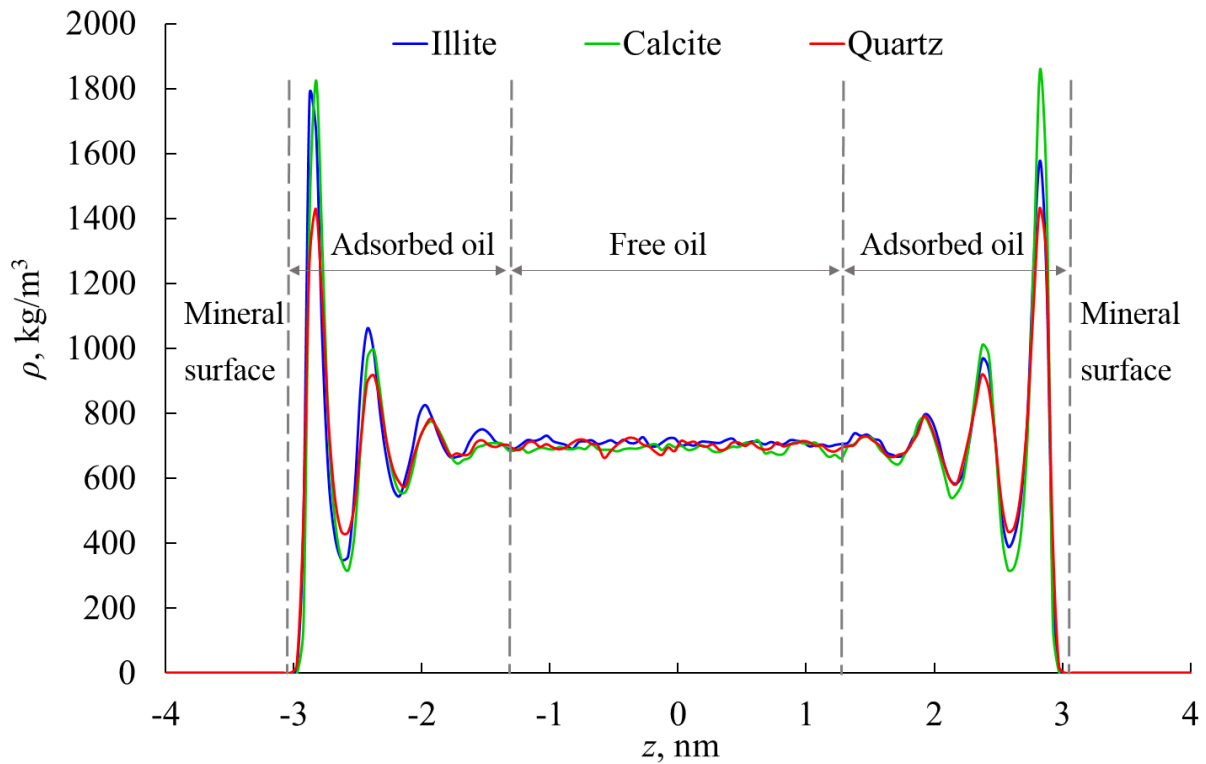
Figure 6-3 Density profiles of octane in mineral slit-pores.

60

6.3.2 Oil detachment from calcite surface

At the reservoir temperature of 383 K and three different pressures (10 MPa, 20 MPa, and 35MPa), the oil detachment abilities by CO_2 and C_2H_6 were investigated. The final configurations are shown in Figure 6-4 and Figure 6-5.

In CO_2 cases, at 10 MPa, a small fraction of oil molecules diffuses into the bulk CO_2, and most oil molecules aggregate together and cannot be detached. As shown in Figure 6-4(a), CO_2 molecules tend to adsorb on the calcite surface due to the strong interactions between O atoms of the CO_2 and calcium (Ca) sites. A dense CO_2 layer is formed on the calcite surface, but it does not contribute to the oil detachment. At 20 MPa, more oil molecules dissolve into the bulk CO_2, but the majority of oil molecules form several smaller aggregates. At 35 MPa, all oil molecules dissolve into the bulk CO_2.
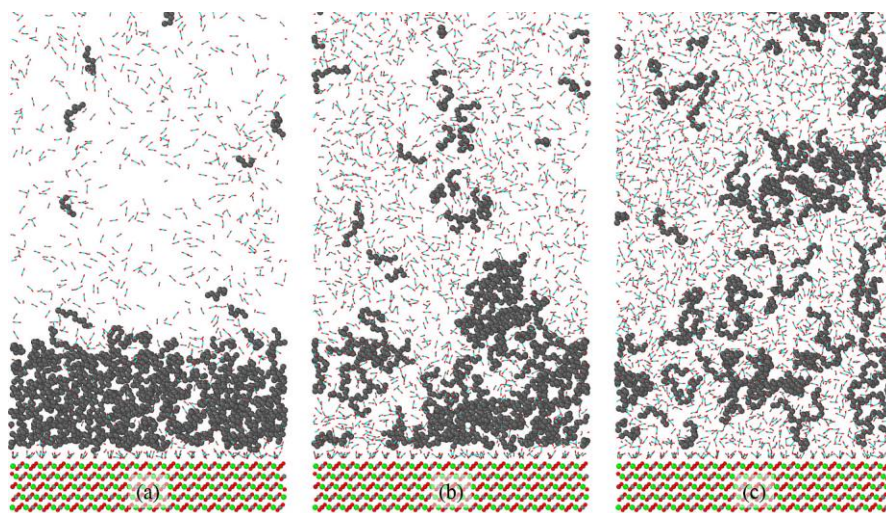
Figure 6-4 Oil detachment from calcite surfaces by CO_2: (a) 10 MPa, (b) 20 MPa, (c) 35 MPa

In C_2H_6 cases, at 10 MPa, a small fraction of oil molecules diffuses into the bulk C_2H_6, and most oil molecules aggregate together and cannot be detached. At 20 MPa, most oil molecules dissolve into the bulk C_2H_6 except the dense oil layer. At 35 MPa, no big differences are found

compared to the final configuration at 20 MPa. The oil molecules dissolve into the bulk C_2H_6 more uniformly.
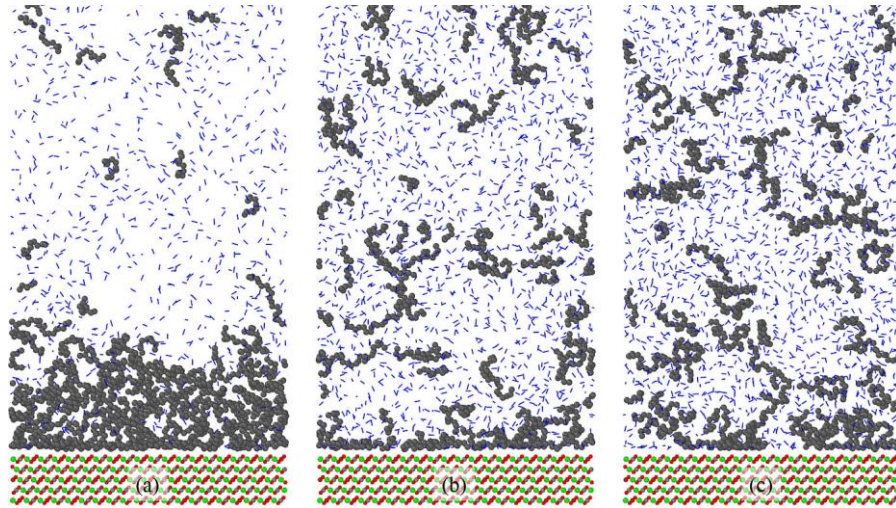
Figure 6-5 Oil detachment from calcite surfaces by C_2H_6: (a) 10 MPa, (b) 20 MPa, (c) 35 MPa

The density profiles of oil molecules, CO_2, and C_2H_6, were calculated to give a detailed distribution of the molecules (Figure 6-6).
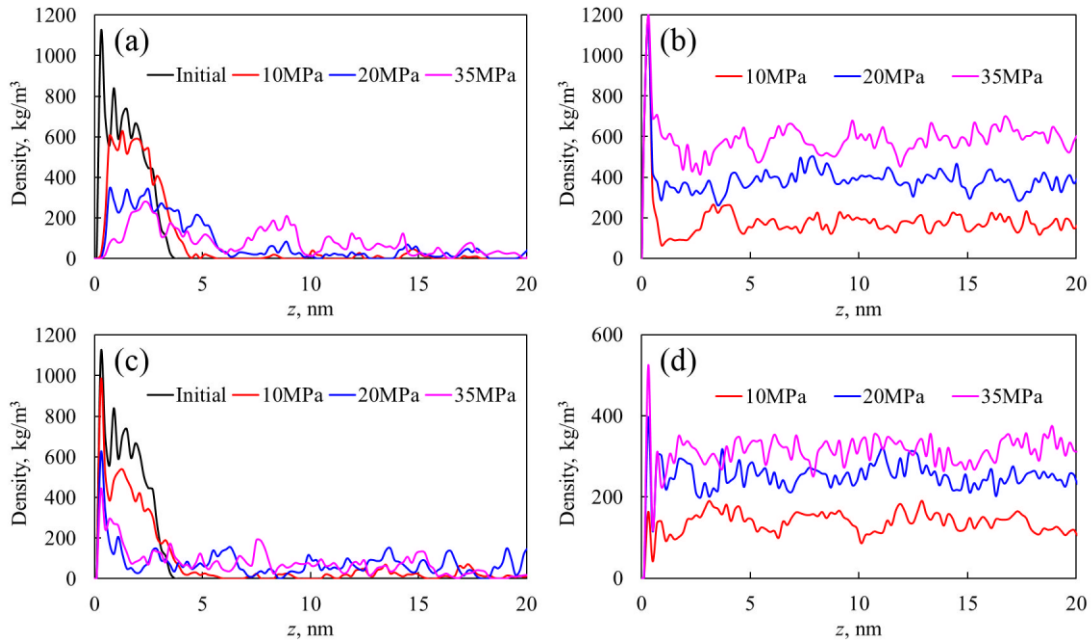
Figure 6-6 Density profiles for different molecules along z-axis: (a) oil molecules in the CO_2 cases, (b) CO_2, (c) oil molecules in the C_2H_6 cases, (d) C_2H_6.

The broad peaks in Figure 6-6(a) indicate that the detached oil molecules by CO_2 still attach to one another. In each curve of Figure 6-6(b), a distinct peak of CO_2 is localized near the calcite surface due to the competitive adsorption of CO_2 on the calcite surfaces. The peak density value remains unchanged with increasing pressure.

In Figure 6-6(c), the typical adsorption peaks suggest that some oil molecules still adsorb on the calcite surface. Except for the adsorption peaks, the even distribution feature of the profiles indicates that the oil molecules dissolve into the bulk C_2H_6 uniformly. From the peak density values in Figure 6-6(c) and Figure 6-6(d), the adsorption loading of oil on the calcite surface gradually decreases with increasing pressure, while the adsorption loading of C_2H_6 gradually increases with the increasing pressure. This phenomenon is caused by the increasing mutual solubility of oil and C_2H_6.

The oil detachment from the calcite surface is mainly affected by the swelling effect and the mutual dissolution, which lead to the decrease of viscosity and improvement of mobility. C_2H_6 shows advantages in detaching oil from calcite surface, particularly at lower pressure, because it is more soluble in crude oil and more effective in swelling crude oil. CO_2 molecules adsorb on calcite surface more preferentially than C_2H_6, but the competitive adsorption does not contribute significantly to the oil detachment.

6.3.3 Oil extraction from dead-end calcite nanochannel

Under nanoconfinement, interactions between fluid molecules and the solid surface significantly affect the diffusion behavior of the molecules. The final configurations of oil

extraction from dead-end calcite nanochannels at 383K and 10 MPa are shown in Figure 6-7. The percentages are the extraction efficiency.

As illustrated in Figure 6-3, only adsorbed oil exists in the 2.19 nm nanochannel. CO_2 molecules have a strong preference for adsorbing on the nanochannel surfaces and extract most oil from the nanochannel. In the 5.22 nm nanochannel, the adsorbed oil is detached by CO_2 while the majority of oil molecules still attach to one another and cannot be extracted from the nanochannel.

C_2H_6 mainly dissolve into the bulk oil and swells the oil phase. The swelling effect and mutual dissolution result in a small portion of oil extracted from the nanochannels. The interactions between oil molecules and the surface-oil interactions prevent the oil molecules from moving out of the nanochannel. Most oil molecules are still trapped in the nanochannels.
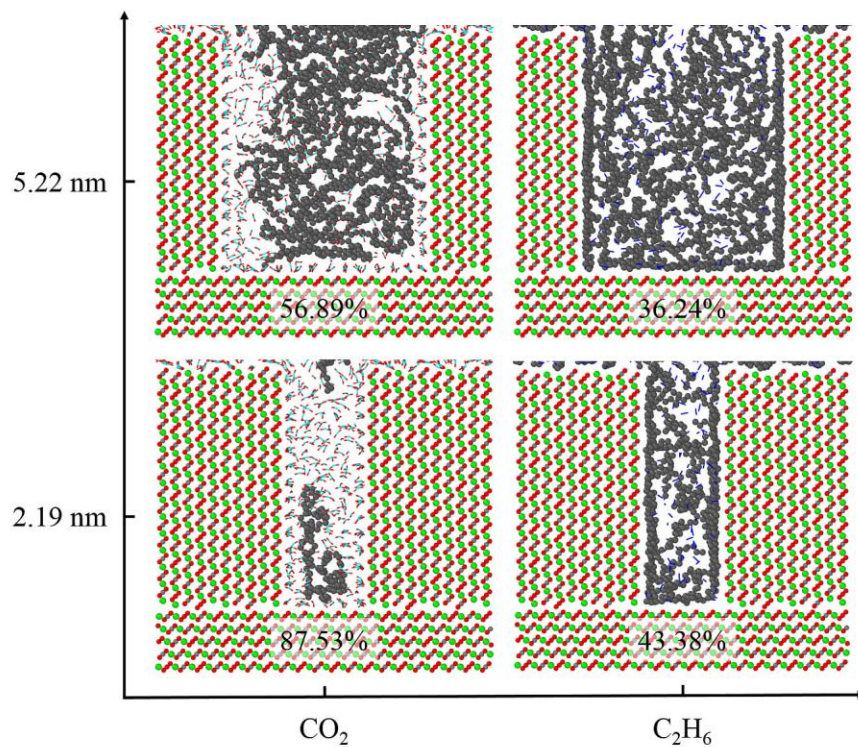
Figure 6-7 Oil extraction from dead-end calcite nanochannels at 383K and 10 MPa.

At higher system pressure, 35 MPa, the effect of swelling extraction and mutual dissolution becomes more pronounced. The oil extraction efficiencies are improved as shown in Figure 6-8. At the pressure of 10 MPa, CO_2 already extracts the majority of oil from the 2.19 nm nanochannel, so no significant improvement in the oil extraction efficiency is found in this case. Similar to the cases at 10 MPa, CO_2 has a larger oil extraction efficiency than C_2H_6. Simulation results indicate that competitive adsorption plays a more important role than swelling extraction and mutual dissolution in extracting oil under nanoconfinement.
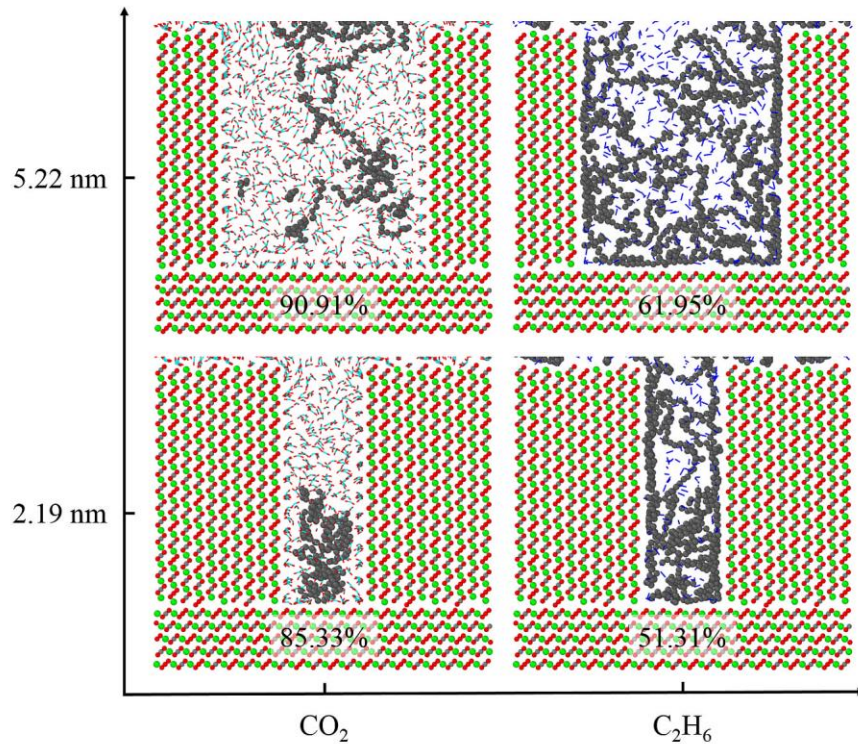
Figure 6-8 Oil extraction from dead-end calcite nanochannels at 383K and 35 MPa.

6.4 Conclusions

To comprehensively characterize the gas injection EOR, the complicated interactions between fluid and mineral surfaces were investigated. The oil extraction mechanisms from dead-end nanochannels with the injection of CO_2 and C_2H_6 was assessed.

The density profile of fluids in a mineral nanochannel is highly dependent on the mineral–fluid interaction. However, when the width of the nanochannel is greater than a threshold value, the fluid, which is in the center of the nanochannel, is slightly influenced by solid substrates and has similar properties as the bulk fluid.

Without nanoconfinement, the swelling extraction and mutual dissolution are the dominant factors affecting the oil detachment. C_2H_6 is more efficient than CO_2 in detaching adsorbed oil from calcite surfaces. Considering the nanoconfinement, competitive adsorption plays a more important role. CO_2 is more efficient than C_2H_6 in extracting oil from dead-end calcite nanochannels.

CHAPTER 7

MOLECULAR SIMULATION STUDY OF INTERFACIAL TENSION REDUCTION AND OIL DETACHMENT BY SURFACE-MODIFIED SILICA NANOPARTICLES

7.1 Introduction

In the tight formations, residual oil is trapped in the narrow throats due to high capillary pressure, which is influenced by rock wettability and oil/water interfacial tension (IFT) (Hendraningrat and Torsæter, 2014). For the oil industry, chemical injection is another effective enhanced oil recovery (EOR) technique.

Surfactant flooding is one commonly used technology in the chemical EOR process. Surfactants can mobilize residual oil by lowering the oil/water interfacial tension and/or by altering the rock wettability from oil-wet to water-wet (Kamal et al., 2017b). Under mild reservoir conditions (low temperature, low salinity), most surfactants perform well in improving oil recovery. However, under harsh reservoir conditions (high temperature, high salinity), the stability and effectiveness of surfactants can be a challenging task (Kamal et al., 2017b; Negin et al., 2017). Moreover, the high cost of chemicals and the surfactant loss due to the high adsorption on rock surfaces also limit the application of surfactant flooding (Gogoi, 2011). Therefore, less expensive and more efficient EOR methods are greatly needed.

Recently, nanotechnology has been employed to solve different problems arising during surfactant flooding. By adding different nanoparticles (NPs) in the base fluids (such as water, brine, ethanol, etc.), investigators have developed various types of nanofluids to improve oil recovery (Kamal et al., 2017a; Nazari Moghaddam et al., 2015). Studies have shown that NPs can improve oil recovery either alone or in combination with surfactants (Hendraningrat et al., 2013; Zargartalebi et al., 2015). The EOR mechanisms of nanofluids have already been reported by many

researchers, which mainly include disjoining pressure, IFT reduction, wettability alteration, preventing asphaltene precipitation, and viscosity increase of injection fluids (Sun et al., 2017). The presence of NPs can also decrease the adsorption of surfactant molecules on rock surfaces (Chen et al., 2018; Zargartalebi et al., 2015). Since silica (SiO_2) is cheap and environmentally friendly compared to other nanomaterials, SiO_2 NPs are the most commonly used nanomaterials in nanofluid flooding. Besides, chemical behaviors of SiO_2 NPs can be easily controlled by surface modification with different functional groups (Bagwe et al., 2006; Jang et al., 2018; Qiao et al., 2016; Worthen et al., 2016).

Understanding the behavior of NPs at the nanoscale is important to the development of nanofluids for EOR applications. In recent years, molecular simulations have been employed in the oil industries to study different EOR methods (Le et al., 2015; Li et al., 2019b; Tang et al., 2019; Yan et al., 2017a). Atomistic molecular dynamics simulations (Fan et al., 2011; Liang et al., 2019), dissipative particle dynamics simulations (Luu et al., 2013a; Vu and Papavassiliou, 2019), and coarse-grained molecular dynamics simulations (Katiyar and Singh, 2017; Li et al., 2019a) have been performed to study the properties of NPs and the effect of NPs on the IFT and oil detachment. Molecular simulations can provide a molecular-level insight into the interactions between components, which is generally difficult to obtain from experiments.

While substantial studies have focused on using NPs to improve oil recovery, whether NPs adsorbed at an interface can reduce the interfacial tension is still controversial. In addition, seldom molecular models have been built to investigate the effect of NPs on oil transportation in nanopores. In this study, molecular simulations were performed to study the influence of various NPs on the oil/water interfacial tension and the oil detachment and displacement in the quartz nanochannels.

Both water-wet and oil-wet surfaces were considered. The EOR mechanisms of the surface-modified NPs were discussed.

7.2 Models and Methodology

7.2.1 Molecular models and force field

All molecular models used in the simulations are illustrated in Figure 7-1. In this work, quartz was chosen as the mineral to study because it is a major rock-forming mineral. Hydroxylated quartz was used to represent the water-wet rock. To mimic the oil-wet rock, methyl groups were grafted on the quartz surfaces (Liang et al., 2019). Octane (C_8H_{18}) was selected to represent the oil phase in simulating the oil/water interfaces, while alkane mixtures were used in the study of nanofluid flooding. The spherical SiO_2 NP was carved out from the amorphous SiO_2 (Lorenz et al., 2005). Typically, the size of NPs ranges from a few nanometers to 100 nm in diameter. However, for the economy of computational resources, all the NPs simulated in this work are 1.5 nm in diameter. Surface-modified SiO_2 NPs were modeled through modifying SiO_2 NP with functional groups. The alkyl carboxylate ion, $-(CH_2)_4COO^-$, and various alkyl chains ($-(CH_2)_nCH_3$) were selected as the hydrophilic and hydrophobic functional groups, respectively. Three configurations of functional groups on SiO_2 surfaces are shown in Figure 7-2.

69
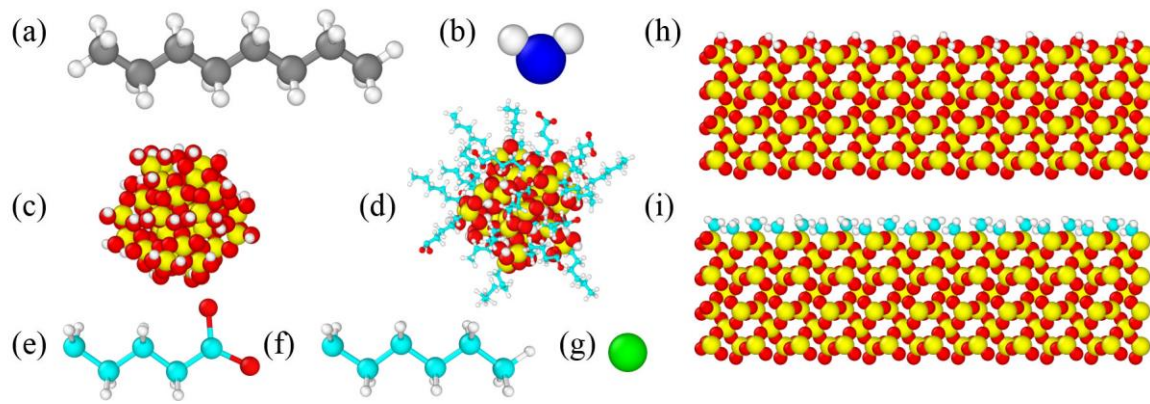
Figure 7-1 Molecular models used in the simulations: (a) octane; (b) water; (c) SiO_2 NP; (d) surface-modified SiO_2 NP; (e) alkyl carboxylate ion; (f) alkyl chain; (g) Na^+; (h) hydroxylated quartz surface; (i) methylated quartz surface. Gray, white, blue, red, yellow, cyan, and green spheres represent carbon, hydrogen, oxygen, oxygen, silicon, carbon, and sodium, respectively.
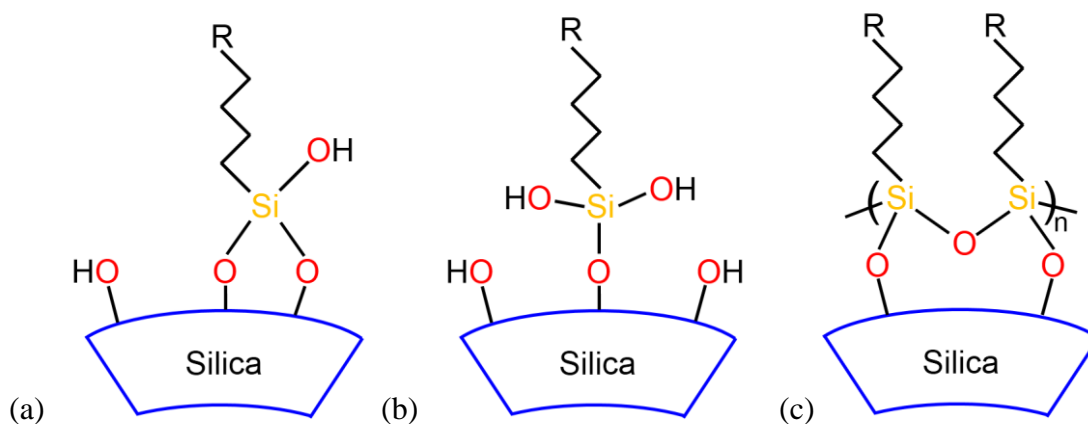
Figure 7-2 Three configurations of functional groups on silica surfaces. R represents $-COO^-$ or $-(CH_2)_nCH_3$ (Adapted from Worthen et al., 2016).

By varying the ratio and distribution of the functional groups on the NP surface, different surface-modified NPs were built, as shown in Table 7-1. Both homogeneous nanoparticles (HNPs) and Janus nanoparticles (JNPs) were considered in the study. HNPs were randomly covered by carboxylates and/or alkyl chains, while carboxylates and alkyl chains were grafted on opposite sides of the JNPs.

Table 7-1 Name and Surface Chemistry of the NPs in the Simulations

Name	surface group composition
HNP1	100% $-OH$
HNP2	100% $-(CH_2)_4COO^-$
HNP3	100% $-(CH_2)_5CH_3$

Name	surface group composition
HNP4	50% $-(CH_2)_4COO^-$ + 50% $-(CH_2)_3CH_3$
HNP5	50% $-(CH_2)_4COO^-$ + 50% $-(CH_2)_4CH_3$
HNP6	50% $-(CH_2)_4COO^-$ + 50% $-(CH_2)_5CH_3$
HNP7	50% $-(CH_2)_4COO^-$ + 50% $-(CH_2)_6CH_3$
HNP8	50% $-(CH_2)_4COO^-$ + 50% $-(CH_2)_7CH_3$
JNP1	70% $-(CH_2)_4COO^-$ + 30% $-(CH_2)_5CH_3$
JNP2	60% $-(CH_2)_4COO^-$ + 40% $-(CH_2)_5CH_3$
JNP3	50% $-(CH_2)_4COO^-$ + 50% $-(CH_2)_5CH_3$
JNP4	40% $-(CH_2)_4COO^-$ + 60% $-(CH_2)_5CH_3$
JNP5	30% $-(CH_2)_4COO^-$ + 70% $-(CH_2)_5CH_3$
JNP6	50% $-(CH_2)_4COO^-$ + 50% $-(CH_2)_3CH_3$
JNP7	50% $-(CH_2)_4COO^-$ + 50% $-(CH_2)_4CH_3$
JNP8	50% $-(CH_2)_4COO^-$ + 50% $-(CH_2)_6CH_3$
JNP9	50% $-(CH_2)_4COO^-$ + 50% $-(CH_2)_7CH_3$

In this study, the all-atom Optimized Potential for Liquid Simulation (OPLS-AA) force field (Jorgensen et al., 1996; Siu et al., 2012) was employed for simulating alkanes and the functional groups. Water molecules were represented with the SPC/E model (Berendsen et al., 1987). For the quartz surfaces and the NP cores, we used the model proposed by Lorenz et al. (Lorenz et al., 2005) that was developed based on the OPLS-AA force field. The non-bonded interactions between atoms were described by the pairwise additive Lennard-Jones (LJ) 12−6 potentials and the Coulombic interactions. Interactions were reduced by a factor of 0.5 for 1−4 neighbor pairs.

Unlike-atom interactions were calculated using the geometric combining rules. The cutoff radius was set to 12 Å, and the time step was set to 1 fs. The long-range electrostatic interactions were calculated using the particle-particle particle-mesh (PPPM) method (Hockney and Eastwood, 1989) with an accuracy of 10^{-5}. The Nosé-Hoover thermostat and barostat (Hoover et al., 1982; Nosé, 1984) was used to control the temperature and pressure. All MD simulations were performed using the Large-scale Atomic/Molecular Massively Parallel Simulator (LAMMPS) code (Plimpton, 1995). The snapshots were rendered by the Open Visualization Tool (OVITO) (Stukowski, 2010).

7.2.2 Oil/water interfaces

As shown in Figure 7-3 Initial configuration of water/C_8H_{18} interfaces in the presence of NPswith a slab of water in the center and two C_8H_{18} slabs at each side of the box in the x-direction, a periodic orthorhombic simulation box was constructed with two interfaces formed. Two NPs were distributed at each interface of C_8H_{18} and water. For the system that contains NPs functionalized with carboxylates, Na^+ ions were added to keep charge balance. The density profiles of the C_8H_{18}/water systems with various NPs were calculated to show the distribution of NPs in the vicinity of oil/water interfaces. The temperature of the systems was kept constant at 300 K, and the pressure was maintained at 1 atm. The IFTs of different systems were calculated to investigate the influence of NPs on the IFT of the oil/water system.
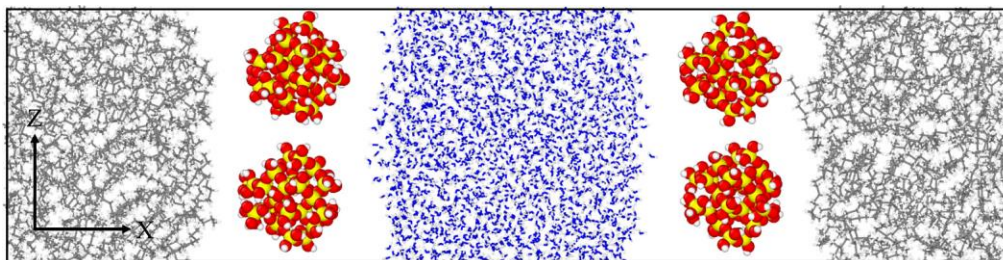
Figure 7-3 Initial configuration of water/C_8H_{18} interfaces in the presence of NPs

The IFTs were calculated from the expression of pressure tensors as follows (Zhang et al., 1995),

$$\gamma = \frac{1}{2}\left\langle L_x\left(P_{xx} - \frac{P_{yy} + P_{zz}}{2}\right)\right\rangle \tag{7.1}$$

where γ is the IFT, L_x is the box length in the x-direction, P_{xx}, P_{yy}, and P_{zz} are the components of the pressure tensor in x, y, and z directions, respectively. The angled brackets indicate the ensemble average.

The systems were first equilibrated for 2 ns, and then the production runs of 5 ns were performed. The IFTs were averaged over the last 2 ns of the production runs.

7.2.3 Alkanes/water/NPs transportation in confined nanochannels

The initial configuration for simulating the nanofluid flooding process is shown in Figure 7-4. The height of the nanochannel is ~6 nm and the length of the nanochannel is ~12 nm. Based on the components of a light crude oil sample (Hawthorne et al., 2016; Li et al., 2020), alkane mixtures were randomly distributed near the methylated quartz surfaces. In order to construct the nanofluid, four NPs were added to the water phase. The detachment and displacement processes of adsorbed oil in both water-wet and oil-wet nanochannels were investigated. The simulation temperature was kept constant at 353 K. The velocity of the left slab was set to 1.0 m/s (1.0×10^{-5} Å/fs) along the x-direction, and the external force was applied on the right slab to keep the pressure of the water phase being maintained at 35 MPa (Tang et al., 2019). The time-varying configurations of oil/water/NPs in the nanochannels were presented to show the dynamic displacing processes. The center of mass (COM) displacements of the oil droplets were calculated to show the oil detachment capacity of the NPs.
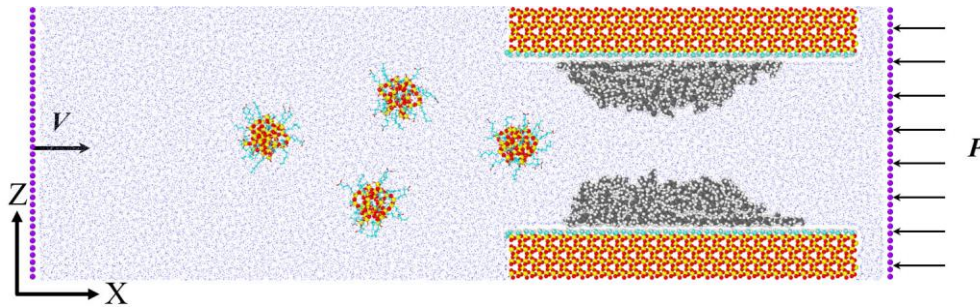
Figure 7-4 Initial configuration for simulating the nanofluid flooding process.

7.3 Results and Discussions

7.3.1 Location of NPs in the C_8H_{18}/water/NPs system

In Figure 7-5, we present the final simulation configurations of C_8H_{18}/water interfaces in the presence of different NPs. Unmodified SiO_2 NPs (i.e. HNP1) remain in the water phase but stay close to the oil/water interface. NPs modified with carboxylates (i.e. HNP2) shift from the oil/water interface to the bulk water due to increasing hydrophilicity. NPs modified with alkyl chains (i.e., HNP3) move into the oil phase, which shows the hydrophobic nature of the NPs. However, this type of NP cannot totally desorb from the interface to the oil phase. As shown in Fig.4(d), with carboxylates in the water phase and alkyl chains in the oil phase, the homogenous amphiphilic NPs and Janus NPs stay at the interfaces of oil and water.
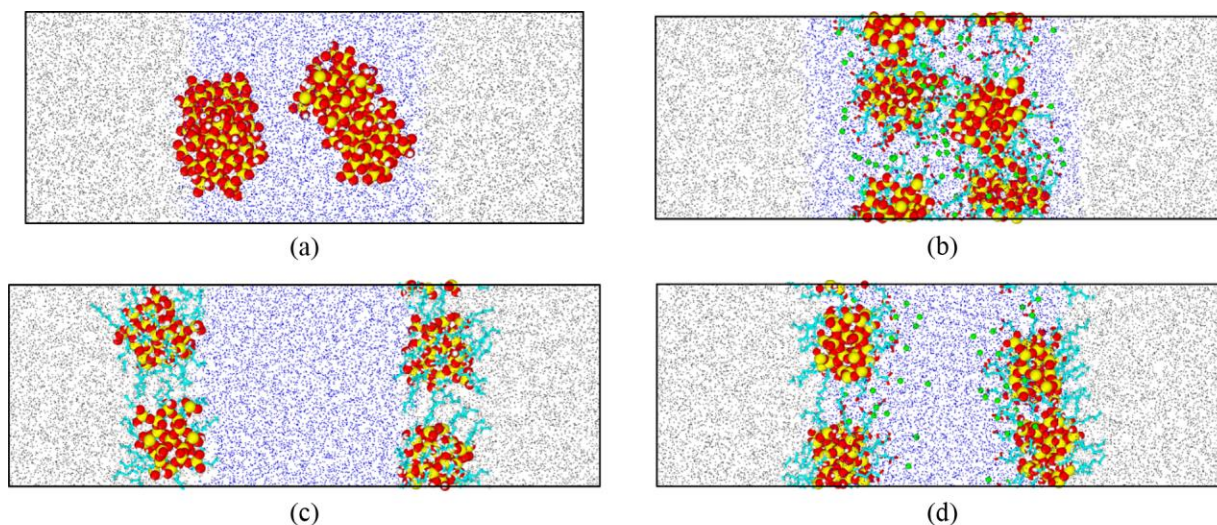
Figure 7-5 Final configurations of C_8H_{18}/water interfaces with different NPs: (a) HNP1; (b) HNP2; (c)HNP3;(4) JNP3.

7.3.2 Effect of NP type on oil/water IFT

Many experimental results about the effect of NPs on oil/water IFT have been reported. However, nanofluids are typically prepared with surfactants, ethanol, propanol, or other chemicals as the dispersant. These chemicals are able to reduce the IFT, so attributing the IFT reduction to NPs is not convincing. Herein, the effect of individual NPs on the IFT was investigated. The C_8H_{18}/water system without NPs was first simulated, and the IFT value (49.44±0.19 mN/m) in good agreement with the experimental data (51.20 mN/m and 50.97 mN/m) in the literature (Ndao et al., 2015; Zeppieri et al., 2001). Then the IFT values of C_8H_{18}/water systems with different NPs were calculated.

Unmodified NP (HNP1) does not tend to adsorb at the interface and can hardly affect the oil/water IFT. Surface-modified NPs with both hydrophilic and hydrophobic functional groups can reduce the IFT to some extent. For homogeneous NPs, as the carboxylates and the alkyl chains are randomly distributed on the NPs, the IFTs change irregularly. Herein, the effect of JNPs on the

75

oil/water IFT is mainly discussed. As shown in Figure 7-6, the IFT is affected by the ratio of hydrophilic and hydrophobic functional groups on the JNPs. With $-(CH_2)_4COO^-$ as the hydrophilic functional group, when the ratio of $-(CH_2)_5CH_3$ is 50% (i.e., JNP3), the lowest IFT is achieved.
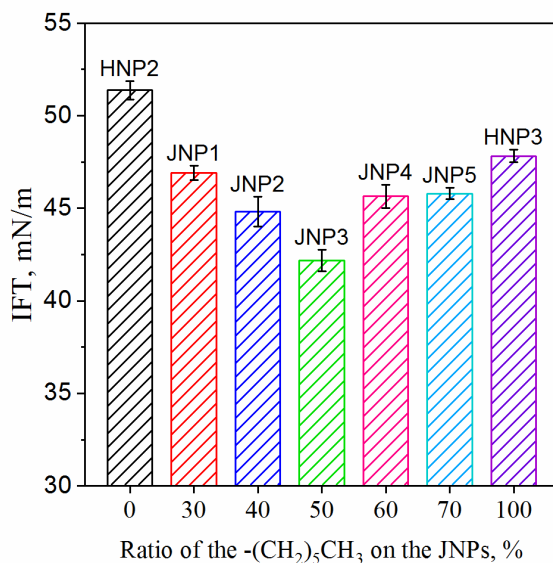
Figure 7-6 C_8H_{18}/water IFT as a function of the ratio of the $-(CH_2)_5CH_3$ on the JNPs.

The alkyl chain length of the hydrophobic functional groups can also affect the IFT. As shown in Figure 7-7, with 50% $-(CH_2)_4COO^-$ and 50% different alkyl chains grafted on the SiO_2 NPs, the lowest IFT is achieved when the number of carbon atoms in the alkyl chains is 6 (i.e., JNP3).
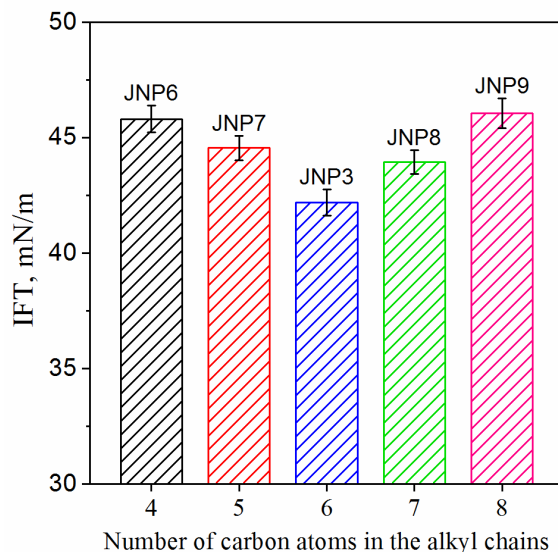
Figure 7-7 Effect of the number of carbon atoms in the alkyl chains on C_8H_{18}/water IFT.

7.3.3 Effect of NP interface coverage on oil/water IFT

The simulation results indicate that SiO_2 NPs reduce the IFT between oil and water only when they are located at the oil/water interface, which agrees with the findings in the literature (Li et al., 2019a; Moradi et al., 2015). The surface-modified NPs with only carboxylates, HNP2, remain in the water phase. Even though the bulk concentration of the NPs is much higher than that of many reported experimental studies, no IFT reductions were observed. The NP concentration in the bulk phase is not the fundamental factor affecting the oil/water IFT, while the NP concentration at the interface is. Similar to other simulation studies, the NP interface coverage was used to characterize the NP concentration at the interface (Luu et al., 2013a; Vu and Papavassiliou, 2019). The NP interface coverage was calculated as the percent of the interfacial area covered by NPs. JNP3 was selected for further investigating the effect of the NP interface coverage on oil/water IFT. The C_8H_{18}/water systems with a different number of JNP NPs at the interface were simulated. After

equilibrium, the NP interface coverages were calculated. In Fig. 8, we present the simulation snapshots of JNP3 NPs at C_8H_{18}/water interfaces.

(a)　　　　　　　(b)　　　　　　　(c)　　　　　　　(d)
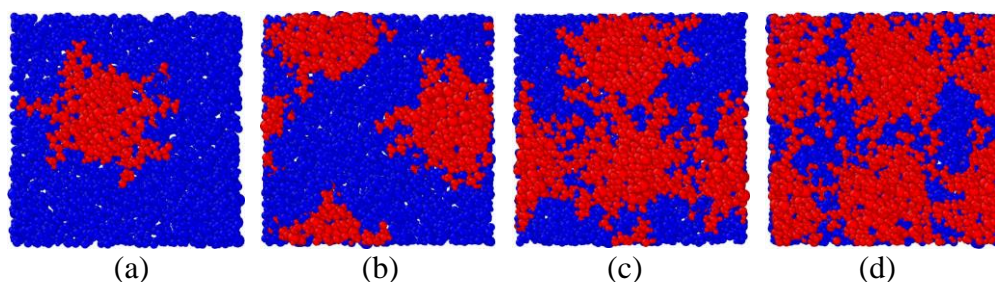
Figure 7-8 Top views of simulation snapshots for JNP3 NPs at the C_8H_{18}/water interface. Interface coverages are (a) 18.53%, (b) 34.91%, (c) 53.49%, and (d) 69.32%. Red and blue spheres represent atoms in JNP3 NPs and water, respectively. C_8H_{18} molecules are not shown for clarity.

The C_8H_{18}/water IFT of each system was also calculated. Variations of the IFT as a function of NP surface coverage is shown in Figure 7-9. When the JNP3 NPs cover 18.53% of the interface, the IFT is close to the pure C_8H_{18}/water IFT. The IFT decreases significantly only when the interface coverage is large enough.
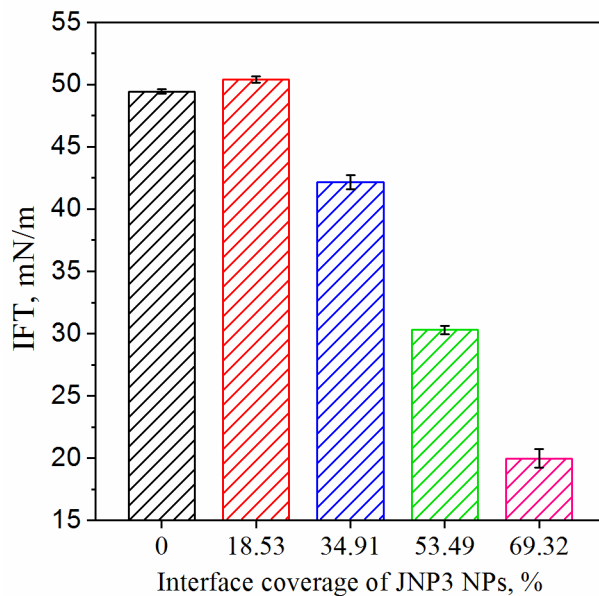
Figure 7-9 The IFT as a function of the interface coverage of JNP3 NPs

The IFT reduction depends strongly on the surface chemistry and the interface coverage of NPs, which is consistent with previously reported experimental observations (Glaser et al., 2006; Moradi et al., 2015; Saleh et al., 2005) and MD simulation results (Fan and Striolo, 2012; Liang et al., 2019; Luu et al., 2013a). Simulation results show that surface-modified NPs with both hydrophilic and hydrophobic functional groups can reduce the interfacial tension. From the simulation scenarios, the JNP3 shows the highest capability of reducing the IFT. However, the IFT reduction in the presence of NPs is not significant in terms of EOR application. A much lower IFT, such as that with surfactants, cannot be achieved. Although NPs individually can hardly reduce the oil/water IFT, a large number of studies have shown that NPs can increase the efficiency of surfactant in reducing the interfacial tension (Biswal et al., 2016; Li et al., 2019a; Mohajeri et al., 2015; Suleimanov et al., 2011; Sun et al., 2014). The synergistic effect between NPs and surfactants has not been well explained. Recently, Tuan V. and Dimitrios V. (Vu and Papavassiliou, 2019) explained the synergistic effect as NPs at the oil/water interface reduce the contact area between oil and water and leads to the less interfacial area available for surfactants, so that fewer surfactant molecules are needed to generate a larger IFT reduction than when they are alone at the interface. Besides, some investigators have reported that ellipsoidal Janus NPs (Luu et al., 2013b) and Janus cylinders (Ruhland et al., 2011) are more effective than spherical NPs in reducing the interfacial tension. Further studies are needed to verify the aforementioned research results.

7.3.4 Effect of rock wettability on oil transportation in nanochannels

The hydroxylated quartz nanochannel and methylated quartz nanochannel were selected to mimic the water-wet and oil-wet rock surfaces, respectively. As shown in Figure 7-10, oil droplets are easily detached from the water-wet surfaces and displaced out of the nanochannel at ~6 ns.
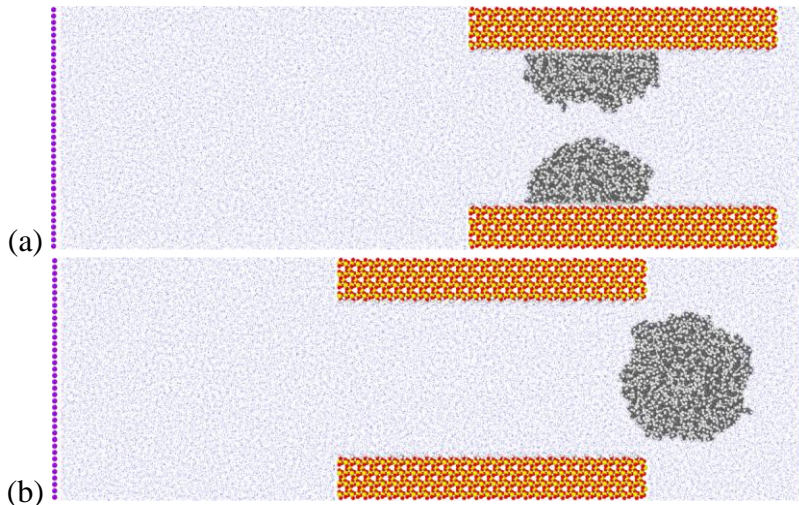
Figure 7-10 Adsorbed oil displacement in hydroxylated quartz nanochannel in the water injection

process: (a) 0 ns; (b) 6 ns.

In the oil-wet nanochannel, water cannot detach the oil droplets from the rock surfaces even after 16 ns simulation (Figure 7-11). The results show that the initial rock wettability affects waterflood behavior and oil recovery performance. Pure water cannot recover the residual oil from the nanopores in the oil-wet rocks.
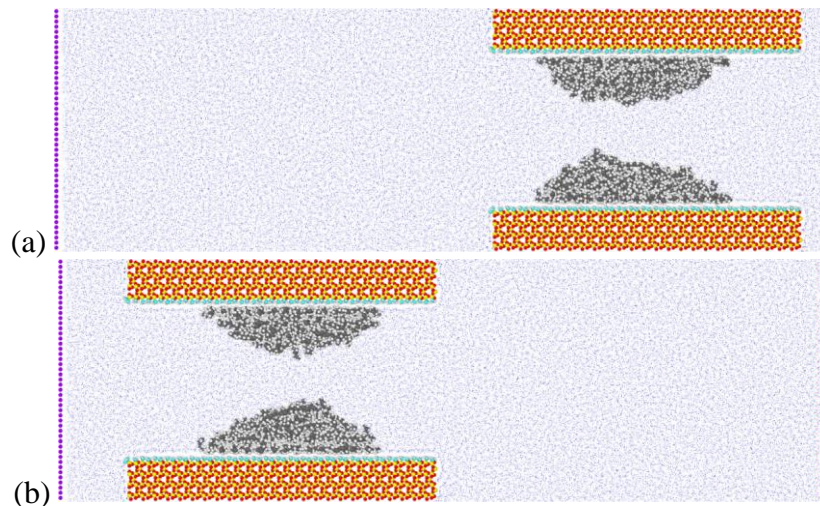
Figure 7-11 Adsorbed oil displacement in methylated quartz nanochannel in the water injection

process: (a) 0 ns; (b) 16 ns.

7.3.5 Effect of NPs on oil displacement in oil-wet nanochannels

Figure 7-12 shows the oil displacement processes in the oil-wet nanochannels with the injection of different nanofluids.
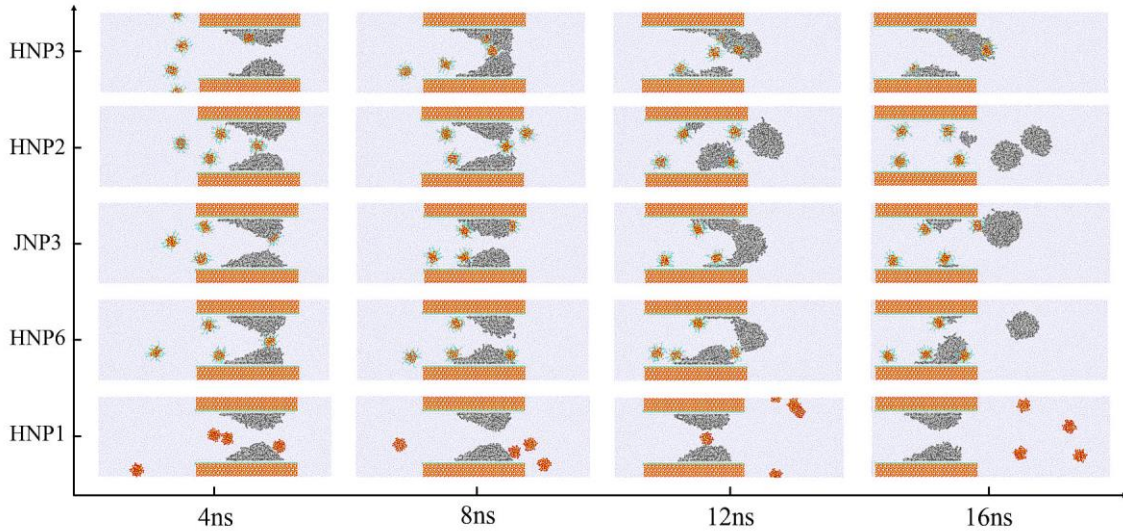
Figure 7-12 Adsorbed oil displacement in methylated quartz nanochannel in the nanofluid injection process.

Unmodified SiO_2 NPs (i.e., HNP1) cannot detach the adsorbed oil in the oil-wet nanochannel and totally move out of the nanochannel without attaching to the rock surfaces or the oil droplets. Both homogeneous amphiphilic NPs (i.e., HNP6) and Janus NPs (i.e., JNP3) can self-assemble at the oil/water interfaces or the oil/water/rock contact regions. These two types of NPs can detach the adsorbed oil from the rock surfaces, and partial oil molecules are displaced out of the nanochannels at the end of the simulations. Surface-modified NPs with alkyl chains (i.e. HNP3) almost mix with the adsorbed oil. The oil films are deformed, but no oil molecules are detached. Interestingly, surface-modified NPs with carboxylates (i.e. HNP2) are able to displace the adsorbed oil out of the oil-wet nanochannel, even though they cannot reduce the oil/water IFT.

For each simulation, the center of mass (COM) displacements of the adsorbed oil droplets along (x-direction) and perpendicular (z-direction) to the water flow direction were calculated. Figure 7-13 shows the COM displacement of the two oil droplets on the top and bottom slabs.
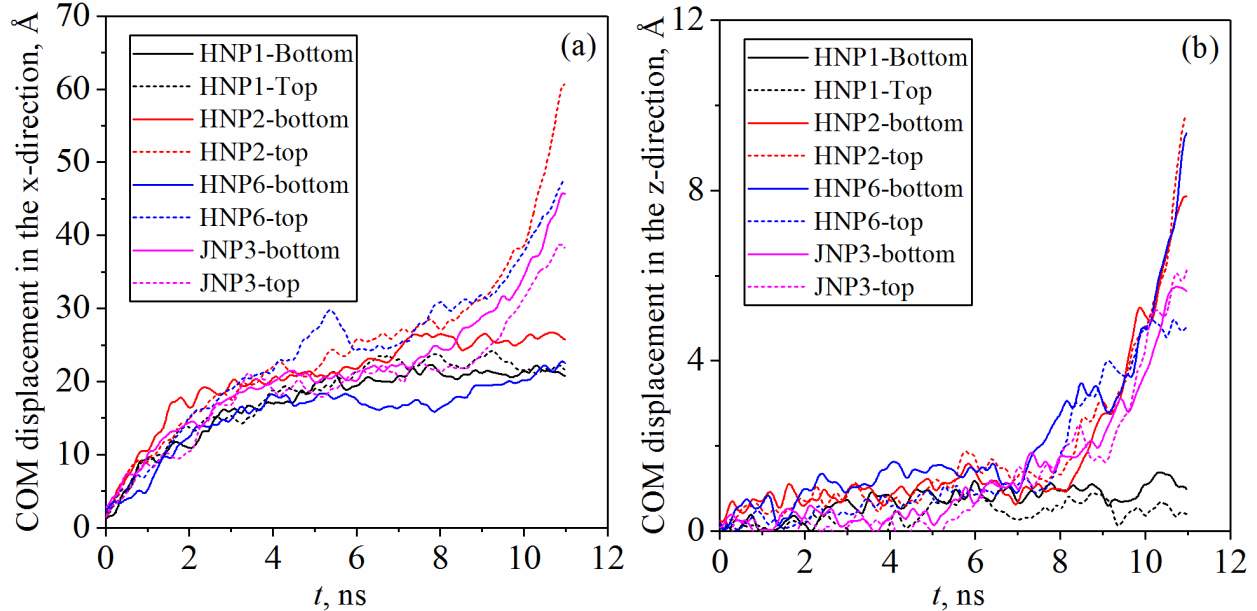
Figure 7-13 COM displacement of the adsorbed oil (a) along and (b) perpendicular to the water flow direction.

The movement speed of the adsorbed oil can be reflected from the slope of the COM displacement curve in the x-direction. The detachment speed of the adsorbed oil can be reflected from the slope of the curve in the z-direction. The addition of surface-modified NPs resulted in faster movement and detachment of the adsorbed oil, which can be indicated from the large slopes of the curves.

To explore the underlying oil detachment mechanism of different NPs, the interaction energies between oil and rock surfaces, water, or NPs were calculated as shown in Figure 7-14. Interactions between pure water and oil cannot overcome the adsorption action between oil molecules and rock surfaces. When the NPs contact with the adsorbed oil, homogeneous

amphiphilic NPs or Janus NPs can provide a driving force on the oil molecules and facilitate the detachment of adsorbed oil from the rock surfaces. The interaction energy calculations indicate that Janus NPs exert a greater driving force on the adsorbed oil than the other types of NPs. Compared with the JNP3 or HNP6 NPs, the HNP2 NPs interact more weakly with the oil phase.
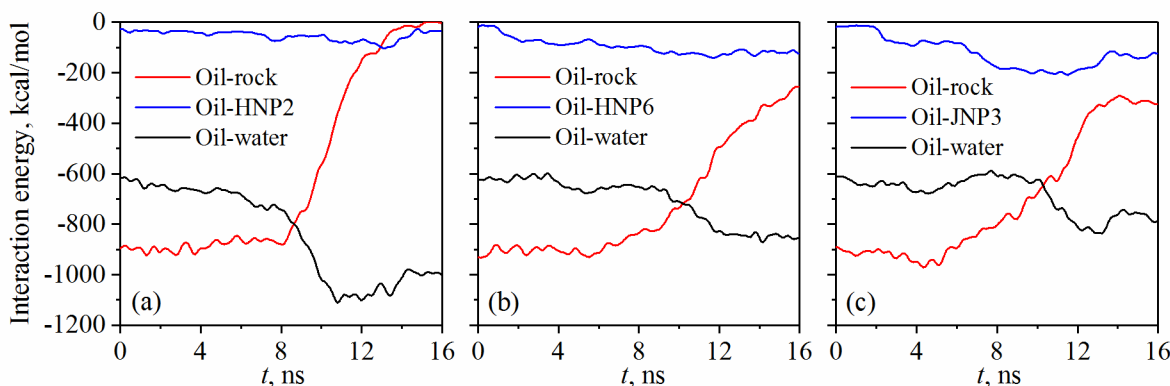
Figure 7-14 Interaction energies between oil and other components in the representative

simulation scenarios: (a) HNP2 NPs, (b) HNP6 NPs, (c) JNP3 NPs.

Interaction energies between different NPs and the rock surfaces (Figure 7-15) show that the HNP2 NPs interact more strongly with the rock surfaces than other types of NPs. The adsorption of the HNP2 NPs on the rock surfaces should be the main mechanism of the oil detachment. As shown in Figure 7-16, the adsorbed HNP2 NP resulted in the formation of gaps between the oil droplet and the rock surface, and then water molecules entered into the gap. With more water molecules entering into the gap, eventually, a water channel was formed and the adsorbed oil droplet was detached.
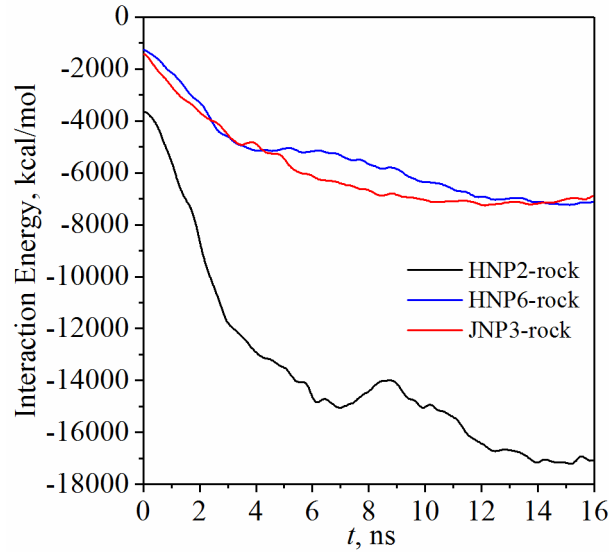
Figure 7-15 Interaction energies between different NPs and rock surfaces.
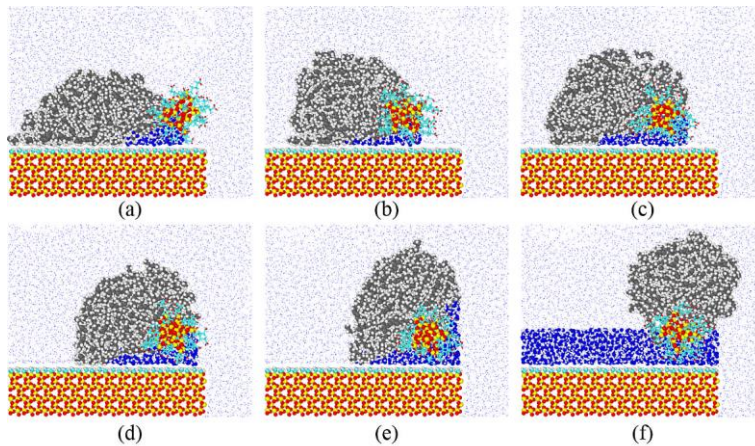
Figure 7-16 Effect of the HNP2 NP on the detachment of adsorbed oil.

The simulation results indicate that surface-modified NPs can improve the efficiency of oil detachment from the oil-wet rock surface. IFT change cannot be fully responsible for the oil detachment process since the IFTs of the C_8H_{18}/water system and C_8H_{18}/nanofluids system are very similar. The strong interactions between NPs and oil/rock account for the oil detachment and the incremental oil recovery. At the end of the simulations, some NPs are still adsorbed on the rock surfaces. As the NPs are partially or fully hydrophilic, the adsorbed NPs on the rock surfaces can

also change the wettability of the oil-wet rock to intermediate-wet or water-wet. As the type of functional group significantly affects the performance of NPs in detaching and displacing the adsorbed oil, different functional groups will be considered in future studies. The ratio and distribution of functional groups should be carefully tuned to achieve the largest incremental oil recovery.

7.4 Conclusions

Molecular dynamics simulations were used to assess the mechanisms of EOR associated with surface-modified nanoparticles (NPs) and nanofluid flooding. Surface-modified NPs with both hydrophilic and hydrophobic chains, also called amphiphilic NPs, can self-assemble at the oil/water interface and reduce the interfacial tension. However, the IFT reduction in the presence of NPs is not significant in terms of EOR application.

Simulation snapshots and interaction energy calculations indicate different EOR mechanisms of the surface-modified NPs. In the process of nanofluid flooding, homogenous amphiphilic NPs or Janus NPs can self-assemble at the oil/water interfaces or the oil/water/rock contact regions. The NPs modified with both carboxylates and alkyl chains exert a great driving force on the oil molecules and facilitate the detachment of adsorbed oil from the rock surfaces. While for the NPs modified with only carboxylates, the strong interaction between NPs and the rock surfaces play an important role in detaching the adsorbed oil.

Molecular simulations can provide molecular-level insights into the EOR processes and can guide scientists and engineers in designing NPs, which can effectively improve oil recovery.

CHAPTER 8

CONCLUSIONS AND RECOMMENDATIONS

In this dissertation, the characteristics of the Middle Bakken rock and oil were first summarized. Then, different potential EOR methods in the tight formation were evaluated using molecular simulations. For evaluating different properties of interest, bulk systems, interfacial systems, and nanoconfined systems were built and simulated.

Pressure, temperature, and oil composition are the main factors impacting the CO_2 solubility, and the density and swelling factor of the oil/CO_2 system. Both the CO_2 solubility and the swelling factor of the oil/CO_2 system increase with the increasing pressure and the decreasing temperature. The CO_2 solubility and swelling effect are more pronounced in light oil.

The viscosity of the n-alkane/CO_2 system is approximately in an inversely proportional relationship with the mole fraction of dissolved CO_2. The average viscosity reduction rate is about 45% when the CO_2 mole fraction is 60% under the reservoir condition.

Compared with CO_2 and CH_4, C_2H_6 has stronger attractive interaction with crude oil, and thus it is more soluble in crude oil and induces a more pronounced oil swelling. Meanwhile, C_2H_6 leads to a stronger oil diffusivity that is more effective in mobilizing crude oil. Furthermore, C_2H_6 is more favorable for the Bakken Formation since C_2H_6 is sufficient in the Bakken oil play, and there is no need for high injection pressure.

Without nano-confinement, the swelling extraction and mutual dissolution are the dominant factors affecting the oil detachment. C_2H_6 is more efficient than CO_2 in detaching adsorbed oil from the calcite surface. Considering the nano-confinement, competitive adsorption plays a more important role. CO_2 is more efficient than C_2H_6 in extracting oil from dead-end calcite nanochannel.

86

In the process of nanofluid flooding, homogenous amphiphilic NPs or Janus NPs can self-assemble at the oil/water interfaces or the oil/water/rock contact regions. The NPs modified with both carboxylates and alkyl chains exert a great driving force on the oil molecules and facilitate the detachment of adsorbed oil from the rock surfaces. While for the NPs modified with only carboxylates, the strong interaction between NPs and the rock surfaces play an important role in detaching the adsorbed oil.

Molecular simulations can provide molecular-level insights into the EOR processes. Better models are needed to predict the experimental results more accurately and guide the EOR projects in the Middle Bakken Formation and other tight formations.

REFERENCES

Abedini, A., & Torabi, F., 2014. On the CO_2 storage potential of cyclic CO_2 injection process for enhanced oil recovery. Fuel 124, 14–27.

Alahmadi, H.A.H., 2010. A triple-porosity model for fractured horizontal wells. Texas A&M University.

Alder, B.J., & Wainwright, T.E., 1959. Studies in molecular dynamics. I. General method. J. Chem. Phys. 31, 459–466.

Alder, B.J., & Wainwright, T.E., 1957. Phase transition for a hard sphere system. J. Chem. Phys. 27, 1208–1209.

Alharthy, N.S., Nguyen, T.N., Teklu, T.W., et al., 2013. Multiphase compositional modeling in small-scale pores of unconventional shale reservoirs. Presented at the SPE Annual Technical Conference and Exhibition, New Orleans, Louisiana, USA, September 30–October 2.

Allen, M.P., & Tildesley, D.J., 1989. Computer simulation of liquids. Oxford University Press, Oxford, UK.

Alvarado, V., & Manrique, E., 2010. Enhanced oil recovery: An update review. Energies 3, 1529–1575.

Arif, M., Lebedev, M., Barifcani, A., et al., 2017. Influence of shale-total organic content on CO_2 geo-storage potential. Geophys. Res. Lett. 44, 8769–8775.

Assef, Y., & Almao, P.P., 2019. Evaluation of cyclic gas injection in enhanced recovery from unconventional light oil reservoirs: Effect of gas type and fracture spacing. Energies 12, 1370.

Awan, A.R., Teigland, R., & Kleppe, J., 2008. A survey of North Sea enhanced-oil-recovery

projects initiated during the years 1975 to 2005. SPE Reserv. Eval. Eng. 11, 497–512.

Aycaguer, A.C., Lev-On, M., & Winer, A.M., 2001. Reducing carbon dioxide emissions with enhanced oil recovery projects: A life cycle assessment approach. Energy & Fuels 15, 303–308.

Bagwe, R.P., Hilliard, L.R., & Tan, W., 2006. Surface modification of silica nanoparticles to reduce aggregation and nonspecific binding. Langmuir 22, 4357–4362.

Berendsen, H.J.C., Grigera, J.R., & Straatsma, T.P., 1987. The missing term in effective pair potentials. J. Phys. Chem. 91, 6269–6271.

Biswal, N.R., Rangera, N., & Singh, J.K., 2016. Effect of different surfactants on the interfacial behavior of the n-hexane-water system in the presence of silica nanoparticles. J. Phys. Chem. B 120, 7265–7274.

Cai, H.Y., Zhang, Y., Liu, Z.Y., et al., 2018. Molecular dynamics simulation of binary betaine and anionic surfactant mixtures at decane-water interface. J. Mol. Liq. 266, 82–89.

Chen, C., Wan, J., Li, W., et al., 2015. Water contact angles on quartz surfaces under supercritical CO_2 sequestration conditions : Experimental and molecular dynamics simulation studies. Int. J. Greenh. Gas Control 42, 655–665.

Chen, C., Wang, S., Kadhum, M.J., et al., 2018. Using carbonaceous nanoparticles as surfactant carrier in enhanced oil recovery: A laboratory study. Fuel 222, 561–568.

Chen, Y., & Xu, G., 2013. Improvement of Ca^{2+}-tolerance by the introduction of EO groups for the anionic surfactants: Molecular dynamics simulation. Colloids Surfaces A: Physicochem. Eng. Asp. 424, 26–32.

Chun, B.J., Choi, J. Il, & Jang, S.S., 2015. Molecular dynamics simulation study of sodium dodecyl sulfate micelle: Water penetration and sodium dodecyl sulfate dissociation.

Colloids Surfaces A: Physicochem. Eng. Asp. 474, 36–43.

Chung, F.T.H., Jones, R.A., & Nguyen, H.T., 1988. Measurements and correlations of the physical properties of CO_2/heavy-crude-oil mixtures. SPE Reserv. Eng. 3, 822–828.

Clark, A.J., 2009. Determination of recovery factor in the Bakken Formation, Mountrail County, ND. Presented at the SPE Annual Technical Conference and Exhibition. New Orleans, Louisiana, USA, Octobor 4–7.

Cygan, R.T., Liang, J.-J., & Kalinichev, A.G., 2004. Molecular models of hydroxide, oxyhydroxide, and clay phases and the development of a general force field. J. Phys. Chem. B 108, 1255–1266.

De Almeida, J.M., & Miranda, C.R., 2016. Improved oil recovery in nanopores: NanoIOR. Sci. Rep. 6, 1–11.

De Lara, L.S., Michelon, M.F., & Miranda, C.R., 2012. Molecular dynamics studies of fluid/oil interfaces for improved oil recovery processes. J. Phys. Chem. B 116, 14667–14676.

Dong, X., Shi, Y., & Yang, D., 2018. Quantification of mutual mass transfer of CO_2/N2–light oil systems by dynamic volume analysis. Ind. & Eng. Chem. Res. 57, 16495–16507.

Dubbeldam, D., Calero, S., Ellis, D.E., et al., 2016. RASPA: Molecular simulation software for adsorption and diffusion in flexible nanoporous materials. Mol. Simul. 42, 81−101.

Dubbeldam, D., Calero, S., Vlugt, T.J.H., et al., 2004. United atom force field for alkanes in nanoporous materials. J. Phys. Chem. B 108, 12301–12313.

Ewen, J.P., Gattinoni, C., Thakkar, F.M., et al., 2016. A comparison of classical force-fields for molecular dynamics simulations of lubricants. Materials 9, 1–17.

Falk, K., Sedlmeier, F., Joly, L., et al., 2012. Ultralow liquid/solid friction in carbon nanotubes: Comprehensive theory for alcohols, alkanes, OMCTS, and water. Langmuir 28, 14261−

14272.

Fan, H., Resasco, D.E., & Striolo, A., 2011. Amphiphilic silica nanoparticles at the decane-water interface: Insights from atomistic simulations. Langmuir 27, 5264–5274.

Fan, H., & Striolo, A., 2012. Nanoparticle effects on the water-oil interfacial tension. Phys. Rev. E 86, 051610.

Fang, T., Wang, M., Wang, C., et al., 2017. Oil detachment mechanism in CO_2 flooding from silica surface: Molecular dynamics simulation. Chem. Eng. Sci. 164, 17–22.

Frenkel, D., Mooij, G.C.A.M., & Smit, B., 1992. Novel scheme to study structural and thermal properties of continuously deformable molecules. J. Phys. Condens. Matter 4, 3053–3076.

Gaspar Ravagnani, A.T.F.S., Ligero, E.L., & Suslick, S.B., 2009. CO_2 sequestration through enhanced oil recovery in a mature oil field. J. Pet. Sci. Eng. 65, 129–138.

Glaser, N., Adams, D.J., Böker, A., et al., 2006. Janus particles at liquid-liquid interfaces. Langmuir 22, 5227–5229.

Gogoi, S.B., 2011. Adsorption-desorption of surfactant for enhanced oil recovery. Transp. Porous Media 90, 589–604.

Green, M.S., 1954. Markoff random processes and the statistical mechanics of time-dependent phenomena. II. Irreversible processes in fluids. J. Chem. Phys. 22, 398−413.

Han, H., Yuan, S., Li, S., et al., 2015. Dissolving capacity and volume expansion of carbon dioxide in chain n-alkanes. Pet. Explor. Dev. 42, 97–103.

Hardy, D.J., Stone, J.E., & Schulten, K., 2009. Multilevel summation of electrostatic potentials using graphics processing units. Parallel Comput. 35, 164–177.

Hawthorne, S.B., & Miller, D.J., 2019. A comparison of crude oil hydrocarbon mobilization by vaporization gas drive into methane, ethane, and carbon dioxide at 15.6 MPa and 42 °C.

Fuel 249, 392–399.

Hawthorne, Steven B., Miller, D.J., Grabanski, C.B., et al., 2019. Hydrocarbon recovery from Williston Basin shale and mudrock cores with supercritical CO_2 : Part 1. method validation and recoveries from cores collected across the basin. Energy & Fuels 33, 6857–6866.

Hawthorne, S.B., Miller, D.J., Grabanski, C.B., et al., 2017. Measured crude oil MMPs with pure and mixed CO_2, methane, and ethane, and their relevance to enhanced oil recovery from middle bakken and bakken shales.Presented at the SPE Unconventional Resources Conference, Calgary, Alberta, Canada, February 15-16.

Hawthorne, S.B., Miller, D.J., Jin, L., et al., 2016. Rapid and simple capillary-rise/vanishing interfacial tension method to determine crude oil minimum miscibility pressure: Pure and mixed CO_2 , methane, and ethane. Energy & Fuels 30, 6365–6372.

Hawthorne, Steven B, Sorensen, J.A., Miller, D.J., et al., 2019. Laboratory studies of rich gas interactions with Bakken crude oil to support enhanced oil recovery. Presented at the Unconventional Resources Technology Conference. Denver, Colorado, USA, July 22-24.

Hendraningrat, L., Li, S., & Torsæter, O., 2013. A coreflood investigation of nanofluid enhanced oil recovery. J. Pet. Sci. Eng. 111, 128–138.

Hendraningrat, L., & Torsæter, O., 2014. Effects of the initial rock wettability on silica-based nanofluid-enhanced oil recovery processes at reservoir temperatures. Energy & Fuels 28, 6228–6241.

Herdes, C., Petit, C., Mejá, A., et al., 2018. Combined experimental, theoretical, and molecular simulation approach for the description of the fluid-phase behavior of hydrocarbon mixtures within shale rocks. Energy & Fuels 32, 5750–5762.

Herdes, C., Totton, T.S., & Müller, E.A., 2015. Coarse grained force field for the molecular

simulation of natural gases and condensates. Fluid Phase Equilib. 406, 91–100.

Ho, T.A., Wang, Y., Xiong, Y., et al., 2018. Differential retention and release of CO_2 and CH_4 in kerogen nanopores: Implications for gas extraction and carbon sequestration. Fuel 220, 1–7.

Hockney, R.W., & Eastwood, J.W., 1989. Computer Simulation Using Particles. CRC Press, New York.

Hoover, W.G., Ladd, A.J.C., & Moran, B., 1982. High-strain-rate plastic flow studied via nonequilibrium molecular dynamics. Phys. Rev. Lett. 48, 1818.

Hu, X., Li, Y., He, X., et al., 2012. Structure-behavior-property relationship study of surfactants as foam stabilizers explored by experimental and molecular simulation approaches. J. Phys. Chem. B 116, 160–167.

Humphrey, W., Dalke, A., & Schulten, K., 1996. VMD: Visual Molecular Dynamics. J. Mol. Graph. 14, 33–38.

Iwere, F.O., Heim, R.N., & Cherian, B. V., 2012. Numerical simulation of enhanced oil recovery in the middle Bakken and upper three forks tight oil reservoirs of the Williston basin, in: Americas Unconventional Resources Conference 2012. Pittsburgh, Pennsylvania, USA.

Jalili, S., & Akhavan, M., 2009. A coarse-grained molecular dynamics simulation of a sodium dodecyl sulfate micelle in aqueous solution. Colloids Surfaces A: Physicochem. Eng. Asp. 352, 99–102.

Jang, H., Lee, W., & Lee, J., 2018. Nanoparticle dispersion with surface-modified silica nanoparticles and its effect on the wettability alteration of carbonate rocks. Colloids Surfaces A: Physicochem. Eng. Asp. 554, 261–271.

Jia, B., Tsau, J.S., & Barati, R., 2019. A review of the current progress of CO_2 injection EOR and carbon storage in shale oil reservoirs. Fuel 236, 404–427.

Jin, L., Hawthorne, S., Sorensen, J., et al., 2016. A systematic investigation of gas-based
improved oil recovery technologies for the Bakken tight oil formation. Presented at the
Unconventional Resources Technology Conference. San Antonio, Texas, USA, August 1-3.

Jorgensen, W.L., Maxwell, D.S., & Tirado-Rives, J., 1996. Development and testing of the
OPLS all-atom force field on conformational energetics and properties of organic liquids. J.
Am. Chem. Soc. 118, 11225–11236.

Josh, M., Esteban, L., Delle Piane, C., et al., 2012. Laboratory characterisation of shale
properties. J. Pet. Sci. Eng. 88–89, 107–124.

Kamal, M.S., Adewunmi, A.A., Sultan, A.S., et al., 2017a. Recent advances in nanoparticles
enhanced oil recovery : rheology , interfacial tension , oil recovery , and wettability
alteration. J. Nanomater. 1–15.

Kamal, M.S., Hussein, I.A., & Sultan, A.S., 2017b. Review on surfactant flooding: phase
behavior, retention, ift, and field applications. Energy & Fuels 31, 7701–7720.

Katiyar, P., & Singh, J.K., 2017. A coarse-grain molecular dynamics study of oil-water
interfaces in the presence of silica nanoparticles and nonionic surfactants. J. Chem. Phys.
146, 204702.

Kubo, R., 1957. Statistical mechanical theory of irreversible processes. I. general theory and
simple applications to magnetic and conduction problems. J. Phys. Soc. Japan 12, 570−586.

Kurtoglu, B., 2014. Integrated reservoir characterization and modeling in support of enhanced oil
recovery for Bakken. Colorado School of Mines.

Kurtoglu, B., Sorensen, J.A., Braunberger, J., et al., 2013. Geologic characterization of a bakken
reservoir for potential CO_2 EOR, Presented at the Unconventional Resources Technology
Conference, Denver, Colorado, USA, August 12-14.

Kuuskraa, V.A., Godec, M.L., & Dipietro, P., 2013. CO_2 utilization from "next generation" CO_2 enhanced oil recovery technology. Energy Procedia 37, 6854–6866.

Labani, M.M., Rezaee, R., Saeedi, A., et al., 2013. Evaluation of pore size spectrum of gas shale reservoirs using low pressure nitrogen adsorption, gas expansion and mercury porosimetry: A case study from the Perth and Canning Basins, Western Australia. J. Pet. Sci. Eng. 112, 7–16.

Le, T., Ogbe, S., Striolo, A., et al., 2016. N-octane diffusivity enhancement via carbon dioxide in silica slit-shaped nanopores-a molecular dynamics simulation. Mol. Simul. 42, 745–752.

Le, T., Striolo, A., & Cole, D.R., 2015. CO_2-C_4H_{10} mixtures simulated in silica slit pores: Relation between structure and dynamics. J. Phys. Chem. C 119, 15274–15284.

LeFever, J., & Helms, L., 2006. Bakken Formation Reserve Estimates. North Dakota Geol. Surv.

Lemmon, E.W., McLinden, M.O., Friend, D.G., et al., 2011. NIST chemistry webBook, NIST standard reference database number 69. National Institute of Standards and Technology. Gaithersburg, MD, USA.

Li, C., Pu, H., Zhang, S., et al., 2019a. Effect of nanoparticles and surfactants on oil/water interfacial tension: A coarse-grained molecular dynamics simulation study. Presented at the Unconventional Resources Technology Conference, Denver, Colorado, USA, July 22-24.

Li, C., Pu, H., & Zhao, J.X., 2019b. Molecular simulation study on the volume swelling and the viscosity reduction of n-alkane/CO_2 systems. Ind. Eng. Chem. Res. 58, 8871–8877.

Li, C., Pu, H., Zhong, X., et al., 2020. Interfacial interactions between Bakken crude oil and injected gases at reservoir temperature: A molecular dynamics simulation study. Fuel 276, 118058.

Li, L., & Sheng, J.J., 2016. Experimental study of core size effect on CH_4 huff-n-puff enhanced

oil recovery in liquid-rich shale reservoirs. J. Nat. Gas Sci. Eng. 34, 1392–1402.

Li, L., Zhang, Y., & Sheng, J.J., 2017. Effect of the injection pressure on enhancing oil recovery in shale cores during the CO_2 huff-n-puff process when it is above and below the minimum miscibility pressure. Energy & Fuels 31, 3856–3867.

Liang, S., Fang, T., Xiong, W., et al., 2019. Oil detachment by modified nanoparticles: A molecular dynamics simulation study. Comput. Mater. Sci. 170, 109177.

Liu, B., Shi, J., Sun, B., et al., 2015. Molecular dynamics simulation on volume swelling of CO_2-alkane system. Fuel 143, 194-201.

Liu, B., Shi, J., Wang, M., et al., 2016. Reduction in interfacial tension of water-oil interface by supercritical CO_2 in enhanced oil recovery processes studied with molecular dynamics simulation. J. Supercrit. Fluids 111, 171–178.

Liu, B., Wang, C., Zhang, J., et al., 2017. Displacement mechanism of oil in shale inorganic nanopores by supercritical carbon dioxide from molecular dynamics simulations. Energy & Fuels 31, 738–746.

Liu, H., Dai, S., & Jiang, D.E., 2014. Molecular dynamics simulation of anion effect on solubility, diffusivity, and permeability of carbon dioxide in ionic liquids. Ind. Eng. Chem. Res. 53, 10485− 10490.

Liu, K., Ostadhassan, M., Zhou, J., et al., 2017. Nanoscale pore structure characterization of the Bakken shale in the USA. Fuel 209, 567–578.

López-Lemus, J., Romero-Bastida, M., Darden, T.A., et al., 2006. Liquid-vapour equilibrium of n -alkanes using interface simulations. Mol. Phys. 104, 2413–2421.

Lorenz, C.D., Webb, E.B., Stevens, M.J., et al., 2005. Frictional dynamics of perfluorinated self-assembled monolayers on amorphous SiO_2. Tribol. Lett. 19, 93–99.

Loucks, R.G., Reed, R.M., Ruppel, S.C., et al., 2012. Spectrum of pore types and networks in

    mudrocks and a descriptive classification for matrix-related mudrock pores. Am. Assoc.

    Pet. Geol. Bull. 96, 1071–1098.

Luu, X.C., Yu, J., & Striolo, A., 2013a. Nanoparticles adsorbed at the water/oil interface:

    Coverage and composition effects on structure and diffusion. Langmuir 29, 7221–7228.

Luu, X.C., Yu, J., & Striolo, A., 2013b. Ellipsoidal Janus nanoparticles adsorbed at the water-oil

    interface: Some evidence of emergent behavior. J. Phys. Chem. B 117, 13922–13929.

Macías-Salinas, R., Chávez-Velasco, J.A., Aquino-Olivos, M.A., et al., 2013. Accurate modeling

    of CO_2 solubility in ionic liquids using a cubic EoS. Ind. Eng. Chem. Res. 52, 7593−7601.

Makimura, D., Kunieda, M., Liang, Y., et al., 2013. Application of molecular simulations to

    CO_2-Enhanced oil recovery: Phase equilibria and interfacial phenomena. SPE J. 18, 319–

    330.

Manrique, E.J., Engineering, N.Q., Muci, V.E., et al., 2007. EOR field experiences in carbonate

    reservoirs in the United States. SPE Reserv. Eval. Eng. 10, 667−686.

Martin, F.D., 1983. Technical screening guides for the enhanced recovery of oil. Presented at the

    SPE Annual Technical Conference and Exhibition. San Francisco, California, USA,

    October 5-8.

Martin, F.D., & Taber, J.J., 1992. Carbon dioxide flooding. J. Pet. Technol. 44, 396–400.

Martin, M.G., & Siepmann, J.I., 1999. Novel Configurational-Bias Monte Carlo method for

    branched molecules. transferable potentials for phase equilibria. 2. united-atom description

    of branched alkanes. J. Phys. Chem. B 103, 4508–4517.

Martin, M.G., & Siepmann, J.I., 1998. Transferable potentials for phase equilibria. 1. united-

    atom description of n-alkanes. J. Phys. Chem. B 102, 2569–2577.

Metropolis, N., Rosenbluth, A.W., Rosenbluth, M.N., et al., 1953. Equation of state calculations by fast computing machines. J. Chem. Phys. 21, 1087–1092.

Mohajeri, M., Hemmati, M., & Shekarabi, A.S., 2015. An experimental study on using a nanosurfactant in an EOR process of heavy oil in a fractured micromodel. J. Pet. Sci. Eng. 126, 162–173.

Moradi, B., Pourafshary, P., Jalali, F., et al., 2015. Experimental study of water-based nanofluid alternating gas injection as a novel enhanced oil-recovery method in oil-wet carbonate reservoirs. J. Nat. Gas Sci. Eng. 27, 64–73.

Mosavat, N., Abedini, A., & Torabi, F., 2014. Phase behaviour of CO_2-brine and CO_2-oil systems for CO_2 storage and enhanced oil recovery: Experimental studies. Energy Procedia 63, 5631–5645.

Moultos, O.A., Tsimpanogiannis, I.N., Panagiotopoulos, A.Z., et al., 2016. Atomistic molecular dynamics simulations of carbon dioxide diffusivity in n-hexane, n-decane, n-hexadecane, cyclohexane, and squalane. J. Phys. Chem. B 120, 12890–12900.

Müller, E.A., Herdes, C., & Totton, T.S., 2015. Coarse-grained models for crude oils: A direct link between equations of state and molecular simulations. Presented at the Offshore Technology Conference Brasil, Rio de Janeiro, Brazil, October 27–29.

Mulliken, C.A., & Sandler, S.I., 1980. The prediction of CO_2 solubility and swelling factors for enhanced oil recovery. Ind. Eng. Chem. Process Des. Dev. 19, 709−71.

Nath, S.K., Escobedo, F.A., & De Pablo, J.J., 1998. On the simulation of vapor-liquid equilibria for alkanes. J. Chem. Phys. 108, 9905–9911.

Nazari Moghaddam, R., Bahramian, A., Fakhroueian, Z., et al., 2015. Comparative study of using nanoparticles for enhanced oil recovery: Wettability alteration of carbonate rocks.

Energy & Fuels 29, 2111–2119.

Ndao, M., Devémy, J., Ghoufi, A., et al., 2015. Coarse-graining the liquid-liquid interfaces with the MARTINI force field: How is the interfacial tension reproduced? J. Chem. Theory Comput. 11, 3818–3828.

Negin, C., Ali, S., & Xie, Q., 2017. Most common surfactants employed in chemical enhanced oil recovery. Petroleum 3, 197–211.

Nelson, P.H., 2009. Pore-throat sizes in sandstones, tight sandstones, and shales. Am. Assoc. Pet. Geol. Bull. 93, 329–340.

Nosé, S., 1984. A unified formulation of the constant temperature molecular dynamics methods. J. Chem. Phys. 81, 511–519.

Orr, F.M., Heller, J.P., & Taber, J.J., 1982. Carbon dioxide flooding for enhanced oil recovery: Promise and problems. J. Am. Oil Chem. Soc. 59, 810A-817A.

Pan, B., Li, Y., Wang, H., et al., 2018. CO_2 and CH_4 Wettabilities of organic-rich shale. Energy & Fuels 32, 1914–1922.

Papavasileiou, K.D., Peristeras, L.D., Bick, A., et al., 2019. Molecular dynamics simulation of pure n-alkanes and their mixtures at elevated temperatures using atomistic and coarse-grained force fields. J. Phys. Chem. B 123, 6229–6243.

Peng, F., Wang, R., Guo, Z., et al., 2018. Molecular dynamics simulation to estimate minimum miscibility pressure for oil with pure and impure CO_2. J. Phys. Commun. 2, 115028.

Perera, M.S.A., Gamage, R.P., Rathnaweera, T.D., et al., 2016. A review of CO_2-enhanced oil recovery with a simulated sensitivity analysis. Energies 9, 481.

Phillips, Z.D., Halverson, R.J., Strauss, S.R., et al., 2007. A case study in the Bakken formation: Changes to hydraulic fracture stimulation treatments result in improved oil production and

reduced treatment costs. Presented at the Rocky Mountain Oil and Gas Technology
Symposium, Denver, Colorado, USA, April 16-18.

Plimpton, S., 1995. Fast parallel algorithms for short-range molecular dynamics. J. Comput.
Phys. 117, 1–19.

Potoff, J.J., & Siepmann, J.I., 2001. Vapor-liquid equilibria of mixtures containing alkanes,
carbon dioxide, and nitrogen. AIChE J. 47, 1676–1682.

Qiao, B., Liang, Y., Wang, T.J., et al., 2016. Surface modification to produce hydrophobic nano-
silica particles using sodium dodecyl sulfate as a modifier. Appl. Surf. Sci. 364, 103–109.

Qin, J., Han, H., & Liu, X., 2015. Application and enlightenment of carbon dioxide flooding in
the United States of America. Pet. Explor. Dev. 42, 209–216.

Qu, G., Xue, C., Zhang, M., et al., 2016. Molecular dynamics simulation of sulfobetaine-type
zwitterionic surfactants at the decane/water interface: structure, interfacial properties. J.
Dispers. Sci. Technol. 37, 1710–1717.

Rao, D.N., 1997. A new technique of vanishing interfacial tension for miscibility determination.
Fluid Phase Equilib. 139, 311–324.

Rouquerol, J., Avnir, D., Fairbridge, C.W., et al., 1994. Recommendations for the
characterization of porous solids (technical report). Pure Appl. Chem. 66, 1739–1758.

Ruhland, T.M., Gröschel, A.H., Walther, A., et al., 2011. Janus cylinders at liquid-liquid
interfaces. Langmuir 27, 9807–9814.

Ruiz-Morales, Y., & Romero-Martínez, A., 2018. Coarse-grain molecular dynamics simulations
to investigate the bulk viscosity and critical micelle concentration of the ionic surfactant
sodium dodecyl sulfate (SDS) in aqueous solution. J. Phys. Chem. B 122, 3931–3943.

Ryckaert, J.P., Ciccotti, G., & Berendsen, H.J.C., 1977. Numerical integration of the cartesian

equations of motion of a system with constraints: molecular dynamics of n-alkanes. J. Comput. Phys. 23, 327−341.

Saleh, N., Sarbu, T., Sirk, K., et al., 2005. Oil-in-water emulsions stabilized by highly charged polyelectrolyte-grafted silica nanoparticles. Langmuir 21, 9873–9878.

Sammalkorpi, M., Karttunen, M., & Haataja, M., 2007. Structural properties of ionic detergent aggregates: A large-scale molecular dynamics study of sodium dodecyl sulfate. J. Phys. Chem. B 111, 11722–11733.

Saraji, S., & Piri, M., 2015. The representative sample size in shale oil rocks and nano-scale characterization of transport properties. Int. J. Coal Geol. 146, 42–54.

Seyyedsar, S.M., Farzaneh, S.A., & Sohrabi, M., 2017. Investigation of low-density CO_2 injection for enhanced oil recovery. Ind. Eng. Chem. Res. 56, 5443−5454.

Siepmann, J.I., & Frenke, D., 1992. Configurational Bias Monte Carlo: A new sampling scheme for flexible chains. Mol. Phys. An Int. J. Interface Between Chem. Phys. 75, 59–70.

Simoes Santos, M., Franco, L., Castier, M., et al., 2018. Molecular dynamics simulation of n-alkanes and CO_2 confined by calcite nanopores. Energy & Fuels 32, 1934–1941.

Simon, R., & Graue, D.J., 1964. Generalized correlations for predicting volubility,swelling viscosity behavior of CO_2-crude oil systems. J. Pet. Sci. Eng. 17, 102–106.

Siu, S.W.I., Pluhackova, K., & Böckmann, R.A., 2012. Optimization of the OPLS-AA force field for long hydrocarbons. J. Chem. Theory Comput. 8, 1459–1470.

Šolc, R., Gerzabek, M.H., Lischka, H., et al., 2011. Wettability of kaolinite (001) surfaces - Molecular dynamic study. Geoderma 169, 47–54.

Sorensen, J.A., Braunberger, J.R., Liu, G., et al., 2015. Characterization and evaluation of the Bakken petroleum system for CO_2 enhanced oil recovery. Presented at the Unconventional

Resources Technology Conference, San Antonio, Texas, USA, July 20-22.

Sorensen, J.A., Braunberger, J.R., Liu, G., et al., 2014. CO_2 storage and utilization in tight hydrocarbon-bearing formations: A case study of the bakken formation in the williston basin. Energy Procedia 63, 7852–7860.

Sorensen, J.A., Kurz, B.A., Hawthorne, S.B., et al., 2017. Laboratory characterization and modeling to examine CO_2 storage and enhanced oil recovery in an unconventional tight oil formation. Energy Procedia 114, 5460–5478.

Stukowski, A., 2010. Visualization and analysis of atomistic simulation data with OVITO-the Open Visualization Tool. Model. Simul. Mater. Sci. Eng. 18, 015012.

Suebsiri, J., Wilsan, M., & Tontiwachwuthikul, P., 2006. Life-cycle analysis of CO_2 EOR on EOR and geological storage through economic optimization and sensitivity analysis using the weyburn unit as a case study. Ind. Eng. Chem. Res. 45, 2483−2488.

Suleimanov, B.A., Ismailov, F.S., & Veliyev, E.F., 2011. Nanofluid for enhanced oil recovery. J. Pet. Sci. Eng. 78, 431–437.

Sun, Q., Li, Z., Li, S., et al., 2014. Utilization of surfactant-stabilized foam for enhanced oil recovery by adding nanoparticles. Energy & Fuels 28, 2384–2394.

Sun, X., Zhang, Y., Chen, G., et al., 2017. Application of nanoparticles in enhanced oil recovery: A critical review of recent progress. Energies 10, 345.

Tang, X., Koenig, P.H., & Larson, R.G., 2014. Molecular dynamics simulations of sodium dodecyl sulfate micelles in water - The effect of the force field. J. Phys. Chem. B 118, 3864–3880.

Tang, X., Xiao, S., Lei, Q., et al., 2019. Molecular dynamics simulation of surfactant flooding driven oil-detachment in nano-silica channels. J. Phys. Chem. B 123, 277–288.

Tenney, C.M., & Cygan, R.T., 2014. Molecular simulation of carbon dioxide, brine, and clay mineral interactions and determination of contact angles. Environ. Sci. Technol. 48, 2035–2042.

Toukmaji A.Y., & Board J.A., 1996. Ewald summation techniques in perspective: a survey. Comput. Phys. Commun. 95, 73–92.

Ungerer, P., Nieto-Draghi, C., Lachet, V., et al., 2007. Molecular simulation applied to fluid properties in the oil and gas industry. Mol. Simul. 33, 287–304.

Ungerer1, P., Lachet1, V., & Tavitian1, B., 2006. Applications of molecular simulation in oil and gas production and processing. Oil Gas Sci. Technol. 61, 387–403.

Urukova, I., Pérez-Salado Kamps, Á., & Maurer, G., 2009. Solubility of CO_2 in (water + acetone): Correlation of experimental data and predictions from molecular simulation. Ind. & Eng. Chem. Res. 48, 4553–4564.

Vorholz, J., Harismiadis, V.I., Panagiotopoulos, A.Z., et al., 2004. Molecular simulation of the solubility of carbon dioxide in aqueous solutions of sodium chloride. Fluid Phase Equilib. 226, 237–250.

Vu, T. V., & Papavassiliou, D. V., 2019. Synergistic effects of surfactants and heterogeneous nanoparticles at oil-water interface: Insights from computations. J. Colloid Interface Sci. 553, 50–58.

Wang, R., Peng, F., Song, K., et al., 2018. Molecular dynamics study of interfacial properties in CO_2 enhanced oil recovery. Fluid Phase Equilib. 467, 25–32.

Wang, S., Feng, Q., Javadpour, F., et al., 2016a. Breakdown of fast mass transport of methane through calcite nanopores. J. Phys. Chem. C 120, 14260–14269.

Wang, S., Feng, Q., Zha, M., et al., 2015. Molecular dynamics simulation of liquid alkane

occurrence state in pores and slits of shale organic matter. Pet. Explor. Dev. 42, 844–851.

Wang, S., Javadpour, F., & Feng, Q., 2016b. Molecular dynamics simulations of oil transport through inorganic nanopores in shale. Fuel 171, 74–86.

Wang, S., & Larson, R.G., 2015. Coarse-grained molecular dynamics simulation of self-assembly and surface adsorption of ionic surfactants using an implicit water model. Langmuir 31, 1262–1271.

Welker, J.R., & Dunlop, D.D., 1963. Physical properties of carbonated oils. J. Pet. Technol. 15, 873–876.

West, D.R.M., Harkrider, J.D., Besler, M.R., et al., 2013. Optimized production in the Bakken shale : south antelope case study. Presented at the SPE Unconventional Resources Conference, Calgary, Alberta, Canada, November 5-7.

Worthen, A.J., Tran, V., Cornell, K.A., et al., 2016. Steric stabilization of nanoparticles with grafted low molecular weight ligands in highly concentrated brines including divalent ions. Soft Matter 12, 2025–2039.

Xiao, S., Edwards, S.A., & Gräter, F., 2011. A new transferable forcefield for simulating the mechanics of CaCO3 crystals. J. Phys. Chem. C 115, 20067–20075.

Yan, H., Yuan, S., Xu, G., et al., 2010. Effect of Ca^{2+} and Mg^{2+} ions on surfactant solutions investigated by molecular dynamics simulation. Langmuir 26, 10448–10459.

Yan, Y., Li, C., Dong, Z., et al., 2017. Enhanced oil recovery mechanism of CO_2 water-alternating-gas injection in silica nanochannel. Fuel 190, 253–259.

Yang, Y., & Zoback, M.D., 2014. The role of preexisting fractures and faults during multistage hydraulic fracturing in the Bakken Formation. Interpretation 2, SG25–SG39.

Yang, Z., Li, M., Peng, B., et al., 2012. Dispersion property of CO_2 in oil. 2: Volume expansion

of CO_2 + organic liquid at near-critical and supercritical conditions of CO_2. J. Chem. Eng. Data 57, 1305–1311.

Yu, W., Lashgari, H.R., Wu, K., et al., 2015. CO_2 injection for enhanced oil recovery in Bakken tight oil reservoirs. Fuel 159, 354–363.

Zargartalebi, M., Kharrat, R., & Barati, N., 2015. Enhancement of surfactant flooding performance by the use of silica nanoparticles. Fuel 143, 21–27.

Zeppieri, S., Rodríguez, J., & López De Ramos, A.L., 2001. Interfacial tension of alkane + water systems. J. Chem. Eng. Data 46, 1086–1088.

Zhang, J., Pan, Z., Liu, K., et al., 2013. Molecular simulation of CO_2 solubility and its effect on octane swelling. Energy & Fuels 27, 2741–2747.

Zhang, L., Lu, X., Liu, X., et al., 2016. Surface wettability of basal surfaces of clay minerals: Insights from molecular dynamics simulation. Energy & Fuels 30, 149–160.

Zhang, S., Li, Y., & Pu, H., 2020. Studies of the storage and transport of water and oil in organic-rich shale using vacuum imbibition method. Fuel 266, 117096.

Zhang, S., Pu, H., & Zhao, J.X., 2019. Experimental and numerical studies of spontaneous imbibition with different boundary conditions: Case studies of Middle Bakken and Berea cores. Energy & Fuels 33, 5135–5146.

Zhang, Y., Feller, S.E., Brooks, B.R., et al., 1995. Computer simulation of liquid/liquid interfaces. I. Theory and application to octane/water. J. Chem. Phys. 103, 10252−10266.

Zhao, L., Tao, L., & Lin, S., 2015. Molecular dynamics characterizations of the supercritical CO_2-mediated hexane-brine interface. Ind. Eng. Chem. Res. 54, 2489–2496.

Zheng, S., Li, H.A., Sun, H., et al., 2016. Determination of diffusion coefficient for alkane solvent-CO_2 mixtures in heavy oil with consideration of swelling effect. Ind. Eng. Chem.

Res. 55, 1533−1549.

Zhu, A., Zhang, X., Liu, Q., et al., 2009. A fully flexible potential model for carbon dioxide. Chinese J. Chem. Eng. 17, 268–272.